ANL-7249

Argonne National Laboratory

REACTOR DEVELOPMENT PROGRAM

PROGRESS REPORT

August 1966

Printed in USA. Price $4.00 . Available from the Clearinghouse for Federal Scientific and Technical Information, National Bureau of Standards, U. S. Department of Commerce, Springfield, Virginia 22151

ANL-7249
Reactor Technology
(TID-4500)
AEC Research and
Development Report

0571

ARGONNE NATIONAL LABORATORY
9700 South Cass Avenue
Argonne, Illinois 60439

REACTOR DEVELOPMENT PROGRAM PROGRESS REPORT

August 1966

Albert V. Crewe, Laboratory Director
Stephen Lawroski, Associate Laboratory Director

Division	Director
Chemical Engineering	R. C. Vogel
Idaho	M. Novick
Metallurgy	M. V. Nevitt
Reactor Engineering	L. J. Koch
Reactor Physics	R. Avery
Remote Control	R. C. Goertz

Report coordinated by
R. M. Adams and A. Glassner

Issued September 23, 1966

Operated by The University of Chicago
under
Contract W-31-109-eng-38
with the
U. S. Atomic Energy Commission

FOREWORD

The Reactor Development Program Progress Report, issued monthly, is intended to be a means of reporting those items of significant technical progress which have occurred in both the specific reactor projects and the general engineering research and development programs. The report is organized in a way which, it is hoped, gives the clearest, most logical overall view of progress. The budget classification is followed only in broad outline, and no attempt is made to report separately on each sub-activity number. Further, since the intent is to report only items of significant progress, not all activities are reported each month. In order to issue this report as soon as possible after the end of the month editorial work must necessarily be limited. Also, since this is an informal progress report, the results and data presented should be understood to be preliminary and subject to change unless otherwise stated.

The issuance of these reports is not intended to constitute publication in any sense of the word. Final results either will be submitted for publication in regular professional journals or will be published in the form of ANL topical reports.

The last six reports issued in this series are:

February 1966	ANL-7176
March 1966	ANL-7193
April 1966	ANL-7204
May 1966	ANL-7219
June 1966	ANL-7230
July 1966	ANL-7245

REACTOR DEVELOPMENT PROGRAM

Highlights of Project Activities for August 1966

EBR-II

Run No. 20 was completed after 700 MWd of reactor operation. A short, low-power run was made before and after this run to irradiate neutron-flux wires. Run No. 21, giving 610 MWd, was completed on August 27. Integrated reactor power at this time is 9880 MWd. Currently 195 experimental samples are in the reactor in connection with the LMFBR fuels development program.

A scheduled shutdown was initiated for the purpose of required testing, maintenance, and planned modifications.

ZPPR

The construction contractor was notified to proceed with work. Drilling of pilot and pitting holes has begun. Fabrication of fuel elements has begun.

ZPR-3

In Assembly 48, a large plutonium-fueled soft-spectrum core, the reactivity coefficients of a number of materials were measured at the core center by use of an automatic sample changer.

ZPR-6 and -9

Equipment for fabricating Doppler-effect fuel elements of PuO_2 has been procured.

AARR

Critical-facility measurements indicate that the maximum reactivity gain due to voiding of the ITC would occur for a void larger than 70% of ITC volume.

Some of the problems attendant to the design of a neutron "window" may be resolved by using steel instead of aluminum for an 8-in.-thick section of the window.

Stress analysis of the reactor vessel inlet and outlet nozzles indicates that calculated stresses are all below the design limits.

Analysis of digital-computer calculations indicate that the use of constant thermal properties for fuel-plate materials provides adequate accuracy for calculations of transient temperatures.

REACTOR DEVELOPMENT PROGRAM

Highlights of Project Activities for August 1960

EBR-II

Run No. 20 was completed after 700 MWd of reactor operation. A short, low-power run was made before and after this run to irradiate neutron-flux wires. Run No. 21, giving 610 MWd, was completed on August 27. Integrated reactor power at this time is 9880 MWd. Currently 195 experimental samples are in the reactor in connection with the LMFBR fuels development program.

A scheduled shutdown was initiated for the purpose of required testing, maintenance, and planned modifications.

ZPPR

The construction contractor was notified to proceed with work. Drilling of pilot and plating holes has begun. Fabrication of fuel elements has begun.

ZPR-3

In Assembly 48, a large plutonium-fueled soft-spectrum core, the reactivity coefficients of a number of materials were measured at the core center by use of an automatic sample changer.

ZPR-6 and -9

Equipment for fabricating Doppler-effect fuel elements of PuO_2 has been procured.

AAEC

Critical-facility measurements indicate that the maximum reactivity gain due to voiding of the ITC would occur for a void larger than 70% of ITC volume.

Some of the problems attendant to the design of a neutron "window" may be resolved by using steel instead of aluminum for an 8-in.-thick section of the window.

Stress analysis of the reactor vessel inlet and outlet nozzles indicates that calculated stresses are all below the design limits.

Analysis of digital-computer calculations indicate that the use of constant thermal properties for fuel-plate materials provides adequate accuracy for calculations of transient temperatures.

TABLE OF CONTENTS

TABLE OF CONTENTS

TABLE OF CONTENTS

I. LIQUID-METAL FAST BREEDER REACTORS

A. Fuel Development

1. Metal Fuels

a. Irradiation of Uranium-Plutonium Alloys. Twenty full-length (35.6 cm) metal fuel rods are undergoing irradiation in the EBR-II reactor. Details are summarized in Table I.

TABLE I. Status of Metal Fuel Irradiations in Progress

			Design Parameters					Operating Conditions			
										Burnup to Date	
Test Reactor	Capsule or S/A No.	Specimen Number	Fuel Composition (w/o)	Effective Density (%)	Cladding Composition (w/o)	Cladding OD (in.)	Cladding Thickness (in.)	Power Density kW/cc[d]	Max Cladding Temp (°C)	a/o (U + Pu)	fiss/cc x 10^{-20}[a]
CP-5	CP-45	1N15	U-19 Pu-14 Zr	66	V-20 Ti	0.208	0.015	2.6	630	9.8	21.2
EBR-II	XG06	ND23	U-15 Pu-10 Zr	66	V-20 Ti	0.209	0.016	1.7	540	3.8	9.1
EBR-II	XG05	ND24	U-15 Pu-10 Zr	66	V-20 Ti	0.209	0.016	1.7	535	3.6	8.6
EBR-II	XA07	ND28	U-15 Pu-9 Zr	75	304 SS	0.208	0.021	2.0	630	3.7	10.3
EBR-II	XA07	ND41	U-15 Pu-9 Zr	75	304 SS	0.208	0.021	2.0	625	3.6	10.0
EBR-II	XA07	ND32	U-15 Pu-9 Zr	75	316 SS	0.196	0.015	2.0	605	3.5	9.8
EBR-II	XA07	ND43	U-15 Pu-9 Zr	75	Hastelloy-X	0.196	0.015	2.0	615	3.6	10.0
EBR-II	XA07	ND25	U-14 Pu-12 Zr	76	304 SS	0.208	0.021	1.9	600	3.2	8.2
EBR-II	XA07	ND27	U-14 Pu-12 Zr	76	304 SS	0.208	0.021	1.9	605	3.3	8.4
EBR-II	XA07	ND26	U-14 Pu-12 Zr	76	316 SS	0.196	0.015	1.8	590	3.1	7.9
EBR-II	XA07	ND29	U-14 Pu-12 Zr	76	316 SS	0.196	0.015	1.8	595	3.3	8.4
EBR-II	XA07	ND30	U-14 Pu-12 Zr	76	316 SS	0.196	0.015	1.9	615	3.6	9.2
EBR-II	XA07	ND31	U-14 Pu-12 Zr	76	316 SS	0.196	0.015	1.9	610	3.5	8.9
EBR-II	XA07	ND33	U-14 Pu-12 Zr	76	Hastelloy-X	0.196	0.015	1.9	605	3.4	8.7
EBR-II	XA07	ND34	U-14 Pu-12 Zr	76	Hastelloy-X	0.196	0.015	1.9	610	3.5	8.9
EBR-II	XA07	ND35	U-14 Pu-12 Zr	76	Hastelloy-X	0.196	0.015	1.9	615	3.6	9.2
EBR-II	XA07	ND37	U-14 Pu-12 Zr	66	Hastelloy-X-280	0.208	0.015	1.8	610	3.6	9.0
EBR-II	XA07	ND39	U-14 Pu-12 Zr	66	Hastelloy-X-280	0.208	0.015	1.8	610	3.5	8.7
EBR-II	XA07	ND44	U-14 Pu-12 Zr	66	Hastelloy-X-280	0.208	0.015	1.8	600	3.4	8.5
CP-5	CP-44	1N14	U-15 Pu-10 Ti	69	V-20 Ti	0.203	0.015	2.4	560	8.6	19.8
EBR-II	XG05	NC17	U-15 Pu-10 Ti	63	V-20 Ti	0.209	0.016	1.6	540	3.7	8.1
EBR-II	XG06	NC23	U-15 Pu-10 Ti	63	V-20 Ti	0.209	0.016	1.6	540	3.9	8.6
CP-5	CP-41	4N10	U-10 Pu-10 Fz	77	V-20 Ti	0.196	0.016	1.9	550	7.8	22.9
CP-5	CP-41	5N11	U-10 Pu-10 Fz	79	V-20 Ti	0.193	0.016	2.0	550	7.8	23.4
CP-5	CP-41	6N12	U-10 Pu-10 Fz	84	V-20 Ti	0.189	0.016	2.1	550	7.8	24.9
CP-5	CP-41	1N7	U-15 Pu-10 Fz	77	V-20 Ti	0.196	0.016	1.9	550	7.8	22.9
CP-5	CP-41	2N8	U-15 Pu-10 Fz	79	V-20 Ti	0.193	0.016	2.0	550	7.8	23.4
CP-5	CP-41	3N9	U-15 Pu-10 Fz	84	V-20 Ti	0.189	0.016	2.1	550	7.8	24.9
CP-5	CP-43	1N13	U-15 Pu-10 Fz	73	V-20 Ti	0.199	0.015	2.3	540	7.3	20.3
CP-5	CP-50	1N16	Th-20 U	75	V-20 Ti	0.196	0.015	1.9	610	6.7	3.2
CP-5	CP-50	4N19	Th-20 U	75	V-20 Ti	0.196	0.015	1.9	610	6.7	3.2
CP-5	CP-50	2N17	Th-10 Pu-10 U	75	V-20 Ti	0.196	0.015	2.0	630	7.7	3.6
CP-5	CP-50	5N20	Th-10 Pu-10 U	75	V-20 Ti	0.196	0.015	2.0	630	7.7	3.6
CP-5	CP-50	3N18	Th-10 Pu-20 U	75	V-20 Ti	0.196	0.015	1.9	630	4.5	3.3
CP-5	CP-50	6N21	Th-10 Pu-20 U	75	V-20 Ti	0.196	0.015	1.9	610	4.5	3.3

[a]Based on effective density.

Four instrumented, temperature-controlled capsules, which contain several different types of experimental alloy fuels, are being operated in the CP-5 reactor. Table I also summarizes information for these specimens.

U-Pu-Zr alloy is being irradiated in CP-5 in V-20 w/o Ti alloy tubing and has reached a calculated 9.8 a/o burnup at a maximum clad temperature of 630°C.

U-Pu-Ti alloy specimen, also jacketed in V-20 w/o Ti alloy tubing, has attained a calculated 8.6 a/o burnup at maximum clad temperatures of 560°C.

Postirradiation examinations of U-15 w/o Pu-10 w/o Zr fuel alloy jacketed in Type 304 stainless steel, Type 316 stainless steel, and Hastelloy-X tubing are being conducted. These specimens had been irradiated to 1.7 a/o burnup and at maximum jacket temperatures of 600°C. At these temperatures, the specimens showed excellent compatibility between fuel and jacket. The transverse sections of the fuel showed three distinct bands that could be correlated to phase-transformation temperatures (see Fig. 1). The radial temperature gradient was between 580°C at the surface and 680°C at the center of the fuel. The most important reactions are $\gamma + \beta \rightarrow \alpha + \zeta$ at 655°C and $\alpha + \gamma \rightarrow \delta + \zeta$ at 595°C. As anticipated, the fuel had swelled to the internal diameter of the cladding, and the bond sodium was entirely displaced into the gas plenum. Figure 1 also shows that original void volume, which had existed as a sodium-filled annulus around the solid metal fuel pin at the start of irradiation, became redistributed throughout the fuel volume in the form of finely-divided porosity.

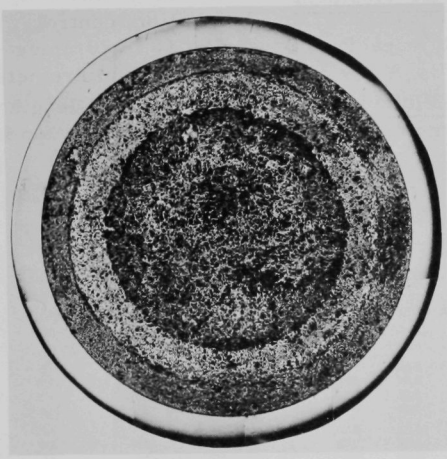

Fig. 1. Transverse Section of U-15 w/o Pu-10 w/o Zr Alloy Jacketed in Hastelloy-X and Irradiated to 1.7 a/o Burnup at a Maximum Cladding Temperature of 600°C. The concentric bands in the fuel were correlated to phase-transformation temperatures. (Magnification 16X)

A U-15 w/o Pu-10 w/o Fz fuel pin jacketed in V-20 w/o Ti tubing was being irradiated in the CP-5 reactor at maximum jacket temperatures of 540°C. This specimen was one that had a selected configuration, and the objective of the test was to determine the maximum attainable burnup before jacket failure. When the fuel had reached a calculated 7.3 a/o burnup, the thermocouples indicated that the jacket had failed. A neutron radiograph of the irradiated capsule confirmed the jacket failure. This fuel rod will be destructively examined in the alpha-gamma metallurgical hot cell facility.

2. Oxide Fuels

a. Particulate Fuel Elements. Thirty fuel specimens of UO_2-PuO_2 in the form of sol-gel spheres and particulate material from the Dynapak process are needed for irradiation in FERMI and in EBR-II. A partial shipment of sol-gel spheres has been received from ORNL. The particulate material has been received and reduced to proper size fractions.

In the past, feed preparation for vibratory compaction processes was carried out by laboriously and inefficiently crushing materials by hand. Commercially available, laboratory-type jaw crushers are large and cumbersome from the standpoint of glovebox operation. In addition, control over jaw spacing is crude, and hourly capacities upward of 10 to 20 times our normal criticality limit is typical. A jaw crusher built with micrometer stroke and jaw adjustments (see Fig. 2) was used to crush the material described above.

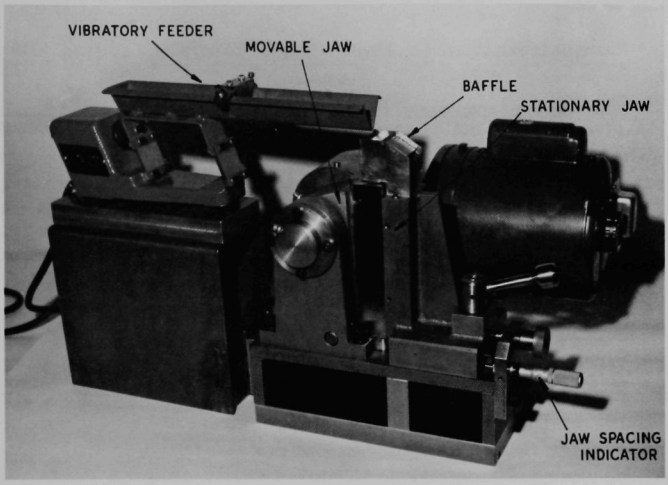

Fig. 2. Jaw Crusher and Feeder

b. Oxide and Cermet Fuel Irradiations in EBR-II. The status of mixed oxide and stainless steel-PuO_2 cermet specimens under irradiation in EBR-II is shown in Tables II and III. The cermets were manufactured by Battelle Northwest Laboratories and prepared for irradiation by Argonne National Laboratory.

TABLE II. Status of UO_2-20 w/o PuO_2 Irradiations in Progress in EBR-II

		Design Parameters				Operating Conditions			
								Burnup to Date	
Capsule or S/A No.	Specimen Number	Effective Density (%)	Cladding Composition	Cladding OD (in.)	Cladding Thickness (in.)	Power Density kW/cc[a]	Max Cladding Temp (°C)	a/o (U + Pu)	fiss/cc x 10^{-20}[a]
X009	SOV-5	82	304 SS	0.297	0.020	1.7	555	2.3	4.8
X009	SOV-6	82	304 SS	0.297	0.020	1.7	565	2.5	5.1
X011	SOV-3	83	304 SS	0.296	0.019	1.9	610	1.8	3.8
X011	HOV-4	80	Hastelloy-X	0.295	0.014	1.8	600	1.8	3.6
X011	TVOV-1	77	V-20 w/o Ti	0.297	0.020	1.7	575	1.8	3.4
X011	SOV-7	85	304 SS	0.296	0.019	2.0	630	1.8	3.7
X011	SOV-1	80	304 SS	0.296	0.019	1.7	590	1.8	3.5
X011	HOV-10	86	Hastelloy-X	0.295	0.014	1.9	615	1.7	3.7
X011	HOV-15	80	Hastelloy-X	0.295	0.014	1.7	590	1.7	3.4

[a]Based on effective density.

TABLE III. Status of Cermet Fuel Irradiations, Clad in Type 304 Stainless Steel, in Progress in EBR-II

Capsule or S/A No.	Specimen Number	Design Parameters: Fuel Composition (w/o)	Design Parameters: Effective Density (%)	Design Parameters: Cladding OD (in.)	Design Parameters: Cladding Thickness (in.)	Operating Conditions: Power Density kW/cc[a]	Operating Conditions: Max Cladding Temp (°C)	Operating Conditions: Burnup to Date: a/o (U + Pu)	Operating Conditions: Burnup to Date: fiss/cc x 10^{-20}[a]
X011	5P-9	SS-40 PuO_2	98	0.301	0.015	0.88	495	2.5	1.9
X011	5P-12	SS-27 PuO_2	99	0.294	0.015	0.59	450	2.5	1.2
X011	5U-14	SS-27 UO_2	98	0.298	0.013	0.45	435	1.9	0.98

[a]Based on effective density.

3. Carbide Fuels

a. Compatibility of (U,Pu)C with Potential Cladding Materials

(i) Compatibility with Stoichiometric and Hyperstoichiometric (U,Pu)C. Testing of potential iron-, nickel-, and vanadium-based cladding materials (see Progress Report for April 1966, ANL-7204, pp. 16-17) with single-phase monocarbide and with two-phase hyperstoichiometric carbides continues. The single-phase monocarbide being used contains 4.83 w/o equivalent carbon, while the hyperstoichiometric carbide contains 5.25 w/o equivalent carbon, resulting in a proportionate amount of $(U,Pu)_2C_3$ as a second phase.

Haynes 56 alloy, which showed no reaction with either carbide composition at 800°C for 42 days (approximately 1000 hr), is being tested under more severe conditions. Compatibility couples containing this material and heat-treated at 900°C for 42 days have been examined metallographically. Again, no reaction was observed between this material and either carbide composition. Other compatibility couples containing this material are being heat-treated at 800°C for 167 days.

Alloy 16-25-6, which showed a distinct mottled effect and a disappearance of grain boundaries to a depth of 25 to 35 μ when tested with the carbide compositions at 800°C for 42 days, has been tested at 700°C for the same length of time. A somewhat similar, but less distinct, effect has been observed at this temperature. After etching, grain boundaries that were distinct in the interior portion of the cladding could no longer be seen within about 50 μ of the interface. The very fine mottled structure, thought to be molybdenum carbide precipitates, still found in the 800°C specimens, have not been observed in the 700°C specimens.

Two previously untested alloys, Inconel 625 and V-15 w/o Cr-5 w/o Ti, are currently being tested.

Since many of the 700 to 900°C tests have shown only relatively slight differences between the effects of the (U,Pu)C and hyperstoichiometric (U,Pu) carbides, more severe tests are planned to indicate more clearly the role played by the sesquicarbide phase. Accordingly, pellets of $(U_{0.8}Pu_{0.2})_2C_3$ are being prepared.

(ii) Uranium Sulfide Additions to Hyperstoichiometric (U,Pu) Carbides. Based on the work of Shalek and White[1] on the UC-US system, there are indications that sulfide additions to uranium carbides can result in better compatibility between the carbides and potential cladding materials. For this reason, a preliminary study of the effects of sulfide additions on hyperstoichiometric (U,Pu)C has begun.

An arc-melted button of $(U_{0.8}Pu_{0.2})$ carbide containing 5.3 w/o equivalent carbon was crushed to less than 44 μ and divided into three parts; similarly sized US powder was blended with the carbide powder in two of the parts in amounts constituting 15 and 30 w/o of the batches. After pressing, the pellets were fired at 1900°C for 2 hr, then refired at 2000°C for 2 hr, but high-density pellets were not obtained from the mixed powders. Geometric densities are given in Table IV.

TABLE IV. Fired Densities of (U,Pu)C + US Mixtures

Hyperstoichiometric (U,Pu)C (w/o)	US (w/o)	Firing Temp (°C)	Geometric Density (g/cm^3)	Estimated % Theoretical Density*
100	-	1900	11.61	87
-	100	1900	9.79	90
85	15	1900	10.07	77
		2000	10.41	80
70	30	1900	9.53	75
		2000	9.79	77

*Based on densities of $(U_{0.8}Pu_{0.2})C$, $(U_{0.8}Pu_{0.2})_2C_3$, and US, and assuming no interaction.

Further attempts will be made to promote sintering in the carbide-sulfide mixtures in order to achieve greater densification.

(iii) Irradiations in EBR-II. The status of mixed carbide specimens under irradiation in EBR-II is shown in Table V. A hazards analysis

TABLE V. Status of UC-20 w/o PuC Irradiations in Progress in EBR-II

		Design Parameters				Operating Conditions			
								Burnup to Date	
Capsule or S/A No.	Specimen Number	Effective Density (%)	Cladding Composition	Cladding OD (in.)	Cladding Thickness (in.)	Power Density kW/cc[a]	Max Cladding Temp (°C)	a/o (U + Pu)	fiss/cc x 10^{-20}[a]
XG05	SMV-2	84	304 SS	0.297	0.020	2.1	645	3.8	10.4
XG05	HMV-5	80	Hastelloy-X	0.297	0.015	2.2	670	3.9	10.2
XG05	NMV-11	84	Nb-1 w/o Zr	0.281	0.012	2.1	645	3.9	10.8
XO08	NMP-2	82	Nb-1 w/o Zr	0.281	0.012	1.6	545	2.2	5.8
XO08	NMV-4	80	Nb-1 w/o Zr	0.281	0.012	2.4	635	3.1	8.2
XO08	NMV-7	80	Nb-1 w/o Zr	0.281	0.012	2.1	605	2.8	7.5
XO08	NMV-12	86	Nb-1 w/o Zr	0.281	0.012	2.4	635	3.1	8.7
XO08	HMV-1	80	Hastelloy-X	0.297	0.015	2.1	640	2.8	7.3
XO08	HMV-4	80	Hastelloy-X	0.297	0.015	2.3	670	3.0	8.1
XO08	HWMP-1	82	Hastelloy-X + W	0.297	0.020	1.6	555	2.1	5.6
XO08	HWMV-1	83	Hastelloy-X + W	0.297	0.020	2.4	685	3.1	8.5
XO09	SMV-1	82	316 SS	0.306	0.024	1.6	570	2.3	6.3
XO09	SMP-1	80	316 SS	0.306	0.024	2.1	640	1.8	4.7
XO09	VMV-1	86	Vanadium	0.301	0.022	2.5	640	2.7	7.6

[a]Based on effective density.

[1]Shalek, P. D., and White, G. D., "Studies in the System Uranium Carbide-Uranium Sulfide," Carbides in Nuclear Energy, Vol. I, Macmillan and Co., Ltd., London (1964).

of four rods containing physically mixed UC and PuC powders, vibratory-compacted solid solution (U,Pu)C powder, and UC-20 w/o PuC pellets was completed for consideration by the EBR-II Irradiations Review Committee.

4. Fuel Cladding and Structure

a. Development of Refractory-metal Alloy for Service in Oxygen-contaminated Sodium. Exposure of V-20 w/o Ti (TV-20) samples for 32 hr to flowing[2] sodium (2.45 cm/sec) containing 2 to 5 ppm oxygen by weight in the temperature range from 550 to 750°C has been completed. Under these conditions the alloy gains weight according to a parabolic rate law, primarily a result of solution of oxygen in the metal, resulting in a hardened layer at the surface. The rate constant determined from two or more runs at a given temperature varied from 2.5×10^{-4} $(mg/cm^2)^2$ hr^{-1} at 550°C to 25×10^{-4} $(mg/cm^2)^2$ hr^{-1} at 750°C.

A short series of experiments was performed in order to make certain that the excellent corrosion behavior of TV-20 in sodium at 650°C in a cold-trapped loop was not due to total depletion of oxygen available to the system. About 1 g of Na_2O_2 was added to the sodium, and the system was operated without refractory alloys for three days with the cold trap at 120°C (as indicated by a thermocouple on the outside wall). An initial one-week exposure of fresh TV-20 coupons (flow of 6.1 m/sec, and 9 ppm terminal oxygen by weight) gave unexpectedly large corrosion. Even so, significantly lower results than previously reported for a dynamic test in sodium with 15 ppm oxygen by weight were obtained. It was believed that perhaps the time allotted for transfer of the oxygen into the cold trap (three days) was too short, since 1 g Na_2O_2 would result in an initial concentration of 300 to 400 ppm oxygen. A second one-week exposure with fresh samples produced the expected low weight gains of the same order as those obtained in the first week of the interrupted long-time test; terminal oxygen concentration was 10 ppm (by mercury amalgamation analysis). This provides evidence that good corrosion behavior of TV-20 can be achieved in a cold-trapped sodium system.

Having reassured ourselves of the acceptability of TV-20 in a cold-trapped sodium system, the interrupted 116-day test at 650°C, and 6.1 m/sec velocity (see Progress Report for July 1966, ANL-7245, p. 11) has been restarted with the addition of V-5 w/o Cr samples. The V-Cr binary appears to be superior to V-Ti with respect to oxygen pickup from sodium containing less than 10 ppm oxygen.

An experiment was performed to see if the relative corrosion resistance of alloys remained the same above and below the sharp break in corrosion behavior at a level of about 10 ppm oxygen. Sheet samples

[2]Velocity imparted by rotation of sample cages.

were exposed first to oxygen-refreshed sodium at 650°C (cold trap at 120°C) for one week. The same samples were ground free of corrosion product and re-exposed to oxygen-refreshed sodium (cold trap at 170°C) for a second week. The results of the two tests are compared in Table VI. It is apparent that the relative amounts of corrosion shift as the oxygen content of the sodium is changed. Microexamination of the alloys prior to exposure showed evidence of segregation and cracking in the first four alloys listed in Table VI. Corrosion penetration along the cracks was noted.

TABLE VI. Corrosion of Vanadium Alloys in 650°C Sodium
(Seven-day exposure)

Alloy (Composition in w/o)	Weight Change (mg/cm^2)	
	Cold Trap at 120°C (8.2, 7.5 ppm O by weight)	Cold Trap at 170°C (15 ppm O by weight)
V-15 Ti-10 Cr Annealed	+0.19	-9.6
V-15 Ti-10 Cr 40% Cold Work	+0.26	-10.0
V-15 Ti-12.5 Cr Annealed	+0.16	-8.7
V-15 Ti-12.5 Cr 40% Cold Work	+0.16	-8.6
V-40 Ti-10 Cr 50% Cold Work	+0.25	-5.2
V-20 Ti Annealed	+0.48	-7.3

Other refractory metals are also of interest to this program. Initial tests are in progress in an oxygen-refreshed system (cold trap at 120°C) at 650°C. Oxygen content, by mercury amalgamation, varies from 7 to 10 ppm. Samples of Cr, Mo, Ti, Nb, V, and Ta are being exposed simultaneously. To date (28 days of exposure), the molybdenum sample is unchanged, and the chromium specimen is still metallic in appearance, with a weight loss of only 0.08 mg/cm^2. Titanium and vanadium samples first gained and are now losing weight as some of the oxide is lost. Total changes are small, -0.08 mg/cm^2 for the vanadium tab and -0.5 mg/cm^2 for the titanium specimen. Tantalum and niobium samples lost weight from the start, and at 28 days the tantalum coupon shows a loss of 7.5 mg/cm^2 and the niobium tab 0.63 mg/cm^2.

5. Fuel Reprocessing

Pyrochemical processes are being developed for processing fast reactor fuels of the ceramic type (e.g., oxide or carbide). A process which utilizes liquid metal-molten salt extractions and salt-transport separations[3] is currently being investigated for the separation of fissile and fertile constituents of the fuel from the fission products. The conceptual process flowsheet has been described previously (see Progress Report for May 1966, ANL-7219, pp. 21-22).

a. Laboratory Investigations of the Oxide-reduction Step and the Salt-transport Separations Step

(i) Salt-transport Separation Step. For this step, magnesium-copper alloy is being considered for use as the donor solvent, and $MgCl_2$ is under consideration for use as the salt carrier between the donor alloy and the acceptor alloy, e.g., zinc-magnesium. An experiment was conducted to investigate the separation of zirconium from uranium and plutonium. The distribution coefficient of zirconium between molten $MgCl_2$ and zirconium-saturated copper-magnesium alloy was measured at 800°C. Zirconium distributed strongly in favor of the copper-magnesium alloy. Since the zirconium concentrations in the $MgCl_2$ were near the limit of detection, the observed zirconium distribution coefficient (ratio of w/o zirconium in salt to w/o zirconium in metal) of about 5×10^{-4} represents an upper limit to the actual value. This small value of the distribution coefficient indicates that zirconium is unlikely to transport with uranium or plutonium.

The experiment was designed also to yield data on the solubility of zirconium in liquid copper-magnesium alloys. At 800°C the solubility of zirconium varied from 3.9 w/o in a copper-magnesium alloy containing 37.5 w/o magnesium to 2.7 w/o in an alloy containing 49.1 w/o magnesium. These values indicate that it will be possible to separate zirconium from uranium by taking advantage of solubility differences; for example, the solubility of uranium in a copper-magnesium alloy containing 49 w/o magnesium is about 0.07 w/o at 800°C.

A cadmium-zinc alloy is being considered as an alternative donor alloy for the copper-magnesium alloy indicated in the conceptual flowsheet. In recent work, a portion of the uranium-cadmium-zinc system was investigated to obtain information about the solubility of uranium[4] in the

[3] In the salt-transport separations, the fissile and fertile materials are selectively transferred from one liquid metal solution (donor) to another (acceptor) by cycling a molten salt phase which acts as a carrier between the two metal solutions. Noble and refractory-metal fission products remain in the donor alloy.

[4] In discussing the solubility of uranium in the ternary system, it is necessary to refer to two liquidus fields in the region of low zinc concentration. In one field, which is below the transition temperature, the solid in equilibrium with the liquid is "UCd_{11}." In the other field, which is above the transition temperature, alpha-uranium is the solid phase.

ternary system at low zinc concentrations. The results of this investigation were as follows. The transition temperature for the peritectic decomposition of UCd_{11} increased from 472 ± 2°C to 485 ± 2°C as the zinc concentration was increased from 0.0 to 2.0 w/o zinc. The increase in the peritectic transition temperature may be attributed to an increase in the free energy of the compound brought about by the substitution of zinc for cadmium in UCd_{11} to produce $UCd_{11-x}Zn_x$. When the liquid phase was supercooled to initiate the transition of alpha-uranium to UCd_{11}, the degree of supercooling decreased with increasing zinc concentration of the mixture. It is conjectured that the change in degree of supercooling results from the introduction of zinc into the solid phase, and that the smaller zinc atom enhances nucleation and brings about an onset of crystallization of the solid phase at a higher temperature than that for pure UCd_{11}.

The solubility of alpha-uranium varied at 500°C from 2.4 w/o uranium at 0.0 w/o zinc to 3.0 w/o uranium at 2.1 w/o zinc. Below the transition temperature, for example at 470°C, the solubility of uranium in equilibrium with UCd_{11} or $UCd_{11-x}Zn_x$ decreases on adding zinc, and varies from 2.4 w/o uranium at 0.0 w/o zinc to 2.0 w/o uranium at 2.1 w/o zinc. The retrograde solubility of alpha-uranium, found in the U-Cd system[5] continues in the ternary system up to at least 2 w/o zinc.

b. Engineering Investigations of Salt-transport Separations. A series of experiments is being made to determine systematically the rates of transfer of various solutes (U, Pu, Mg, Zn, and fission products) in the salt-transport separation step. The purpose of these tests is to provide information which will make it possible to calculate mass-transfer rates for various batch and continuous versions of the salt-transport separation step. In an immiscible liquid metal-molten salt system, the mass transfer rate of a solute is a function of the geometry, mixing conditions, solute mass-transfer coefficient, and difference in solute activities in the bulk salt and metal phases.

The variables to be studied in this experimental program include temperature, mixing conditions, vessel volume, metal composition, and salt composition. The initial work is concerned mainly with the study of the uranium and plutonium mass transfer rates.

(i) Uranium Extractions. An experiment involving the extraction of uranium from a liquid Cu-5.5 w/o Mg donor alloy to a molten $MgCl_2$ salt phase was completed. All of the uranium (5.5 w/o) was in solution. The extraction was carried out at 840°C and a stirring speed of 490 rpm in a baffled $4\frac{1}{4}$-in.-ID tungsten vessel. The uranium mass-transfer rate was

---

[5]Martin, A. E., Johnson, I., and Feder, H. M., Trans. Met. Soc., AIME 221, 789 (1961).

very rapid; greater than 99% of the equilibrium concentration was reached in less than 10 min. The rapid extraction was attributed to the absence of precipitated uranium.[6]

(ii) Plutonium and Cerium Extraction. An experiment involving the simultaneous transfer of plutonium and cerium from a liquid Cu-33 w/o Mg donor alloy to a molten $MgCl_2$-30 m/o NaCl-20 m/o KCl salt phase was also completed. The extraction was conducted at 600°C and at a stirring speed of 650 rpm in a baffled $2\frac{1}{2}$-in.-ID tantalum vessel. Preliminary results indicate that the approach to equilibrium was nearly complete in about 10 min and that the plutonium was extracted more rapidly than the cerium.

c. Plutonium Salt-transport Separations. Following the successful completion of uranium salt-transport separation experiments which demonstrated the engineering feasibility of this method (see Progress Report for July 1966, ANL-7245, p. 14), plans are in progress to conduct similar experiments with plutonium. Equipment and materials are being procured.

B. EBR-II

1. Reactor Improvements

a. Oscillator System Mark II. The oscillator rod drive test rig was disassembled and inspected after the first series of test runs wherein preliminary high-speed test runs had indicated an increase in torque readings (see Progress Report for July 1966, ANL-7245, pp. 23-25, and Table VII below). Inspection revealed that the two lower drive-shaft bearings fabricated from Colmonoy No. 4 were scored; the two upper bearings and the oscillator rod bearing were in good condition.

TABLE VII. Oscillator Rod Operation

Oscillator Speed (rpm)	Time Operated (hr)		
	1st Series	2nd Series	Total
0-60	12	-	12
120-240	15	5	20
300	7	8	15
360	-	5	5
480	-	5	5
			57

[6]In a similar experiment in which uranium precipitate was present in the donor alloy and which was conducted at 800°C and at a stirring speed of 810 rpm, the rate of uranium extraction was significantly lower; to achieve greater than 99% of the equilibrium concentration required about 40 min.

A careful examination of the support structure revealed a total clearance of 0.045 in. between the bearing carrier and the test tank support socket. This excessive clearance was reduced to 0.009 in. by making minor changes in the test structure.

The two scored bearings (of Colmonoy No. 4) were polished to their original specifications and the matching bearing sleeves (of Stellite 6B) were refabricated to maintain the original radial clearances of 0.0025 in.

The hydraulic, thermal, and stress investigations for the oscillator system Mark II have been completed and were found to be very satisfactory.

Sodium flow through the rod is established at a minimum controllable rate. Each of the two internal, parallel, orificing paths have 0.144-in.-dia holes which provide a sodium flow of 5.7 gpm. When two B_4C-filled capsules are present, an increase in sodium temperature of approximately 45°F should occur at an elevation equivalent to the top of the core. Tests indicate that 19.3 gpm of sodium passes through the bearing below the core and flows upward in the annulus between the oscillator rod and its guide tube. Due to heat transfer from adjacent subassemblies, this bypassing sodium will increase in temperature by about 50°F at an elevation equivalent to the top of the core and will increase in temperature to 135°F at the top exit. This has a most desirable moderating effect on thermal gradients and associated thermal stresses within the systems.

At room temperature, the containment-tube expansion-chamber assembly is pressure tested with 20 atm of helium at room temperature. At operating temperature, the strength of the material will permit only 15 atm pressure. Based on perfect-gas equations, and the assumption that all the gas produced from the $B(n,\alpha)$ reaction is released, approximately 3.4 atm of pressure will be developed in the containment-tube expansion-chamber assembly for each percent of burnup in the boron carbide tubes. With one atmosphere pressure (absolute) in the expansion chamber at the time of closure, no problems due to gas-expansion pressure can be visualized for the intended duration of the oscillator rod life.

For the second run, the first two oscillator rods were loaded with boron carbide as presented in Table VIII. Loads 1 and 2 are adjacent on one side of the rod, and loads 3 and 4 are adjacent on the other side. Loads 1-3 and 2-4 are diametrically opposite.

The first oscillator rod (OSC-1) is presently being dynamically balanced in its final assembled and stress-relieved condition. The second rod (OSC-2) is being welded in its final assembly stage.

TABLE VIII. Oscillator Rod Loadings

Rod No.	Capsule Tube	Tube Loading Material	Tube Loading Weight (g)	Tube Loading Length (in.)
OSC-1	1	Al_2O_3	77.9	14.00
	2	Al_2O_3	78.0	14.01
	3	B_4C	78.0	13.97
	4	B_4C	77.9	13.98
OSC-2	1	B_4C	76.2	14.00
	2	SS	*	*
	3	Al_2O_3	75.6	13.99
	4	SS	*	*

*Solid stainless steel rods. Based on the chemical and isotopic analyses, the boron carbide contains 69 percent boron-10.

b. Sodium-surveillance Periscope. Modification of the periscope to eliminate problems experienced with the optical system was continued, and fabrication of the redesigned parts was completed (see Progress Report for May 1966, ANL-7219, p. 3). Assembly of the new parts is approximately 25% complete. Present efforts are directed toward obtaining a satisfactory seal of the synthetic sapphire windows to the stainless steel frames. Several methods being investigated include a Kovar-glass-sapphire lamination technique and a commercial process which provides a direct sapphire-to-stainless steel type of seal. The periscope assembly is expected to be completed in September. At that time, the leak tests and operating checkout will be performed.

2. Operations

Run No. 20 was completed on August 6 after attaining its scheduled 700 MWd of operation.

Following this, six subassemblies containing flux wires for power-distribution measurements were loaded into four core and two outer blanket locations, and Run No. 20-B (1 hr at 50 kW) was made. This measurement was planned in conjunction with a similar run (No. 20-A) prior to Run No. 20 (see Progress Report for July 1966, ANL-7245, pp. 21-22). Preliminary analysis of the measurements of fission-rate distribution from Run No. 20-A is given below (Section I.B.4).

The flux-wire subassemblies were removed, and core loading changes were made in preparation for the following power run. In addition to experimental subassembly XO12, 19 subassemblies were loaded into the

reactor core as follows: ten enriched-core type, six control rods, two enriched inner blanket, and one safety rod. Run No. 21, scheduled for 610 MWd, was started on August 12, and completed on August 27, at which time the integrated reactor power was 9880 MWd.

The main generator has been repaired by replacing the rotating field connection box covers (after radiography) and installing a new forward generator bearing (see Monthly Progress Report for July 1966, ANL-7245, pp. 22-23). Realignment of the turbine and generator was also completed and the machine was returned to service for Run No. 21. Operation has been satisfactory.

After Run No. 21, a shutdown period was started to accomplish numerous maintenance and modification tasks. An access hole was drilled through the small rotating plug into the outer side of the seal trough to enable better observation of the condition of the seal and to permit sampling of the seal metal (Bi-Sn alloy) to determine whether it is contributing to difficulties being experienced in rotating the plugs. If so, corrective action will be taken.

3. Experimental Irradiations

Experimental subassembly XO12 containing nineteen oxide-fuel capsules from NUMEC was assembled, inspected, flow tested, and charged into EBR-II position 4B2. XO12 is scheduled for about 20,600 MWd of reactor operation at 45 MWt (this residence time will achieve approximately 100,000 MWd/mt).

Two alpha-measurement subassemblies, U-1548X and U-1549X, were discharged following Run No. 20. These subassemblies were the 5th and 6th to be discharged from a group of eight subassemblies originally charged as part of the alpha-measurement program.

The flow-calibration program for the recently available Mark-B subassemblies was continued. Of the four Mark-B models, the 61- and 37-pin designs have now been completed, the 19- and 7-pin designs are still to be calibrated. Calibration tests have shown dual orificing will be required to eliminate cavitation for cases demanding relatively low flow rates through these subassemblies.

At the end of Run No. 21, the reactor contained 195 samples of fuel, cladding, and other reactor materials which are being irradiated for the LMFBR fuels development program. Their status is as follows:

Subassembly	Date Loaded	Capsule Content and Number of Capsules ( )	Experimenter	Accumulated Exposure (MWd)	Goal Exposure (MWd)
XG02	7/16/65	UO_2-20 w/o PuO_2 (1) Stainless Dummies (18)	GE	7379	13,600
XG03	7/16/65	UO_2-20 w/o PuO_2 (2) Stainless Dummies (17)	GE	7379	19,450
XG04	7/16/65	UO_2-20 w/o PuO_2 (2) Stainless Dummies (17)	GE	7379	39,000
XG05	9/3/65	UO_2-20 w/o PuO_2 (9) U-15 w/o Pu-10 w/o Zr (1) U-15 w/o Pu-10 w/o Ti (1) UC-20 w/o PuC (3) Structural (5)	GE ANL ANL ANL GE	6952	10,300
XG06	9/3/65	UO_2-20 w/o PuO_2 (12) U-15 w/o Pu-10 w/o Zr (1) U-15 w/o Pu-10 w/o Ti (1) Structural (5)	GE ANL ANL GE	6952	20,600
XA07	10/27/65	U-14 w/o Pu-11 w/o Zr (16) Structural (3)	ANL ANL	6215	18,600
XA08	12/13/65	UC-20 w/o PuC (8) Structural (11)	ANL ANL	5130	19,800
XO09	3/24/66	UC-20 w/o PuC (3) UO_2-20 w/o PuO_2 (2) 304 SS-30 v/o PuO_2 (1) 304 SS-20 v/o PuO_2 (1) UC-20 w/o PuC (3) Structural (4) Structural (3) Structural (2)	ANL ANL PNWL PNWL UNC PNWL ANL GE	4310	5,130
XO10	3/24/66	UO_2-20 w/o PuO_2 (4) Structural (11) Structural (4)	GE ANL PNWL	4310	19,600
XO11	5/9/66	UO_2-20 w/o PuO_2 (7) UO_2-20 w/o PuO_2 (9) 304 SS-30 v/o PuO_2 (1) 304 SS-20 v/o PuO_2 (1) 304 SS-20 v/o UO_2 (1)	ANL GE PNWL PNWL PNWL	2739	8,300
XO12	8/10/66	UO_2-20 w/o PuO_2 (19)	NUMEC	610	20,600
XO13	7/17/66	Structural (18) Graphite (1)	ANL PNWL	1309*	1,200
XO14	7/17/66	Structural (17) Graphite (1) Graphite (1)	PNWL NRL GE	1309	**
U-1550X	5/6/65	Alpha Monitor	ANL	8250	9,120***
U-1551X	5/6/65	Alpha Monitor	ANL	8250	9,120

*Exposure completed.
**Maximum attainable before core has reached terminal size.
***Minimum acceptable.

4. Reactor Physics

Six Mark-I-fuel control rods have now been replaced with Mark I-A fuel. One of these, control rod No. 12, was installed and calibrated in June (see Progress Report for June 1966, ANL-7230, p. 3). These rods have been calibrated by period measurement and by intercomparison. The average reactivity worth of the Mark-I-A control rods is 1.07 times greater than the Mark-I rods, which is in agreement with corresponding values measured for the substitution of standard fuel subassemblies with Mark I-A.

Values obtained for calibrations made this month are as follows:

Control Rod	Fuel Type	Reactivity Worth (Ih)	Control Rod	Fuel Type	Reactivity Worth (Ih)
1	Mark I-A	139	7	Mark I	138
3	Mark I-A	138	10	Mark I-A	162
5	Mark I-A	145	11	Mark I-A	138

By means of the subcritical counting technique, the worths of a pair of Mark-I-A safety rods were determined to be 1.2% $\Delta k/k$. Data from rod-drop tests made at the beginning of Run No. 21 are being processed.

Preliminary results have been obtained pertinent to possible radiation damage of the beryllium used in the neutron source. Measurement by the MTR staff showed the formation of ~0.5 cc of He^4 per cc of beryllium had been formed in the beryllium which had been exposed to 5600 MWd of reactor operation. Since earlier MTR tests showed that swelling of beryllium at 600°C does not begin with less than 20 cc of He^4/cc of Be it would appear that our Sb-Be sources are capable of much longer residence periods.

The data from measurements of fission-rate distribution for Run No. 20-A have been partially analyzed. The results indicate that along the radius chosen for the measurements (free of experiments), the fission-rate distribution agrees more with the homogenized 80-subassembly cores calculated for Runs No. 20-A and 20-B. Figure 3 shows the reactor loading for these runs and the location of the experimental flux wires. However, the data from Run 20-B, which measured fission rates at radial positions in the core adjacent to experimental subassemblies, appear to agree more closely to the calculated homogenized 80-subassembly core. Data are compared in Fig. 4.

Some results from rod-drop tests in EBR-II are shown in Table IX. The objects of the tests were to separate various feedback components and to evaluate their amplitudes and time dependencies. Three separate feedback processes were considered: (a) prompt feedback, concerned mainly

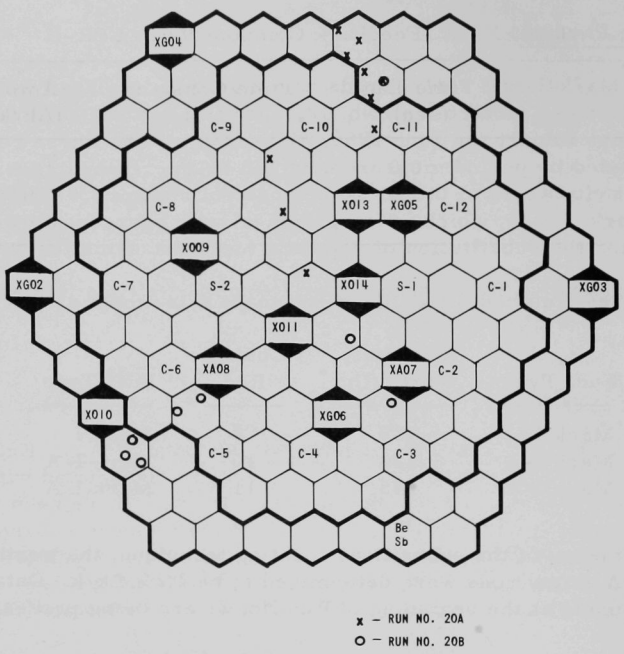

Fig. 3. Location of Wire Detectors in 80-subassembly Core of EBR-II

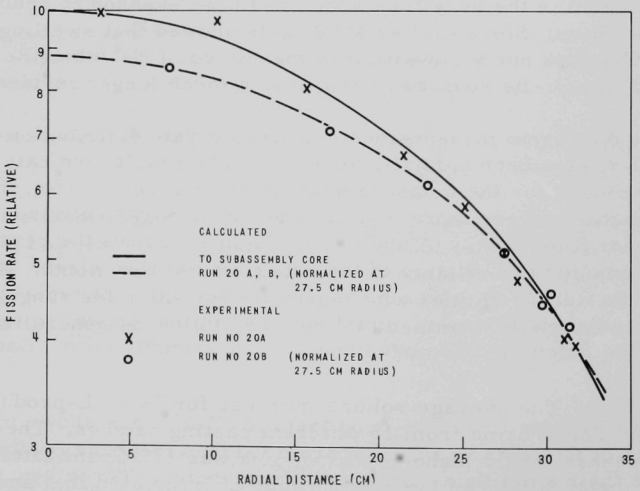

Fig. 4. Radial Fission Rates in EBR-II

TABLE IX. Feedback Components in EBR-II

	Time Lag (sec)	Time Constant (sec)	Amplitude ($\Delta k/k$-MW)
Prompt	~0.0	0.33	2.55×10^{-5}
Intermediate	3.0	7.0	0.67×10^{-5}
Delayed	100.0	33.0	0.53×10^{-5}

with fuel expansion; (b) feedback of an intermediate time interval, associated with the delayed expansion of control rod shafts; and (c) strongly delayed feedback, originating presumably from structural expansion.

5. Fuel Cycle Facility

a. EBR-II Vertical Assembler-Dismantler (VAD). Engineering studies of the viewing and manipulation problems associated with the use of the VAD in the Air Cell of the Fuel Cycle Facility have been completed. These show that it will be necessary to position the core subassemblies vertically in the VAD and to install extended-reach manipulators in the Air Cell. With these provisions, satisfactory loading, welding, cutting, and element removal can be performed on all subassemblies now planned or being used in the reactor. However, the difficulty of handling elements during installation and removal increases with the length of the element. If, in the future, full-length elements are used in large numbers, it may be necessary to design additional, specialized fixtures for this purpose.

Detail design work for the major components of the VAD have been completed. Detail drawings of all units which are likely to involve long fabrication times have also been completed and are now being released for fabrication. All long-delivery purchased items have been ordered. Detailing on other units is continuing and these will be released for fabrication as they are completed.

b. Surveillance of Mark-I-A Fuel. Three additional subassemblies with maximum burnups of 1.20, 1.16, and 1.16 a/o (C-184, C-197, and C-198) were subjected to surveillance examination in the past month. A total of six Mark-I-A subassemblies with maximum burnup in the range from 1.16 to 1.22 a/o have been examined to date. The following generalizations have been noted:

(i) The average volume increase for 72 ANL-produced pins was 13.0%. These came from 15 different casting batches. The average volume increase for 75 Idaho-produced pins was 11.3%; the latter were all cast from ingots produced by melt refining of irradiated fuel and came from 12 different casting batches.

(ii) Two of the subassemblies contained pins from two ingots produced by consolidation of scrap from casting and pin processing, and from rejected pins. The charge for one run (MRC 30) consisted mostly of rejected pins and scrap, and exhibited a volume increase of 9.1%. The charge for the other (MRC 29) consisted of heels from injection casting. The average volume increase for pins of this source was 11.9%.

(iii) One batch of pins cast from a melt-refining ingot (MR 24) had a much lower than average volume increase (7.7%) than had resulted from the rest of the pins produced from MR ingots, normally containing little reject material. Examination of the charge for this run showed that it contained only 1/3 of the charge as irradiated fuel and the other 2/3 of the charge was recycle reject and makeup material. These pins were not included in the value calculated (11.3%) for MR runs listed (i) above.

(iv) Visual examinations of subassemblies and of the clad pins showed no abnormalities resulting from reactor operations or postirradiation handling operations. Straightness values of the entire subassemblies were comparable with those observed prior to irradiation. The individual element cladding appeared to be sound and undamaged. No measurable increase in the cladding diameter was observed.

(v) Limited data showed that significant diameter increases have occurred on the fuel pins themselves. Measurements of the ends of the pins showed a 0.003-0.006-in. increase in diameter and up to a 0.0120-in. increase for the center section of the pins. The latter would be a maximum value obtainable, since any larger increase would cause deformation of the cladding and this was not observed. The increase in volume of the pins as a result of these diameter changes would be about 9%, which is in agreement with the values obtained from sodium-height measurements.

Measurements of axial growth of the pins showed that increases of approximately 0.1-0.2 in. have occurred.

c. Effect of Thoria Removal on Bonding Efficiency. Previously reported data (see Progress Report for May 1966, ANL-7219, pp. 5-6) showed that fewer bond testing rejects for void formation occurred with ANL-produced pins than Idaho-produced pins. One hypothesis for the reason is in the difference in production methods. ANL pins were wiped clean of the injection-casting mold wash prior to canning, whereas the Idaho pins were canned as produced. In order to investigate this further, approximately 2000 Idaho-produced pins were tested; 1500 were forced through a brass wire brush to remove the thoria mold wash prior to canning and the remaining 500 were canned without brushing. The reject rate for voids was about 50% higher for the nonbrushed pins. Investigation of this procedure will continue.

d. Production Summary for August 1966

Subassemblies received:		16 plus 4 flux-wire assemblies
Subassemblies dismantled:		13
Subassemblies fabricated:		15
Subassemblies transferred to reactor:		18
Pins decanned:		1236
Melt refining:	8 irradiated	4 recycle
Pour yield (av):	92.7	92.3
Injection-casting runs:		16
Pin processing:		
Accepts:		1503
Rejects:		149
Pins welded:		1817
Leak testing:		
Accepts:		1591
Rejects:		35
Bond testing (completed runs):		
Accepts:		910
Rejects:		126
Surveillance:		C-186, C-184, C-197, C-198

C. Physics Development

1. ZPR-3

Experiments continued with Assembly 48, a large, plutonium-fueled critical experiment with a soft neutron spectrum similar to the several-thousand-liter cores being considered for future power reactors (see Progress Report for June 1966, ANL-7230, pp. 5-6). Included in the month's program have been measurements of material reactivity coefficients at the core center, Doppler coefficient measurements, and additional fission-ratio experiments.

a. Measurements of Reactivity Coefficients. The reactivity coefficients of several materials were measured at the core center of Assembly 48 utilizing an automatic sample changer. The mechanism allowed the exchange of 2 x 2 x 2-in. samples within a like sample space at the front of the central core drawer of half No. 1 when that drawer was remotely removed from the reactor. Reactivity differences were obtained between the different samples and with a void space situated at the core center. A ZPR-3 control rod in conjunction with an autorod was used for this measurement, which also re-established the same subcritical power level each time the central drawer was reinserted.

Materials which were inserted in the sample space in the form of 2-in. cubes included Fe, Cr, Ni, Mn, steel, Na, Al, Al_2O_3, graphite, depleted uranium, and Mo. Smaller plates or foils of materials were also inserted into the sample space by positioning them with light, steel springs within 2-in. cubical boxes of thin-walled steel. Included in the small samples were various thicknesses of 2-in.-square enriched uranium and tantalum foils, 1/8 x 2 x 2-in. plates of depleted uranium, molybdenum, boron, plutonium, iron, and nickel, and small cylinders of molybdenum and tantalum. Part of the experiments were investigations of effects of sample size, but the accuracy of the measurements generally did not afford much distinction. Every effort was made to obtain the best precision possible with the equipment utilized; however, temperature drift in the assembly still produced appreciable reactivity effects and was the predominant source of error. The data from the experiments are still undergoing analysis.

b. Doppler Measurements. Reactivity effects due to heating were measured for natural uranium, plutonium-239, and an empty sample. The natural uranium sample was run twice to measure the repeatability of the experimental technique. Preliminary analyses indicate that: (1) the average uncertainty in individual measurements was ~7 to 10 x 10^{-8} in k; (2) the empty can has no reactivity effect; and (3) the two experiments with natural uranium agreed to within ~3.5% (about two sigma).

c. Fast Reactor Experiments and Analyses. As part of a continuing program to permit closer correlation of experimental data obtained in different laboratories, U^{238}/U^{235}, U^{233}/U^{235}, and Pu^{239}/U^{235} fission ratios were measured at the center of the U^{235}-fueled Los Alamos spherical critical assembly FLATTOP. Special gas-flow fission chambers were designed for this purpose. These contained carefully calibrated fission foils which have been manufactured and calibrated by techniques identical to those now in use for construction of ZPR-3 and other Idaho Division fission chambers. Preliminary data indicate good agreement with the fission ratios measured by the Critical Assemblies Group at Los Alamos. This program will be continued and extended when more different types of fission foils have been manufactured.

An intercomparison of one U^{235} Idaho Division foil with Los Alamos U^{235} foils was made by M. Thorpe of Los Alamos by irradiation in the thermal column of the Los Alamos Water Boiler Reactor. This comparison gave agreement with the assumed deposited masses to within 2% accuracy. A comparison of the same Los Alamos U^{235} foils was previously made with a U^{235} foil manufactured by White of AWRE, Aldermaston, England, with good agreement with the deposited masses. Thus the Idaho U^{235} foils are, indirectly, in good agreement with the AWRE foils of White which were used for the most recent accurate measurements of microscopic U^{235} fission cross sections.

A careful intercomparison of fission ratios was made in the core of Assembly 48 using new back-to-back, gas-flow fission chambers and the Kirn-type chambers which have been used in most ZPR-3 assemblies. This work included direct measurement of the effects of scattering in the Kirn chamber walls upon fission in U^{238}, U^{236}, U^{234}, and Pu^{240} foils using thick, steel-walled chambers and very thin aluminum-walled chambers. The back-to-back counter foils have been very carefully intercalibrated and are in good agreement with AEE, Winfrith, England, and Los Alamos foils where comparisons can be made. After appreciable wall-scattering corrections (up to 8%) have been applied, the Kirn chamber ratios are in good agreement with those obtained using the back-to-back chambers, and these latter chambers will be used for all future measurements of ZPR-3 fission ratio.

d. Measurements of Fast Neutron Spectrum. A comparison was made of the results of Assembly 48 spectrum measurements made by the proton-recoil and semiconductor sandwich techniques. The comparison was made by calculating the pulse-height distribution expected if the semiconductor sandwich were placed in a neutron-energy spectrum identical to that indicated by the proton-recoil results. The two measurements agree within the limits of the counting statistics.

Considerable effort was spent on a machine calculation of the "geometrical efficiency" of the Li^6-semiconductor sandwich neutron spectrometer. By "geometrical efficiency" is meant the probability of detecting

in coincidence both products of a $Li^6(n,\alpha)H^3$ reaction which takes place between the diodes. The center-of-mass motion of the reaction products makes this an energy-sensitive parameter. The machine program is written for the case of separated diodes having the Li^6 layer in the middle.

2. ZPR-6

Measurements of sodium-void coefficients were made in Assembly 5, a nominal 2600-liter, cylindrically shaped uranium carbide core containing approximately 1600 kg of U^{235}. The core height is 56 in., 28 in. in each half, and is reflected on each end with 30 cm of depleted uranium. The normal material arrangement within the three basic drawer loadings is shown in Fig. 5. Note that the sodium columns are contiguous to columns

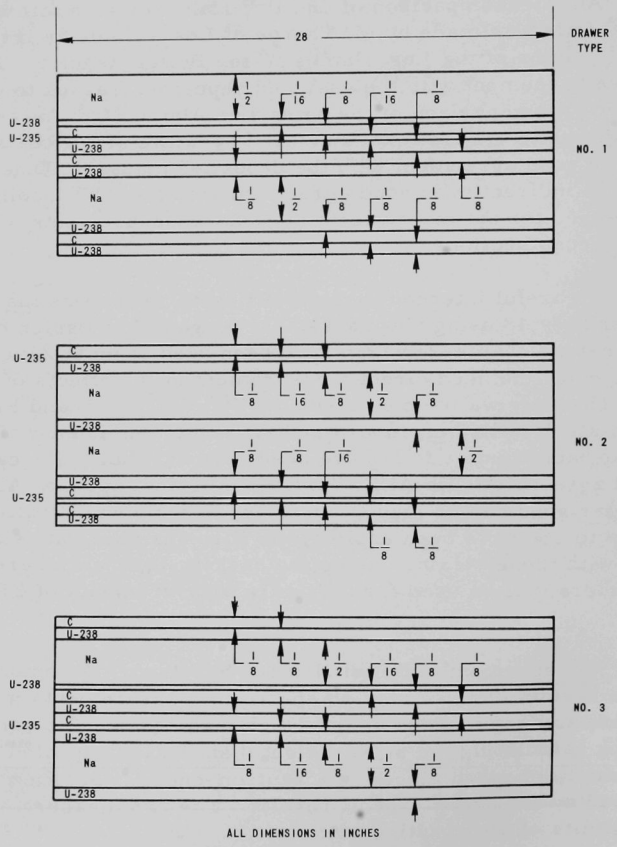

Fig. 5. Arrangement of Materials in Each of the Three Types of Drawers Used in Assembly 5 of ZPR-6

of depleted uranium. Vertical columns of each type of drawer are arranged sequentially to comprise the reactor core, i.e., Nos. 1, 2, 3, 1, etc. The core is reflected radially with ~22 to 28 cm of depleted uranium. Each core drawer has two 1/2-in.-wide, 28-in.-long columns of sodium contained in Type 304 stainless steel cans. Voiding is accomplished by replacing sodium-filled cans with identical empty cans.

Measurements were made by one or both of two methods: (1) observing the critical positions of calibrated control rods with and without sodium in the core, and (2) observing the asymptotic period with and without sodium in the core. In the second case, the rods were arranged to be either fully in the core or out of the core. Thus rod positions were fixed by mechanical stops. No significant difference in results was obtained using either of the methods.

Periods were measured using d.c. ionization chambers and d.c. current amplifiers. The current-amplifier output was fed into a voltage-to-frequency converter to obtain pulse rates proportional to ion chamber currents. These pulses were directed to the input scalers of a digital computer which was programmed to perform a least-squares fit of the data to an exponential function and to compute the period. Residuals, least-squares sums, and standard deviations were printed to provide a precision index.

It is necessary during these measurements to shut the reactor down and separate the table halves to remove the sodium from the drawers. The major experimental uncertainties probably result from table-closure uncertainties and environmental changes. The latter were reduced by either preceding or following a voided-configuration measurement with a reference run.

The spatial dependence of the sodium-void coefficient was determined for both the axial and radial directions. The central void coefficient was determined for both a 3 x 3-drawer and a 1 x 3-drawer high void extending axially for 2 in. on each side of the core midplane. In subsequent measurements of the axial void coefficient, the 2-in. void region in the central 3 x 3-drawer array was moved axially to the positions A, B . . . H, as shown in Fig. 6. In this way voided sections, F for example, correspond

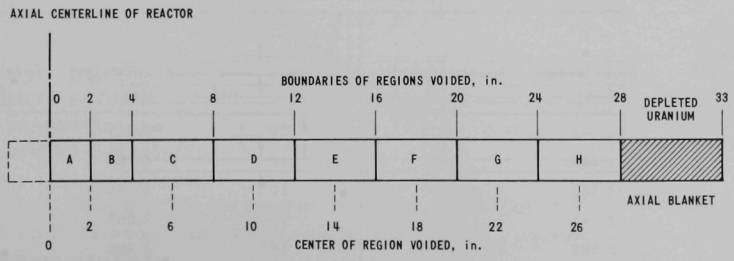

Fig. 6. Schematic Drawing Showing Axial Positions Which Can Be Voided by Substitution of Sodium-filled Cans by Unfilled Cans

to sodium removal from the central 3 x 3-drawer array and extend from 16 to 20 in. from the core midplane in both the movable and stationary halves. Results of these measurements are shown in Fig. 7.

Measurements of the radial dependence of the coefficient were made by moving the 1 x 3-drawer high void from the center to positions 4, 7, 10, and 14 drawers off the center. In these measurements, the sections A + B ± C (see Fig. 6) were voided on both sides of the reactor center to produce regions approximately 16 in. long, 2 in. wide, and 6 in. high. The results are plotted in Fig. 8 and tabulated in Table X.

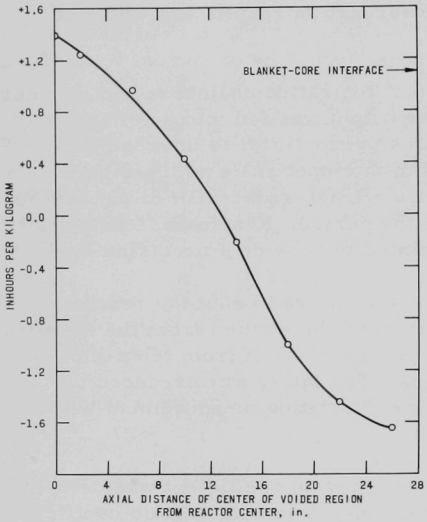

Fig. 7. The Change in Reactivity per kg of Sodium Removed from the Core for Various Axial Distances from the Center of ZPR-6 Assembly 5

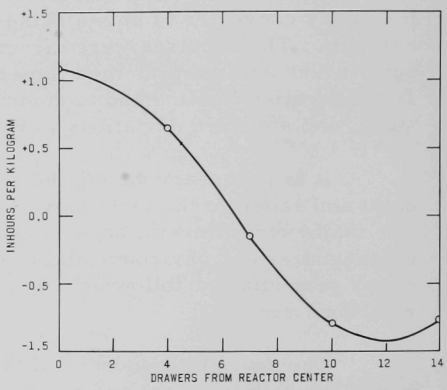

Fig. 8. The Change in Reactivity per kg of Sodium Removed from the Core for Various Radial Distances from the Center of ZPR-6 Assembly 5

TABLE X. Sodium-void Coefficients for Assembly 5 of ZPR-6

(Radial Traverse)

Section Voided (Number of drawers from reactor center)	Sodium Weight (kg)	Specific Worth (Ih/kg)	Section Voided (Number of drawers from reactor center)	Sodium Weight (kg)	Specific Worth (Ih/kg)
0	1.242	+1.10	10	2.585	-0.79
0	1.242	+1.08	10	2.585	-0.83
4	2.585	+0.65	10	2.585	-0.77
4	2.585	+0.64	14	2.585	-0.75
7	2.585	-0.15	14	2.585	-0.77

3. ZPR-9

Doppler coefficient measurements have been made in Assembly 11 with 1/2- and 1-in. expandable natural uranium samples and with a 1/2-in. expandable enriched uranium sample. Preliminary results indicate these measurements are reasonably consistent with similar measurements made in Assembly 9 (see Progress Report for December 1965, ANL-7132, pp. 15-17).

4. ZPPR

a. Construction and Procurement. The construction contractor for the Zero Power Plutonium Reactor facility, Arrington Construction Co., Idaho Falls, Idaho, was notified to proceed with work on August 8. Drilling pilot holes and large pitting holes has commenced.

A meeting of representatives of Division of Reactor Development and Technology, AEC-Chicago, AEC-Idaho, and ANL was held to discuss the present status of the project: construction schedules, equipment procurement, project organization, reporting procedures, quality control, inspection procedures, and ZPPR operations and planning. The conclusions of this meeting are as follows:

(1) The major uncertainty in the construction is the procurement of long-lead-time items, primarily electrical equipment.

(2) No delay is expected due to ANL procurements since all long-lead-time items have been ordered.

(3) The fuel-loading machine is not needed for initial operation of ZPPR.

(4) A Commission decision concerning continued operation of ZPR-3 is needed in the near future to provide adequate time to compose a facility staff and to train operators if it is decided to continue operation.

Procurement of reactor components is continuing. The present status of the reactor components is as follows:

(i) Bed and Tables. As of August 15, the ball screw and nut had been completed, assembled, and tested. Machining of the transmission is 85% complete and that on the bed is 75% complete. The machining on the tables is 85% complete.

(ii) Matrix Drawers. A lot of 1200 fuel drawers has been welded on both ends and stretched to size. ANL representatives will inspect the finished drawers.

(iii) Matrix Tubes. The vendor has been instructed to ship the finished tubes, stored at the vendor's plant since April, to ANL-Idaho.

(iv) Nuclear Instrumentation. Channels 1 and 2 (log count rate and period) are 60% complete. Channels 3 and 4 (log N period) are completed and 90% checked out. Channels 5 and 6 (linear safety) are completed and 75% checked out. Channels 7 and 8 (linear current) are completed and checked out. The relay chassis are completed and checked out.

(v) Area Gamma Monitors. The area gamma monitors are completed and checked out.

(vi) Poison Safety Rod Drives. The purchase order for the poison safety rod drives was sent to McGee and Hogan of Salt Lake City on August 23. Delivery of the first rod drive is scheduled in 60 days. The remaining rod drives are scheduled for 120 days after acceptance of the first rod drive by ANL.

(vii) Reactor Knees. The purchase order for the reactor knees was sent to Macauley Foundry Company of Berkeley, Calif. The scheduled delivery is December 1966.

(viii) Personnel Shields. Bids were again solicited for the personnel shields since the previous short bidding period resulted in no bids being received.

(ix) Tube Bundling. This item has been deleted and is being replaced by matrix-alignment equipment. This includes a rigid plate to hold the individual tubes in place as they are clamped by the knees and matrix tie-down beams, as well as instruments and holding rods. The detailed design of this equipment has started.

(x) Source Drives. The purchase order for the source drives was sent to Teleflex, Inc., North Wales, Pa. The delivery time is 26 weeks.

(xi) Rod-drive Mounting Plates. The purchase order for rod-drive mounting plates was sent to Greenlee Foundries, Inc., Chicago, Ill.

(xii) Matrix Tie-down. The purchase order for the matrix tie-down was sent to the Rupert Iron Works, Rupert, Idaho. Delivery is scheduled for January 1967.

(xiii) Beta-Gamma Air Particulate Monitors. The purchase order for three beta-gamma air particulate monitors was sent to Nuclear Measurements Corp., Indianapolis, Ind.

(xiv) Loading Platform. The purchase order for the ramp assembly, which holds the platform in place when inserted between the halves, was sent to the Rupert Iron Works, Rupert, Idaho.

All other bids on reactor components are either in a state of review or being prepared for resubmission of bids.

b. Fuel Development

(i) Fabrication of Reactivity-coefficient Fuel Elements. Several hundred plate-type plutonium fuel elements (see Fig. 9) are required to determine the effects of increasing percentages of Pu^{240}, Pu^{241}, and Pu^{242} on reactor kinetics. The elements consist of Pu-1.1 w/o Al alloy plate cores sealed in tight-fitting stainless steel jackets. It is planned to manufacture such elements in isotopic ranges from 95 w/o Pu^{239} to 96 w/o ($Pu^{240} + Pu^{241} + Pu^{242}$) as such materials become available. This program will also provide valuable information on the gamma- and neutron-radiation levels experienced during the fabrication of plutonium from highly irradiated fuel, an important subject to the long-range power reactor program.

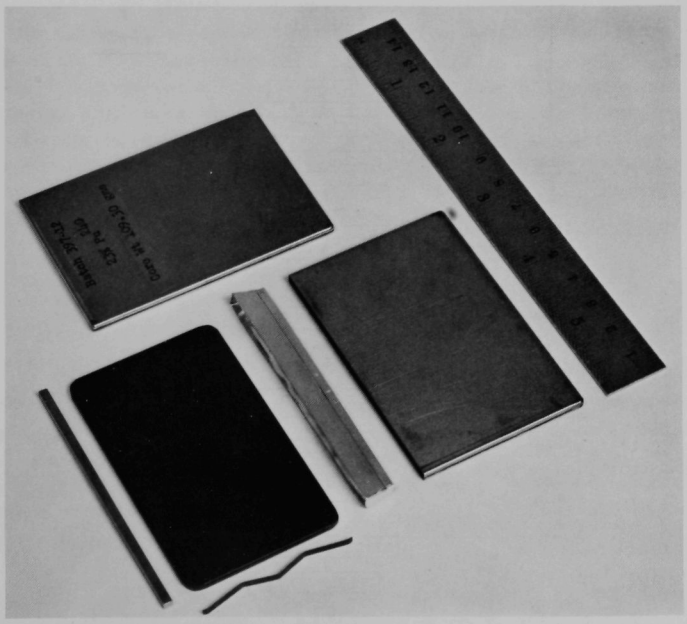

Fig. 9. Danger-coefficient Elements and Components, Including End Plug, 22% Pu^{240} Plate, Spring, Loading Funnel, and Jacket

The flow diagram of the process developed for fabricating these elements is shown in Fig. 10. The purified, highly irradiated plutonium is received in the form of reduction buttons that weigh about 2 kg each. The alloy is made in a vacuum induction furnace. Electrical-grade aluminum wire is placed on the bottom of an yttria-coated magnesia crucible and broken plutonium button is placed on top of the wire. The alloy is melted and heated to 950°C. It is bottom poured into an yttria-coated carbon billet mold. After the casting cools, the furnace is opened, the billet is removed and carefully cleaned. The top is sawed off to produce a rolling billet that measures approximately 16 x 50 x 125 mm.

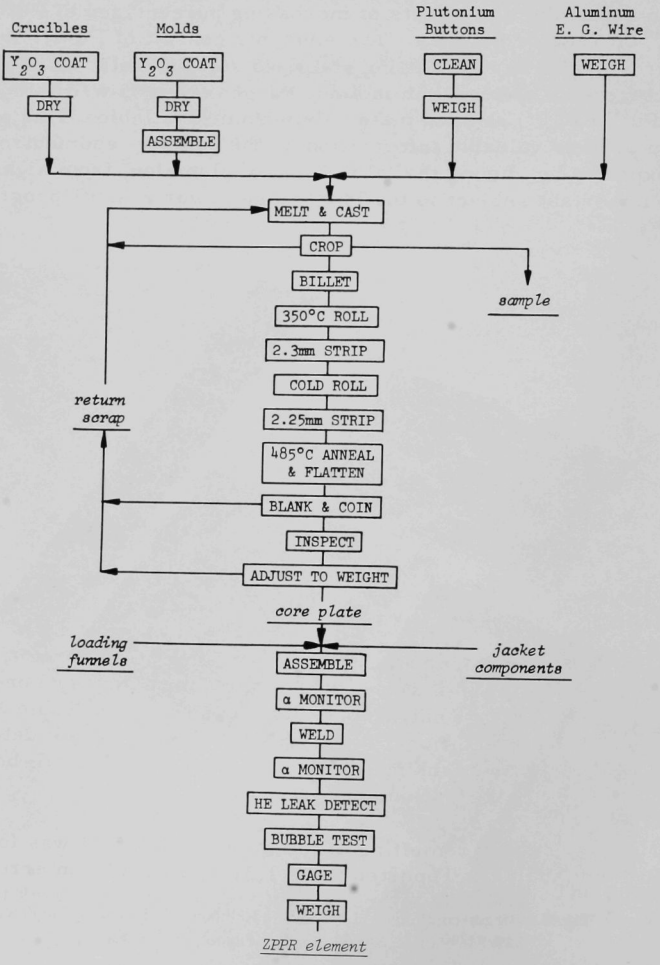

Fig. 10. Flow Diagram for Manufacture of ZPPR Reactivity-coefficient Elements

The billet is heated to 350°C and hot rolled from 16- to 2.30-mm thickness. Reductions are 15% per rolling pass between 125-mm dia x 200-mm, two-high rolls that are electrically heated to 235°C. The 2.30-mm-thick strip is cold finish rolled to 2.25-mm thickness. It is then annealed by heating to 485°C and flattened while hot by pressing between steel flats.

Three sizes of core plates are required, 2.25 mm thick by 45.0 mm wide with lengths of 23.0, 49.3, or 74.7 mm. These are blanked and coined from the strip by combination dies in a 200-tonne press. Coining pressures of 4 tonnes/cm^2 are used. The core plates are cleaned and adjusted to within ±0.5 g of nominal weight by punching holes in the plates. Drilling for weight adjustment was not successful because the material work hardened rapidly.

The core plates are inspected and are inserted into jackets made of 0.3-mm-thick Type 304 stainless steel. A spring is installed in each jacket to hold the core plate against one end of the jacket. An aluminum-foil funnel is used during loading of the core to protect the jacket lip from being contaminated by plutonium. The assembly is done in a contamination-clean glovebox by contamination-preventive methods. After loading, the funnel is removed and the end plug is inserted; welding is done by means of the tungsten-electrode d.c.-arc process in copper chills that completely enclosed the elements except at the edges being joined. The closure welds are made in a welding chamber at one-third to one-half standard atmosphere pressure of 85 v/o helium, 15 v/o argon gas. The completed reactivity-coefficient elements are monitored for alpha contamination, leak detected, gauged, weighed, inspected, and packed for shipment to the reactor experimental groups.

The first shipment of plutonium for this program had the following average isotopic composition: 72.73 w/o Pu^{239}, 22.09 w/o Pu^{240}, 4.51 w/o Pu^{241}, and 0.69 w/o Pu^{242}. There were 12 buttons weighing 23.43 kg.

Twelve Pu-1.1 w/o Al alloy billets were cast, the as-cast weight of each billet being approximately 1800 g. The sprue ends were removed and two samples were taken, one from the top and one from the bottom of each billet. Analytical results are shown in Table XI. It is anticipated that two additional melts will be made to consolidate and recover scrap from the blanking operation. This material will be fabricated into special flux-perturbation specimens.

After remelting of the melt No. R295, it was found that the aluminum analysis, reported to be 1.31 w/o Al, was in error. The billet was remelted a third time to bring the aluminum content back to analyses.

TABLE XI. Calculated and Analyzed Aluminum Content of Billets

Melt Number	Calculated Composition	Aluminum Analysis (w/o)	
		Top	Bottom
R293	Pu-1.10 w/o Al	1.16	1.14
R295	Pu-1.10 w/o Al	1.31	1.32
R297	Pu-1.10 w/o Al	1.19	1.21
R299	Pu-1.15 w/o Al	1.08	1.11
R300	Pu-1.10 w/o Al	1.13	1.08
R302	Pu-1.10 w/o Al	1.15	1.08
R325 (R295 adjusted)	Pu-1.09 w/o Al	0.95	0.97
R326	Pu-1.10 w/o Al	1.08	1.19
R327	Pu-1.11 w/o Al	1.10	1.13
R328	Pu-1.10 w/o Al	1.13	1.12
R329	Pu-1.11 w/o Al	1.08	1.12
R331	Pu-1.11 w/o Al	1.10	1.08
R332	Pu-1.11 w/o Al	1.12	1.15
R343 (R325 adjusted)	Pu-1.11 w/o Al	1.10	1.09

Four billets have been carried through the complete fabrication process, the experience gained from this can be summed up as follows: the Pu-1.1 w/o Al alloy rolls very easily at 350°C, but the alloy work hardens very rapidly when rolled at room temperature. A cold finishing reduction of 0.05 mm was about the maximum practical reduction. Cold straightening by ironing or stretching was not successful, but the stock was easily straightened by heating to approximately 485°C and ironing between steel flats. Oxidation was not a problem in the helium atmosphere that contained approximately 1000 ppm O_2 and 50 ppm H_2O by weight.

Core plates were produced from the rolled strip by means of a combination blanking and coining die. A load of 75 tonnes was sufficient for blanking and coining the 45 x 75-mm core plates. Higher loads tended to make the alloy stick in the die. There was no appreciable straightening in the coining operation, since the coining operation produced very little metal flow.

The procurement of high-quality stainless steel jackets was a continuing problem. The first lot of jackets was rejected because of improper finishing of the weld seams. A partial shipment of the second lot of jackets was found to be satisfactory. Jacketing and welding operations have been started and appear not to present difficulty other than the usual problem of control of alpha contamination.

Integrated radiation-dose records are being maintained on all personnel during this fabrication, and the exposure from each operation is also recorded. These records will be compared with the radiation doses predicted by a computer program. The objective of this study is to develop equations and experience for radiation exposure during the fabrication of plutonium from highly irradiated fuels. Experience to date has shown that it is possible to handle 2-kg batches of 22 w/o Pu^{240} material without exceeding 100 mr per week for the periods of time shown in Table XII.

TABLE XII. Time Limits for Handling 22 w/o Pu^{240} and 4.6 w/o Pu^{241}

Hours per Week	Handling Condition
1.0	Glove contact with 0.75-mm neoprene gloves
2.5	Glove contact with 0.75-mm light-leaded gloves (0.10-mm lead equivalent)
10.0	Body exposure at 400 mm through 3/8-in. unshielded window

(ii) Development of Zero-power Plutonium Reactor Fuels. The development of design and specifications for ZPPR fuel elements was completed, and the following specifications were issued:

ANL Specification Number	Title of Specification
PF-1600	Specification for Uranium, Plutonium, Molybdenum Alloy ZPPR Fuel Elements
PF-1607	Specification for Plutonium for ZPPR Fuel Elements
PF-1612	Specification for Uranium for ZPPR Fuel Element Fabrication

The suitability of the above specifications to the practical fabrication of the fuel elements was tested by developing methods for fabricating the elements and by testing these methods through pilot-lot manufacture of fuel elements. A procedure was written that was followed closely for the manufacture of 73 fuel elements in sizes ranging from 1- to 8-in. nominal length. As this procedure is slightly different from the process described previously (see Progress Report for January 1966, ANL-7152, pp. 24-32), it is summarized below.

The flow diagram is shown in Fig. 11. The major steps of core-plate manufacture are (1) preparation of uranium-molybdenum binary alloy, (2) melting of the binary alloy with plutonium and casting into

precision-sectioned bars, (3) parting core slugs from the bars, (4) milling the cores to precise lengths, (5) weight adjustment of the cores by milling to a variable width, and (6) cleaning the cores to prevent contamination in the jacketing operation. Accurate materials accountability was practiced for all operations on the cores. Precise charge calculations and accurate weighing of all materials were required.

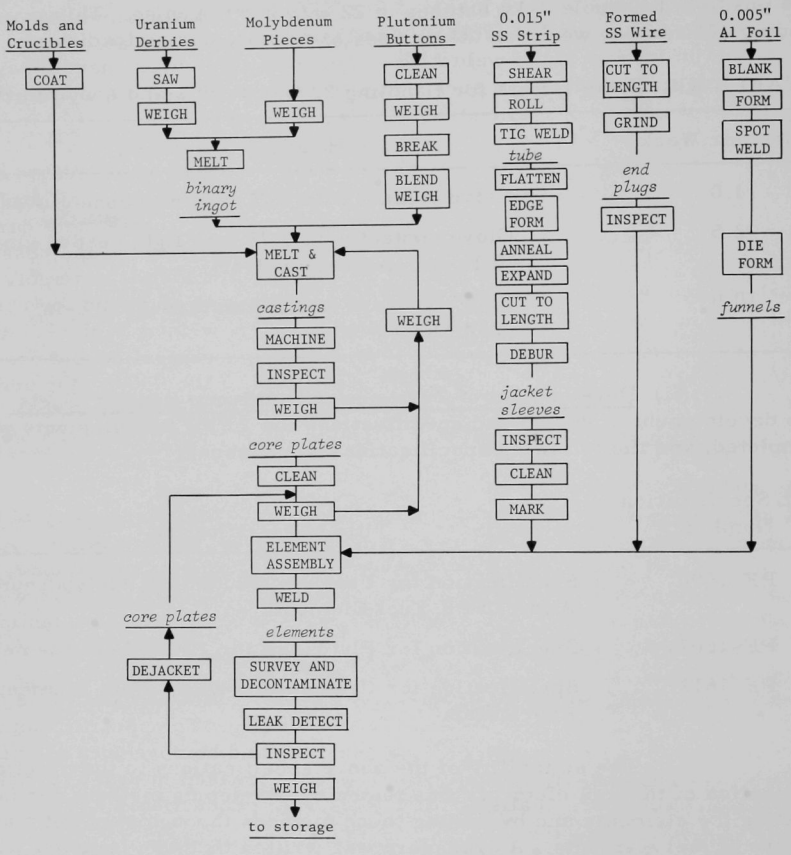

Fig. 11. Flow Diagram for Manufacture of ZPPR Fuel Elements

The steps of fabrication of the jacket sleeve are (1) roll forming and welding stainless steel strip into welded tube, (2) die flattening the tube, (3) die forming the longitudinal edges of the tubes, (4) stretch forming the tube in a precision box die by means of an expanding mandrel, and (6) cutting the jacket sleeves to lengths from the formed tubes. End plugs were cut from formed Type 304L stainless steel wire and were finished to precision tolerance by grinding and milling. All jacket components were thoroughly cleaned.

Contamination-preventive methods were practiced in assembling and welding the fuel elements. After thoroughly brushing and wiping the core plates to remove loose metal or oxide dust, they were transferred to a contamination-free assembly glovebox. Clean jackets were moved into the area, and the bottom plug was installed and welded into place. The jacket sleeves were installed in the welding chills and aluminum-foil funnels were inserted into the jacket opening. This prevented contact between the jacket lip and core plate during loading and reduced contamination of the weld area. The core plates were handled by special tongs and fixtures in such a way that the jackets and contamination-free areas were not contaminated with plutonium.

Welding was done in a chamber that can be evacuated and back-filled with argon-helium gas mixture to one-third to one-half atmospheres pressure. Copper chills contacted all sides of the element during welding to prevent the expansion of the gas within the element and possible weld contamination or blowout. A spring plunger in the chill assembly column loaded the bottom end plug, core plate, top end plug, and top chill with about 88 kg of force while the top end plug was welded in place. All movement of the welding machine was mechanically controlled and programmed. The weld was made by fusing the edge of the jacket plug and the end sleeves by means of a d.c.-arc drawn from the tungsten electrode. The chills and welding parameters were adjusted so that radiused beads were made without buildup.

Inspection operations were carried out at each step of the process for quality-control purposes. Micrometers, surface gauges, and comparators were used for pilot-lot inspection in order to obtain data, but go, no-go gauges will be allowed in production. The plates were weighed on precision balances. The jackets were leak-detected by bubble testing and by mass spectrometer.

A number of provisions of the specification was found to be impractical to meet as they were originally written. The specification was rewritten with liberalization of the composition and homogeneity provisions and some of the dimensional tolerances were increased in order to make the specification more realistic for commercial production.

(iii) Properties of Zero-power U-Pu-base Alloys. Two SEFOR fuel plates, manufactured by NUMEC and reported upon in the July 1965, April 1966, and June 1966 Monthly Progress Reports (pp. 23-24 of ANL-7082, p. 23 of ANL-7204, and pp. 22-23 of ANL-7230, respectively), have been corrosion tested in air for 16 months. The control fuel plate, T13-10, without a jacket defect, has retained its original dimensions. Fuel plate T13-12, which has a small and a large notch filed in the jacket to simulate jacket defects, remained stable for eight months, began swelling during

the ninth month, and has now swelled to 0.876 cm in thickness from its original 0.584 cm. It has also swollen laterally and longitudinally. Maximum contamination measured at the larger notch was 10M, but during handling of the fuel plate a significant amount of powder fell from this notch and gave readings greater than 200M. The corrosion test in air has been discontinued, and the fuel plate will be dejacketed for examination.

D. Other Fast Reactor Physics

1. Nuclear Constants

Neutron radiative capture cross sections are being measured as a function of neutron energy between a few keV and about 3 MeV by the activation technique, in which the sample is exposed to a monoenergetic neutron beam, and analyzed for its radioactive capture product by beta or gamma counting.

The capture cross section of Np^{237} has recently been measured for 8 neutron energies between 150 keV and 1.5 MeV. No data have been available for this reaction until the present work, although the reaction is important to fast reactor technology because it is a source of Pu^{238}. The amount of Pu^{238} may have an important influence on fuel-reprocessing methods.

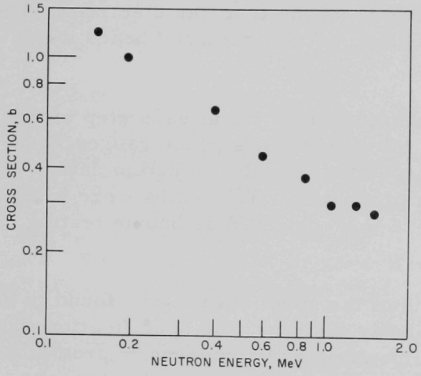

Fig. 12. Capture Cross Section of Neptunium-237

The data are shown in Fig. 12. The absolute values of the cross sections are subject to a possible correction which may result in values about 10% greater than the present values. Several more points will be taken to extend the measurements to about 3 MeV. For the future, efforts are being made to get a ~100-g metallic neptunium sample which will allow measurements to be made down to about 5 keV.

E. Component Development

1. Sodium Technology

a. Physicochemical Mechanics of Metals. As a part of a program to determine the effects of 1200°F sodium on Type 304 stainless steel, a simple test was run in which samples were exposed to this environment and then compared to identical samples exposed only to 1200°F air (see Progress Report for January 1966, ANL-7152, pp. 48-49). The samples

used were of the same heat and were in the form of tubing of 0.494-in. OD and 0.018-in. wall thickness. The electrical resistivity of the samples was first determined in the "as received" condition. The samples were then exposed to each environment and specimens removed for examination at intervals of 3, 5, and 7 days. The examination of these samples consisted of a redetermination of their electrical resistivity followed by a 15-min Strauss test, followed in turn by a third determination of their electrical resistivity. Table XIII shows the resultant electrical resistivity data after these various exposures. The "as received" resistivity of the tubing was 73 x 10^{-6} Ω-cm for all samples used.

TABLE XIII. Corrosion of Type 304 Stainless Steel

	Air-exposed		Sodium-exposed	
Exposure Time	Resistivity (ohm-cm x 10^{-6})	% change from "as received"	Resistivity (ohm-cm x 10^{-6})	% change from "as received"
3 days	69	-5.5	70	-4.1
3 days plus Strauss test	73	0	100	+37.0
5 days	67	-8.2	69	-5.5
5 days plus Strauss test	75	+2.7	127	+74.0
7 days	73	0	73	0
7 days plus Strauss test	79	+8.2	267	+266.0

The data indicate that after 7 days in 1200°F air, followed by the Strauss test, the resistance of the specimen increased only 8.2%. By contrast, the sodium-exposed (7 days at 1200°F) sample had a 266% increase in resistance. These measurements are an indication of an as yet unexplained effect of sodium contact on 304 stainless steel at 1200°F. The effect is to leave the specimen very susceptible to attack by the Strauss test.

b. Component and Materials Evaluation Loop (CAMEL). Bus bars were connected from the large EM pump to rectifier units 3 and 4. The blanket-gas analysis system is being installed, and preparations are being made to begin pumping down the entire system.

The portion of the data-acquisition switching system that is used in conjunction with CAMEL has been completed. Checkout of all output signals from the loop is now underway; the Dymec system is used to measure and record all data.

c. Modified Falex Materials Wear Tester. Three modified Falex wear testers have been assembled.

Wear tests continue in inert gas at 1200°F.

The coefficient of friction at elevated temperatures was determined, for an inert atmosphere and a bearing load of 250 psi, for the bearing combination of chill-cast Haynes Stellite Alloy #19 as wear blocks, and Carboloy 78B (83% WC, 8% TiC, 9% Co) as the shaft. Results are as follows:

Coefficient of Rolling Friction	Temp (°C)
0.950	25
0.860	300
0.552	450
0.312	550
0.194	650

The coefficient of rolling friction decreases as the temperature increased. Two factors contributed to this trend. First, the hardness of the stellite alloy decreases from a Brinell 512 at room temperature to a Brinell 372 at 1200°F. Second, the formation of minute oxides due to commercial argon is accelerated as the temperature is increased. It is believed that any oxides on the surface of the bearing materials have the tendency to act as lubricants.

d. Behavior of Carbon in Liquid Sodium

(i) Solubility of Carbon. Previous attempts[7] to determine the solubility of graphite in liquid sodium gave values which scattered erratically. The results indicated that (a) carbonaceous particulates capable of passing through a 5 μ-porosity stainless steel filter pre-existed in the sodium, (b) additional nonfilterable carbon could be dispersed in liquid sodium, and (c) there was no evidence to support the existence of an equilibrium solubility of graphite, as reported by Gratton.[8] The presence of particulate (submicron-sized) carbon in sodium has since been confirmed by ultracentrifugation,[9a] zone-melting,[9b] filtration,[9c] and dissolution[9d] experiments. New solubility experiments using sintered agglomerates ($>>5\ \mu$) of C^{14}-labeled amorphous carbon as the source of carbon are now being conducted. Preliminary results indicate a solubility of less than 0.3 ppm carbon in sodium for the range 193 to 425°C.

(ii) Adsorption of Carbon. It was previously reported[9b] that after reactor-grade sodium was zone melted in fused silica tubing for 240 cycles, its carbon content (30 to 40 ppm) was concentrated at the fused silica/solid sodium interface. This apparent surface or adsorption effect is being investigated further.

---

[7] Chemical Engineering Division Semiannual Report, ANL-6925, May 1965, p. 92.

[8] Gratton, J. G., Solubility of Carbon in Sodium at Elevated Temperatures, KAPL-1807 (June 30, 1957).

[9] Reactor Development Program Progress Reports: (a) February 1966, ANL-7176, p. 43; (b) April 1966, ANL-7204, p. 31; (c) February 1965, ANL-7017, p. 70; (d) January 1965, ANL-7003, p. 23.

The zone-melting experiment was repeated, but for only 25 cycles, and a carbon distribution essentially identical to that of the 240-cycle experiment was found. Since these experiments, it has been learned that the zone-melting technique is not essential for producing the adsorption effect. Reactor-grade sodium was alternately melted and frozen between 200 and 40°C for 300 cycles in a horizontal fused silica tube about 20 in. long. Analyses showed that the total carbon concentration along the sodium core varied from 3 to 13 ppm, whereas about 7 to 30 times this concentration was associated with the sodium at the tubing wall. Subsequent experiments (see Progress Report for July 1966, ANL-7245, p. 21), in which liquid sodium was drawn up or poured into fused silica tubes and allowed to freeze, have indicated that the carbon is rapidly concentrated at a fused silica/solid sodium interface. A similar result was found with stainless steel tubing, indicating that the adsorption is not restricted to fused silica surfaces.

Various mechanisms can be postulated to explain these observations; experiments to sort out these mechanisms are under way.

F. Design Concept Analyses and Advanced Systems Evaluation

1. 1000-MWe Study

Proposals to perform design studies for a 1000-MWe Liquid Metal Fast Breeder Reactor (LMFBR) were received from the following:

Atomics International;

Babcock and Wilcox Company;

Combustion Engineering, Inc.;

General Electric Company;

Westinghouse Electric Corporation.

The proposals were evaluated by ANL and transmitted to the AEC along with recommendations regarding technical administration and fiscal control of the program.

Upon review of the above information, the AEC stipulated the funding available for the follow-on program, and requested ANL to develop with each company a revised program commensurate with the funding.

ANL is now engaged in meetings with individual contractors to review their proposals. These meetings will identify in detail the program to be followed by each contractor. The defined program will provide maximum return in areas of the contractor's greatest capabilities.

II. GENERAL REACTOR TECHNOLOGY

A. Applied and Reactor Physics Development

1. Adjustable Paralysis Discriminator for Fast-Slow Coincidence Experiments

Nuclear experiments frequently require instrumentation capable of determining precisely both the amplitude and time of occurrence of detector pulses. On one hand, the extensive decay times associated with inorganic scintillators (and some other detection devices) warrant imposition of a fixed overriding paralysis, partly to allow sufficient integration time to process a "slow" signal in order to make an amplitude decision (such as in a single-channel analyzer), partly to prevent retriggering of a discriminator during the pulse duration, and partly to permit accurate calculation of the deadtime correction factor. On the other hand, timing information must be preserved for fast coincidence analysis. Superimposed on these requirements is the fact that the analysis of accidental and instrumental coincidences is greatly simplified if the paralysis accompanying the slow energy-selected pulse is also applied to the fast timing pulse.

These considerations have led to the development of the Adjustable Paralysis Discriminator (APD). Figure 13 displays the internal logic of the APD, which is a negative pulse discriminator with an adjustable and well-defined nonextendable paralysis. Ambiguity in output pulse width and

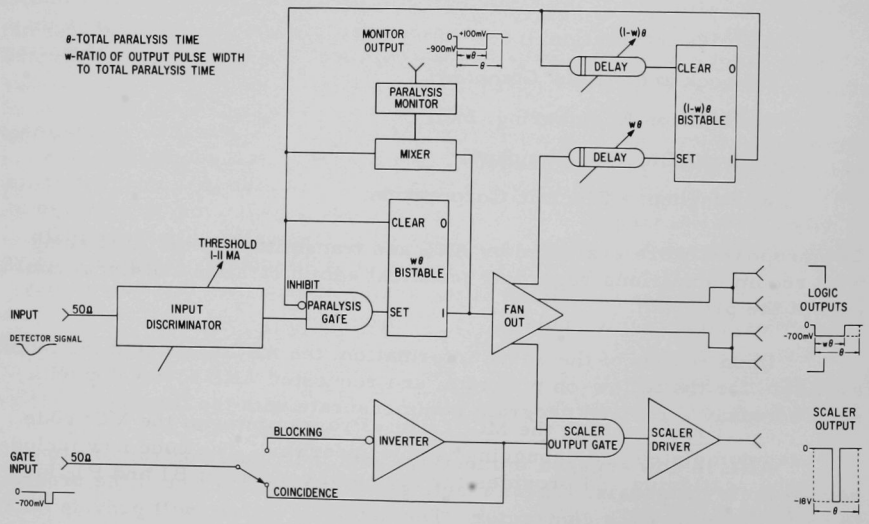

Fig. 13. Internal Logic Diagram for APD

paralysis is minimized by use of 100-MHz logic for the internal circuitry. Input impedance is 50 ohms. The discriminator threshold is continuously adjustable from 1 to 11 mA, with integral nonlinearity of ±0.5% for pulses with risetime greater than 10 nsec. The input is sensitive to negative pulses as narrow as 5 nsec.

The paralysis time (θ) of the APD is continuously adjustable over the range from 0.1 to 10 μsec by means of an internal potentiometer. The range can be shifted even up to the millisecond region by insertion of an appropriate timing capacitor. The ratio (w) of the output pulse width to the paralysis time is also continuously adjustable from 0.3 to 0.7 by means of another internal potentiometer. Adjustment of θ and wθ is facilitated by observation of the waveform at the monitor output (see Fig. 13). Variation in the paralysis time and pulse width at a fixed temperature is less than ±1%, even for pulse pair separations approaching θ, and variation over the temperature range from 0 to 50°C is less than 10%.

Each discriminator provides two pairs of "logic" outputs and a "scaler" output. The dual-output pulse amplitude is -700 mV when both outputs of the pair are terminated in 50 ohms, and -1.4 V when only one output is terminated. Since the outputs are current sources, delay line clipping may be used with each pair independently clipped.

The total circuit delay for input pulses well above threshold is 10 nsec, and the logic pulse risetime is less than 2 nsec. The scaler output pulse amplitude is -18 V into a high impedance or -4 V into 50 ohms, with risetimes less than 20 and 10 nsec, respectively; a silicon diode may be used across the scaler output to limit peak amplitude to -1 V, resulting in a risetime as fast as 3 nsec.

The gate input may be set for "blocking" or "coincidence" (by means of a toggle switch); if "blocking," a scaler pulse is issued concurrently with the logic output unless -700 mV is provided at the gate input; if "coincidence," the scaler pulse appears only as long as -700 mV is provided at the gate input. Both the fast logic output and the scaler output originate at the same time, but only the scaler output is affected by the gate requirement. If the limiter is utilized at the scaler output, then this output may be used as gated "logic" pulse.

2. The ARC System

a. Programming the MC^2 Code. Programming of the MC^2 code has been completed and debugging is now underway. The code now includes hydrogen scattering and provides the option of consistent B1 and P1 flux calculations.

A change has been made in the integration procedure for the resolved resonance region. The code still uses the Romberg integration algorithm, but separate convergence of the integrals is now required for the reaction rate and the flux. The previous version of the code converged on the effective cross section directly. The change was prompted by the observation that in certain cases, large errors in the resulting resolved resonant cross sections could occur due to spurious low-order convergence of the Romberg integration sequence.

The Phase I ARC system will include the present calculational detail of the MC^2 code but with the various subroutines organized into computational modules. This division of the code into a number of modules each of restricted scope permits the ARC user to study a particular type of cross section without the need for running a complete MC^2 problem.

b. Burnup Package Development. A phase-zero burnup package has been designed for the purpose of testing calculation strategies to be used in the first ARC version. The model has been greatly simplified to reduce the initial programming effort; however, the concepts and methods are very similar to those described earlier. The following is a list of capabilities and limitations of the model:

(i) zero-dimensional neutronics;

(ii) one charged fuel isotopic composition (i.e., one material);

(iii) reactor operation with or without reactivity control;

(iv) fractional batch fuel management;

(v) equilibrium or nonequilibrium modes;

(vi) equilibrium operation is "single step," i.e., the same fuel management is carried out after each burn step;

(vii) specified reactor power is maintained over the burn step;

(viii) burn time is adjusted to achieve a specified burnup fraction of fissionable isotopes in discharged material;

(ix) burnup tests may be made either on total burnup or on incremental burnup over one step;

(x) charge enrichment is adjusted so that the uncontrolled static effective k reaches a specified value at a given fraction of the burn time;

(xi) charged fuel volume is preserved with changes in enrichment and isotopic distribution;

(xii) each burn step may be divided into a number of subintervals, at the start of which fluxes will be recalculated; a control search may also be carried out to maintain criticality at each of these points in time;

(xiii) full treatment of isotopic chains and fission products;

(xiv) no real-time computations, i.e., no decay-matrix calculation; real time delays in the external cycle are expressed as an integral number of burn steps;

(xv) one reprocessing plant with isotope-dependent recovery and separation fractions for each of two plant effluents, identified as Class 1 and Class 2, respectively;

(xvi) one external feed with isotope-dependent separation fractions as above;

(xvii) fuel fabrications by means of a degenerate form of supply and demand priority tables.

Several main blocks of the computations necessary for the above model have been coded, and logic debugging is proceeding. Current effort is concentrated on writing and testing various combinations of the multivariable searches necessary in the at-power phase of the cycle. Design of the Phase-I burnup package for inclusion in ARC will be determined by the results of tests on the current model.

B. Reactor Fuels and Materials Development

1. Fuels and Cladding

a. Thermodynamic Study of Nonstoichiometry in Urania. Additional measurements of the total pressure of uranium-bearing species and (simultaneously) of the partial pressure of oxygen over urania have been made by the transpiration method.[10] The measurements are conducted with H_2-H_2O gas mixtures which serve, by equilibration, to fix the oxygen partial pressures and thereby control the compositions of the solid phases. The accumulated data at temperatures ranging from 2080 to 2705°K are presented in Figs. 14 and 15.

The isotherms given in Fig. 14 are, in effect, total pressure curves of the uranium-bearing species UO, UO_2, and UO_3, since the contributions from the species O(g) and O_2(g) are negligible. The triangles represent the calculated[10b] total pressures of uranium-bearing species at the hypostoichiometric urania phase boundary. Previous mass-spectrometric

[10]For previous work, see Reactor Development Program Progress Report: (a) November 1965, ANL-7122, pp. 47-50; (b) March 1966, ANL-7193, pp. 58-62.

investigation[11] of the urania-uranium system has shown that UO is the predominant gaseous species in the far hypostoichiometric region, and that its partial pressure decreases rapidly as the oxygen content of the solid increases. Conversely, UO_3 increases in partial pressure as the oxygen content of the solid increases; UO_3 becomes the predominant gaseous species in the far hyperstoichiometric region. UO_2 is the predominant gaseous species over stoichiometric urania. Minima in the total pressures occur in the vicinity of stoichiometric urania. These minima are associated with compositions corresponding to equilibrium congruent vaporization. However, the data are not accurate enough to determine these compositions as precisely as can be done by the experiments described below (see Sect. II.B.1c).

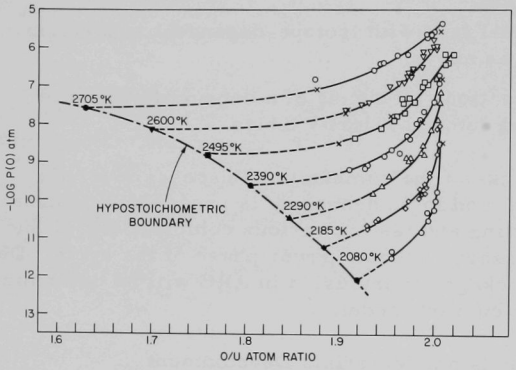

Fig. 14
Total Pressure of Uranium-bearing Species as a Function of Urania Composition (x,o-this work; Δ-calculated, see Ref. 10b)

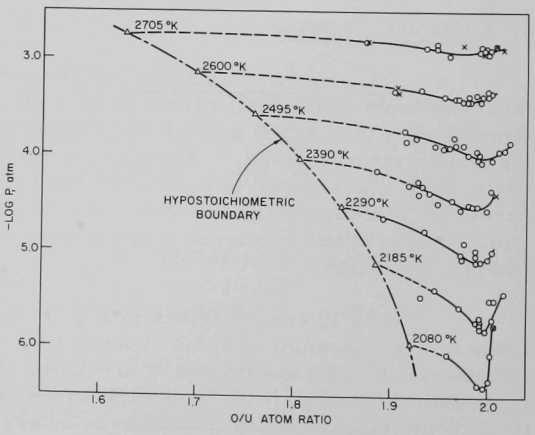

Fig. 15
Partial Pressure of Monatomic Oxygen as a Function of Urania Composition (Open symbols--this work; filled symbols--calculated, see Ref. 10b)

[11]Ackermann, R. J., Rauh, E. G., and Chandrasekharaiah, M. S., A Thermodynamic Study of the Urania-Uranium System, ANL-7048 (July 1965).

The observed partial pressures of oxygen shown in Fig. 15 (open symbols) were computed[10b] from the moisture content of the exit carrier gas streams.[12] The filled symbols give the oxygen partial pressures at the hypostoichiometric urania phase boundary and were calculated.[10b] Of considerable interest is the fact that the isotherms rise less and less steeply at the stoichiometric composition as the temperature increases. This behavior has important consequences for defect models[13] and implies that, at equilibrium, stoichiometric urania is intrinsically disordered with equal numbers of vacancies and interstitials.

The data of Fig. 15 may be used to obtain a preliminary value of ~-58 eu for the relative partial molar entropy of solution of diatomic oxygen in stoichiometric urania in the experimental temperature range. Various values obtained by other workers for hypostoichiometric urania in the range from 900 to 1400°C have been summarized by Hagemark;[14] they seem to extrapolate to the range -7 to 20 eu for stoichiometric urania. It is likely that the experimental values are not equilibrium values because the defect equilibria are very slowly attained in this temperature range.[15]

The study of nonstoichiometry in urania is being written up for journal publication; it is believed that the currently available data can be fitted by an improved model in terms of vacancies, interstitials, and their energies of formation and interaction.

b. The Congruently Vaporizing Composition of Urania. An experimental study of the congruently vaporizing composition(s) of urania was undertaken[10b] to clarify certain disagreements in the literature concerning (a) the vapor pressure of UO_2, and (b) whether UO_2 does or does not vaporize congruently. The experiments were done by vaporizing relatively large amounts of urania from a Knudsen effusion cell into an ultrahigh vacuum, and subsequently determining the O/U ratios of the residues by ignition to U_3O_8. Thus, the principal weaknesses of previous work--insufficient amounts of sample vaporized to reach the congruent composition, and insufficiently low background pressures--were avoided.

The accumulated data between 2025 and 2375°C (±10°C) are shown in Fig. 16, a plot of composition of the urania residues versus temperature. It should be noted that the congruently effusing compositions were

---

[12] Markin, T. L., at Harwell, England, using the H_2-H_2O equilibration technique, has obtained results in good agreement with those shown in Fig. 15 (private communication).

[13] Anderson, J. S., Nonstoichiometric Compounds, Advances in Chemistry Series, No. 39, American Chemical Society, Washington, D. C., 1963, Ch. 1, p. 6.

[14] Hagemark, K., KR-67, Institutt for Atomenergi, Kjeller Research Establishment, Kjeller, Norway (Feb 1964).

[15] Thom, R. J., and Winslow, G., J. Chem. Phys. 44, 2632 (1966).

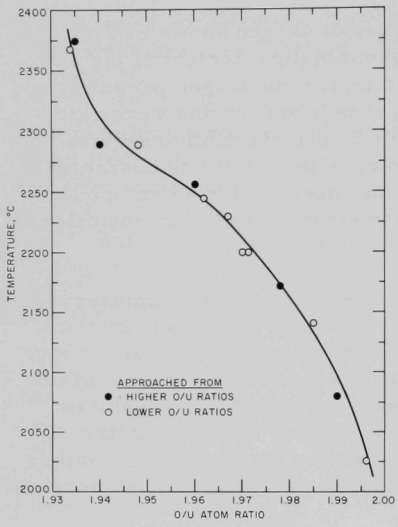

Fig. 16. Compositions of Congruently Effusing Urania

approached from both higher and lower initial O/U ratios, which indicates that constant compositions had been attained. The data show that the congruent composition varies with temperature and that, at elevated temperatures, congruently vaporizing urania is hypostoichiometric.

c. Properties of Uranium Compound Systems

(i) UP-UAs System. Compositions were prepared in the UP-UAs system and were fired at 1800°C in vacuum. X-ray analysis showed complete solid solubility in the system. A plot of lattice constant versus mole percent UP yielded a straight line that essentially conformed to Vegard's law. This supersedes a previous result of a negative deviation from linearity. Metallographic examination also revealed a single phase across the entire system. Oxygen contents were of the order of 0.10 w/o and secondary UO_2 phase was not observed metallographically. Melting temperatures were obtained in a tungsten, "V" furnace. The melting point of UP was 2610°C and that of UAs, 2450°C. The liquidus temperatures showed decreasing values with increasing mole concentrations of UAs. X-ray analysis of melted samples revealed that arsenic was preferentially lost from solid solutions and metallic uranium was formed. The presence of 5 to 10 w/o uranium upon melting might have been responsible for the concave downward shape of the liquidus curve; preferential loss of arsenic should have given an apparent convex upward shape to the curve.

(ii) US-UAs System. Compositions in the system US-UAs were prepared and fired at 1800°C in vacuum. X-ray analysis showed complete solid solubility in this system. Lattice constants for the starting compositions are shown in Table XIV.

Metallographic analysis showed complete solid solubility, but also showed secondary oxide phase. UOS was observed in the US sample along with small amounts of UO_2, but

TABLE XIV. Mixed Uranium Anion Systems

Starting Composition (m/o US)	Lattice Constant (Å)
0	5.777
14.1	5.748
27.9	5.705
41.0	5.663
53.7	5.623
65.8	5.592
77.8	5.557
88.2	5.523
100	5.589

UO_2 was the only second phase that occurred in compositions with high UAs contents. Oxygen contents averaged about 0.15 w/o, and oxide contents did not exceed 2 w/o.

Melting temperatures were obtained for samples in the system, and the liquidus curve was a straight line connecting the melting points of the end members. The line had essentially zero slope, since melting points for both compounds were virtually the same, 2450 ± 20°C. X-ray analysis of melted samples also showed preferential vaporization of arsenic with respect to sulfur and uranium. Melted samples contained metallic uranium and higher S/As ratios after melting than before. The presence of uranium did not result in a concave downward liquidus curve in this case.

d. Thermal Stability of PuO_2. Evaporation rate measurements on PuO_2 with the glovebox thermogravimetric analysis apparatus were begun. The PuO_2 experiments are preliminary to a similar study on mixed uranium-plutonium oxide compositions.

The first part of the PuO_2 work involved fabrication of specimens from high-purity PuO_2 obtained from Los Alamos as a fine, hygroscopic powder. Attempts to press the as-received powder into pellets were unsuccessful; pellet density and strength were poor. Therefore, a calcination procedure was adopted to increase particle size and to remove adsorbed gases.

The first calcination run was made with the PuO_2 powder in an alumina boat at 1000°C in a helium-oxygen atmosphere. An unexpected, but extensive, reaction occurred between the powder and boat; the boat cracked, and the powder was discolored in the contact zone. The powder was successfully calcined by heating it in a platinum boat at 1000°C in a helium-1 v/o oxygen atmosphere.

The pellet-forming procedure included grinding the calcined powder, passing the powder through a 325 mesh screen, adding 1 w/o Carbowax 4000 binder dissolved in ethyl alcohol, and pressing at 60,000 psi. The pellets weighed about 2 g each and had good green strength. The pellets were fired in situ during the evaporation runs.

It was unclear from a literature search whether PuO_2 would react significantly with tungsten or molybdenum in vacuum at the temperatures of the evaporation experiments. Preliminary runs were therefore made to determine the compatibility of these metals with PuO_2.

In the first firing of a pellet on a tungsten plate at 1610°C, severe reaction occurred with the pellet becoming firmly stuck to the tungsten plate. Figure 17 shows the results of several weight-loss runs with PuO_2 pellet and powder on tungsten and molybdenum setter plates in a tungsten

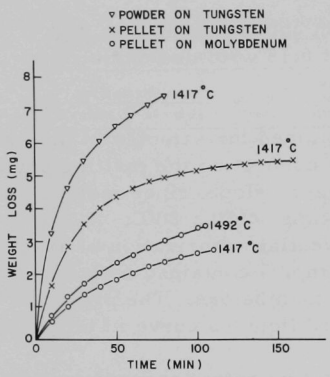

Fig. 17. Weight Loss vs. Time for PuO_2 Resting on Tungsten and Molybdenum Plates in a Tungsten Crucible

crucible. The powder run was made to determine if the reaction resulted from the presence of binder in the pellet. Weight-loss measurements of the setter plates, crucible, and specimens showed that reaction occurred in each run. It is evident from the figure, however, that molybdenum was less reactive than tungsten.

That the weight-loss was partially due to decomposition of the PuO_2 was demonstrated by reoxidation of the pellet after evaporation. Reoxidation of the PuO_{2-x} to PuO_2 was accomplished by heating the pellet for one hour in helium-1 v/o oxygen at 1200°C. Oxygen-to-metal ratios, which were determined gravimetrically, ranged from 1.967 to 1.986.

The evaporation experiments done thus far have shown that the weight-loss contribution from reaction is considerably greater than that from oxygen loss. A suitable container material must therefore be found before meaningful oxygen-loss data can be obtained. The reactive nature of PuO_2 makes the container problem formidable. Experiments are under way to determine whether iridium is compatible with PuO_2.

e. Thermal-diffusivity Equipment for Ceramic Materials. Thermal-diffusivity measurements have been extended to temperatures close to 1500°C by the use of a laser in conjunction with a tantalum heater furnace. A lead sulfide detector is employed as a temperature-sensing device and appears to function well between 300 and 1500°C. Measurements in this temperature range have been carried out on UO_2 and the results are shown in Fig. 18. Although there is still considerable scatter, good agreement is found between ANL data and values in the literature.

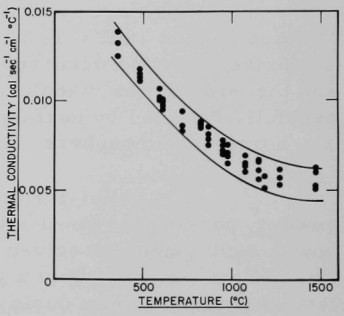

Fig. 18. Thermal Conductivity of UO_2 as a Function of Temperature

f. Irradiation of High-temperature Materials. A series of irradiations in instrumented capsules in the MTR are in progress on ceramic fuel materials, presently carbides and sulfides, being developed under the high temperature materials program. A summary is shown in Table XV.

TABLE XV. Status of Ceramic Fuel (Clad in Nb-1 w/o Zr) Irradiations in MTR

Capsule or S/A No.	Specimen Number	Design Parameters: Fuel Composition (w/o)	Effective Density (%)	Cladding OD (in.)	Clad Thickness (in.)	Operating Conditions: Power Density (kW/cc)[a]	Max Clad Temp (°C)	Burnup to Date: a/o (U + Pu)	fiss/cc x 10^{-20}[a]
56-11	MV-2	UC-20 PuC	79	0.281	0.012	1.2	470	5.8	15.0
56-8	MV-3	UC-20 PuC	81	0.281	0.012	1.2	715	6.3	16.7
56-8	MV-5	UC-20 PuC	80	0.281	0.012	1.2	705	6.0	15.7
56-11	MV-6	UC-20 PuC	80	0.281	0.012	1.2	480	6.3	16.5
56-13	Z-4	UC-20 PuC	79	0.174	0.015	1.2	665	1.2	3.1
56-13	Z-5	UC-20 PuC	79	0.174	0.015	1.2	585	1.2	3.1
56-13	Z-7	UC-20 PuC	79	0.174	0.015	1.2	570	1.2	3.1
56-13	C-45	PuC	84	0.174	0.009	1.4	700	1.2	3.3
56-8	S-7	US	80	0.281	0.012	1.0	535	4.6	8.9
56-8	S-8	US	89	0.281	0.012	1.0	725	6.6	14.2
56-8	S-9	US	76	0.281	0.012	1.0	750	6.6	12.2
56-8	S-10	US	91	0.281	0.012	1.0	690	6.6	14.6
56-11	S-15	US	82	0.281	0.012	1.0	380	3.7	7.7
56-11	S-16	US	90	0.281	0.012	1.0	510	5.6	12.2
56-11	S-17	US	88	0.281	0.012	1.0	500	4.3	9.3
56-11	S-18	US	77	0.281	0.012	1.0	610	6.1	11.4

[a]Based on effective density.

g. Dissolution Kinetics in Liquid-metal Systems. Internal-friction techniques for the determination of interstitial element concentrations in refractory metals are being developed. This method appears to be a very sensitive indicator of impurity level at low concentrations (i.e., a few ppm by weight).

Literature on internal friction indicates that the interstitial-element concentration of bcc metals is a linear function of the heights of specific internal-friction peak. Present work has involved the determination of this relationship for the tantalum-oxygen system by correlating heights of internal-friction peak with data for vacuum-fusion analysis at high oxygen levels where the fusion data are relatively good. The peak heights at low oxygen levels (<50 ppm by weight in tantalum) will then be obtained by extrapolation of the vacuum fusion data to zero.

Results to date indicate a primary oxygen peak at 134°C with a frequency of 0.28 cps. Internal friction peak heights of 4.1×10^{-3} were obtained for samples containing 74 ± 5 ppm oxygen. An internal friction peak of 1.9×10^{-3} corresponds to ~34 ppm oxygen, and peaks of 0.42×10^{-3} and 0.18×10^{-3} were obtained for samples listed as <20 ppm by vacuum fusion analysis. Oxygen levels of <20 ppm are generally not measurable by the vacuum fusion technique on samples of less than 0.3 g. The advantage of the internal-friction method thus is illustrated.

It is planned to obtain the oxygen content in sodium at very low (<1 ppm) oxygen levels by equilibrating (with respect to oxygen) tantalum wires in the sodium. The partitioning of oxygen between sodium and tantalum can be calculated by standard methods. This procedure will be carried out first at relatively high oxygen (in sodium) concentrations where existing analytic techniques, e.g., vacuum distillation, are satisfactory to demonstrate the validity of the calculations.

The concentration of oxygen in tantalum in equilibrium with oxygen in sodium has been calculated using the following expression (based on the best available, including unpublished, data) for the solubility of oxygen in sodium:

$$\log C(\text{ppm}) = 6.939 - 2801(1/T).$$

TABLE XVI. Oxygen in Tantalum in Equilibrium with 1 ppm (by weight) Oxygen in Sodium

Temperature (°C)	Oxygen in Tantalum (ppm)
600	47.0
700	35.5
800	28.3

The results of this calculation, expressed in ppm oxygen by weight in tantalum in equilibrium with 1 ppm oxygen by weight in sodium, are given as a function of temperature in Table XVI.

These values indicate the potential sensitivity of the proposed method of oxygen analyses.

2. Radiation Damage to Structural Materials

a. Fast-neutron Irradiation of Jacket Materials. The effects of elevated temperature coupled with fast-neutron irradiation on the tensile, creep, creep-rupture, and tube-rupture properties of V-20 w/o Ti, V-15 w/o Ti-7.5 w/o Cr, Inconel-625, Hastelloy-X, and Type 304 stainless steel are being investigated in the exposure range from 1×10^{21} to 1×10^{23} n/cm^2. Forty-four capsules, containing 60 tube-rupture specimens and 458 tensile-type specimens, are being irradiated in EBR-II subassemblies XA07, XA08, XO09, XO10, and XO13 at temperatures between 500 and 670°C. The specimens have accumulated maximum total neutron exposures ranging from 6.5×10^{21} to 3.0×10^{22} n/cm^2. The status and identification of the capsules are given in Table XVII.

3. Techniques for Fabrication and Testing

a. Ultrasonic Instrument and Transducer Development. The evaluation of the three ultrasonic transducer probes, which were fabricated last month, was completed. Following is a summary of the results:

(i) Gulton Industries HDT-31 mixture of lead zirconate-titanate is more sensitive than the PZT-4 mixture of lead zirconate-titanate of Clevite Corp.

(ii) For frequencies of 5 Mcps and higher, a 1.27-cm-long, Fiberglas-loaded epoxy backing without a 30° cone on the end opposite the transducer is sufficient. Addition of this 30° cone or an increase in length does not improve the initial pulse length.

TABLE XVII. Status of Cladding-materials Irradiations in EBR-II

S/A No.	Capsule Number	Design Parameters: Cladding Composition (w/o)	Type of Specimen	No. of Specimens	Specimen Environment	Operating Conditions: Max Specimen Temp (°C)	Exposure to Date (n/cm^2)
XA07	AS-9	V-20 Ti	Tensile	16	Argon-helium	590	3.0×10^{22}
XA07	AS-10	Hastelloy-X	Tensile	16	Argon-helium	590	2.7×10^{22}
XA07	AS-11	304 SS	Tensile	16	Argon-helium	590	2.9×10^{22}
XA08	AS-1	V-20 Ti	Tube-burst	12	Argon-helium	540	2.4×10^{22}
XA08	AS-2	V-20 Ti	Tube-burst	12	Argon-helium	540	2.4×10^{22}
XA08	AS-3	Hastelloy-X	Tube-burst	12	Argon-helium	540	2.5×10^{22}
XA08	AS-4	Hastelloy-X	Tube-burst	12	Argon-helium	540	2.5×10^{22}
XA08	AS-5	304 SS	Tube-burst	12	Argon-helium	540	2.5×10^{22}
XA08	AS-6	V-20 Ti	Tensile	16	Argon-helium	580	2.6×10^{22}
XA08	AS-7	Hastelloy-X	Tensile	16	Argon-helium	580	2.4×10^{22}
XA08	AS-8	304 SS	Tensile	16	Argon-helium	580	2.4×10^{22}
XA08	AS-12	V-20 Ti	Tensile	16	Argon-helium	580	2.3×10^{22}
XO09	AS-14	V-20 Ti	Tensile	13	Argon-helium	670	2.1×10^{22}
XO09	AS-15	V-20 Ti	Tensile	13	Argon-helium	670	2.0×10^{22}
XO09	AS-27	304 SS Hastelloy-X	Tensile	13	Argon-helium	670	2.2×10^{22}
XO10	AS-16	V-20 Ti	Tensile	13	Argon-helium	500	7.9×10^{21}
XO10	AS-17	V-20 Ti	Tensile	13	Argon-helium	500	8.6×10^{21}
XO10	AS-18	V-20 Ti	Tensile	13	Argon-helium	500	7.5×10^{21}
XO10	AS-19	V-20 Ti	Tensile	13	Argon-helium	500	7.9×10^{21}
XO10	AS-20	V-20 Ti	Tensile	13	Argon-helium	500	8.8×10^{21}
XO10	AS-21	V-20 Ti	Tensile	13	Argon-helium	500	10.4×10^{21}
XO10	AS-22	Hastelloy-X	Tensile	13	Argon-helium	500	9.1×10^{21}
XO10	AS-23	304 SS	Tensile	13	Argon-helium	500	10.4×10^{21}
XO10	AS-24	304 SS	Tensile	13	Argon-helium	500	8.8×10^{21}
XO10	AS-25	304 SS	Tensile	13	Argon-helium	500	8.4×10^{21}
XO10	AS-26	304 SS	Tensile	15	Argon-helium	500	8.5×10^{21}
XO13	AS-34	Hastelloy-X	Tensile	9	Sodium	650	7.0×10^{21}
XO13	AS-35	V-20 Ti	Tensile	9	Sodium	650	6.5×10^{21}
XO13	AS-36	V-20 Ti	Tensile	9	Sodium	650	6.3×10^{21}
XO13	AS-37	Hastelloy-X	Tensile	9	Sodium	650	7.0×10^{21}
XO13	AS-38	V-20 Ti	Tensile	9	Sodium	650	7.3×10^{21}
XO13	AS-39	V-20 Ti	Tensile	9	Sodium	650	7.0×10^{21}
XO13	AS-40	V-20 Ti	Tensile	9	Sodium	650	7.3×10^{21}
XO13	AS-41	V-20 Ti	Tensile	9	Sodium	650	6.5×10^{21}
XO13	AS-42	V-15 Ti-7.5 Cr	Tensile	9	Sodium	650	6.5×10^{21}
XO13	AS-43	V-15 Ti-7.5 Cr	Tensile	9	Sodium	650	6.8×10^{21}
XO13	AS-44	V-15 Ti-7.5 Cr	Tensile	9	Sodium	650	6.8×10^{21}
XO13	AS-45	V-15 Ti-7.5 Cr	Tensile	9	Sodium	650	6.5×10^{21}
XO13	AS-46	Hastelloy-X	Tensile	9	Sodium	650	7.3×10^{21}
XO13	AS-47	304 SS	Tensile	9	Sodium	650	7.5×10^{21}
XO13	AS-48	304 SS	Tensile	9	Sodium	650	7.3×10^{21}
XO13	AS-49	304 SS	Tensile	9	Sodium	650	7.3×10^{21}
XO13	AS-54	V-15 Ti-7.5 Cr	Tensile	9	Sodium	650	6.8×10^{21}
XO13	AS-55	V-15 Ti-7.5 Cr	Tensile	9	Sodium	650	7.0×10^{21}

(iii) Addition of a 30° cone (2.22 cm long, -500 mesh, 65.5% dense) in sintered nickel backing material at the end opposite the transducer increases the attenuation. The higher attenuation produces a shorter initial pulse.

b. Development of a Neutron-image Intensification System. The possibility for using the neutron-image intensifier for neutron-diffraction applications has been more fully explored. As a detection method for neutron diffraction, the neutron-image intensifier would offer many of the advantages that are realized by the use of similar devices in the X-ray

diffraction field. Rapid orientation of crystals could be accomplished.[16,17] In addition, because of the speed of recording or observing a pattern, diffraction patterns could be obtained from samples that would not remain stable long enough for a conventional diffraction analysis. Dynamic studies could also be made, in that changes could be continuously observed while a sample was heated or subjected to some other variation.[17]

For direct visual observation of diffraction patterns, one needs a reasonable intensity in order to observe small diffraction spots. The detail that can be observed at any given neutron intensity can be calculated. The size of the neutron spot that can be observed at a given neutron intensity depends upon the number of neutrons actually contributing to the image during the time the image information is accumulated, and upon the variation in the number of quanta in the image that will permit observation of the signal. The permissible variation for a useful visual signal has been reported[18,19] to be between three and five.

For visual observation of the neutron image at the output phosphor of the intensifier tube, one can use the following factors: accumulation time of the signal is 0.2 sec; number of neutrons contributing to the image is 15% of those incident on the intensifier tube (allowing 50% absorption in the intensifier tube window and 30% absorption in the neutron scintillator); minimum observable signal-to-noise ratio is three. Neutron beam sizes that should be detectable lie above the line B in Fig. 19; those that should not be detectable lie below line B. The straight line A, for a beam size of 0.35-mm diameter, is the limiting resolution of the present image-intensifier tube. Line C represents the shift in the visible--not visible dividing line if the neutron attenuation in the image intensifier-tube window could be eliminated. In that case, 30% of the incident neutrons would contribute to the image. This represents a situation that should be possible. Line D represents the improvement that would be possible if all of the incident neutrons contributed to the image, the ideal situation.

Also shown in Fig. 19 is an experimental curve obtained in a test in which the output phosphor screen was directly observed through a binocular optical system[20] by several observers. The neutron beam sizes reliably observed at several neutron intensities are shown; the data correlate well with the dividing line formed by lines A and B.

---

[16]Euler, F., Device for Rapid Orientation of Crystals by Direct-image X-ray Techniques, U. S. Air Force Report, AFCRL-66-106 (Feb 1966).

[17]Kennedy, S. W., Rapid X-ray Diffraction Studies Using Image Intensification, Nature 210, 936 (May 28, 1966).

[18]Sturm, R. E., and Morgan, R. H., Screen Intensification Systems and Their Limitations, Am. J. Roentgenology and Radium Therapy 62, 617 (1949).

[19]Morton, G. A., Image Intensifiers and the Scotoscope, Applied Optics 3, 651 (1964).

[20]The optical system was loaned for this test by the Picker X-Ray Corp.

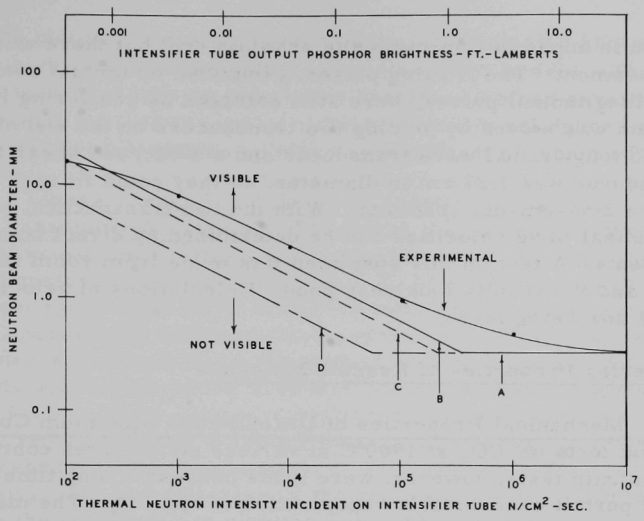

Points above line B should be observed; those below line B should not. Line C represents the improvement to be expected if the neutron absorption in the window of the intensifier tube were eliminated, and line D represents the ideal case in which all the incident neutrons contribute to the image. Line A is the resolution limit of the present tube (0.35 mm). The experimental data, obtained by direct observation of the intensifier tube output screen with a 3X optical system, correlate well with lines A and B, the predicted threshold values for this intensifier tube.

Fig. 19. Neutron Beam Sizes Which Should Be Detectable for a Given Neutron Intensity with a Neutron Image Intensifier Tube

Figure 19 can be used to estimate whether a diffraction pattern can be observed directly, or whether some additional storage element would be needed in the system. For a diffraction spot having a diameter of 3 mm, line B indicates that it should have an intensity of 10^4 n/cm^2-sec or greater in order to be detectable visually with the neutron intensifier tube. Such a diffraction spot could be anticipated by a reflection from a single crystal sample in a monochromatic beam having an intensity of 10^6 n/cm^2-sec; such diffraction spots have been visually observed at CP-5. If the spot were a weak Laue spot, on the other hand, an intensity of about 10^{10} n/cm^2-sec would be necessary at the sample. For cases in which this intensity was not available, the detection could be accomplished by increasing the time during which the signal information accumulates, for example, by photographing the output screen with an exposure time greater than 0.2 sec. Electronic neutron-diffraction detection systems with television or small detector arrays also appear feasible for use with the neutron image intensifier.

c. Determination of Elastic Moduli of High-temperature Materials by Ultrasonics. A rod of V-15 w/o Ti-7.5 w/o Cr (see Progress Reports for May 1966, ANL-7219, p. 47, for June 1966, ANL-7230, p. 38) was

remachined in hopes of improving the echo pattern, but there was no noticeable improvement. The trailing pulses, generated by mutual conversion of shear and longitudinal pulses, were still confused by scattering in the rod. The problem was solved by placing two transducers on the end of the rod--a 5-Mc/sec longitudinal wave transducer and a 5-Mc/sec shear transducer. Each transducer was 1.27 cm in diameter, so they could fit next to each other on the 2.54-cm-dia specimen. With the two transducers, both shear and longitudinal wave velocities can be determined by direct transit-time measurements. A test on this specimen was made from room temperature to 1150°C, and the results look very good. Calculations of velocities and moduli are now being made.

4. Engineering Properties of Reactor Materials

a. Mechanical Properties of Uranium and Plutonium Compounds. Deformation tests on UO_2 at 1900°C at various strain rates continue. No slow-rate strain tests, however, were made because a long time at temperature would permit considerable vaporization of the UO_2. The maximum stress continues to decrease with increasing temperature at medium strain rate. A slight increase in the value for maximum stress was observed when a fast strain rate was used.

Facilities are being developed for determining high-temperature mechanical properties of plutonium compounds. The furnace that has been used for similar measurements of uranium compounds will be modified for glovebox operation. A new method of mounting the radiation shields and a new power supply to the split tungsten mesh element have been developed. Space limitations have dictated a new door-hinging assembly.

An Instron low-speed universal testing instrument with column separation of 36 in. and crosshead height of 52 in. to accommodate an internally mounted glovebox has been ordered. This unit will have a split console; variable and calibrated speed crosshead drive with automatic pacing; load-cycling controls; zero suppression controls; and an X-Y chart device system for extensometer use. An extensometer that can be attached to the tungsten tooling in the hot zone of the furnace is being developed for glovebox application.

A glovebox to contain the furnace and to be internally mounted on the Instron universal tester has been designed and is being fabricated at ANL. The box will be suspended from the Instron frame, but will be additionally supported by an exterior frame. The furnace will be suspended from the glovebox frame to permit precision alignment of the load testing train.

The four-point loading technique for cross-bending of specimens will continue to be used. It is anticipated that smaller specimens will be

used for the plutonium-containing materials. Plans include the determination of the high-temperature Young's modulus, deformation, and the effect of temperature on plasticity and yield strength. These properties will be correlated with the thermal history, microstructure and other physical characteristics of plutonium, as well as uranium, ceramic compounds.

b. Linear Thermal Expansion of Vanadium, Titanium, Chromium, and Some Vanadium-base Alloys. The linear thermal-expansion characteristics of vanadium, titanium, and chromium (cylindrical specimens of 6.4-mm diameter and 38-mm long) and of V-30 w/o Ti and V-50 w/o Ti alloys (sheet specimens, 38 by 6.4 by 0.8 mm) were determined up to 1000°C. Experimental values of $\Delta L/L_0$ versus temperature were fitted to a second-degree polynomial by the method of least squares. Similar least-squares fits were obtained for V-40 w/o Ti, V-5 w/o Ti-15 w/o Cr and V-15 w/o Ti-7.5 w/o Cr, whose mean linear expansion coefficients were previously reported in the Monthly Progress Report for April 1966, March 1966 and February 1966, respectively (ANL-7204, ANL-7193 and ANL-7176, respectively). The polynomials and the mean expansion coefficients calculated from the equations are given in Table XVIII.

TABLE XVIII. Linear Thermal Expansion of Vanadium, Titanium, Chromium, and Some Vanadium-base Alloys

Material	Density ($g\text{-}cm^{-3}$)	Temp Range (°C)	Mean Linear Expansion Coefficient (10^{-6} °C^{-1})
$\frac{\Delta L}{L_0} = 9.03 \times 10^{-6}T + 1.56 \times 10^{-9}T^2$ (0-1000°C)			
Vanadium	6.08 ± 0.01	0-250	9.42
		0-500	9.81
		0-750	10.20
		0-1000	10.59
$\frac{\Delta L}{L_0} = 8.53 \times 10^{-6}T + 2.08 \times 10^{-9}T^2$ (0-1000°C)			
Titanium	4.51 ± 0.02	0-250	9.05
		0-500	9.57
		0-750	10.09
		0-1000	10.61
$\frac{\Delta L}{L_0} = 3.98 \times 10^{-6}T + 9.38 \times 10^{-9}T^2 - 3.32 \times 10^{-10}T^3$ (100-1000°C)*			
Chromium	7.16 ± 0.01	0-250	5.66
		0-500	7.80
		0-750	9.20
		0-1000	9.85

TABLE XVIII (Contd.)

Material	Density ($g\text{-}cm^{-3}$)	Temp Range (°C)	Mean Linear Expansion Coefficient ($10^{-6}\ °C^{-1}$)
$\frac{\Delta L}{L_0} = 8.90 \times 10^{-6}T + 2.28 \times 10^{-9}T^2$ (0-1000°C)			
V-30 w/o Ti	5.53 ± 0.01	0-250	9.47
		0-500	10.04
		0-750	10.61
		0-1000	11.18
$\frac{\Delta L}{L_0} = 8.59 \times 10^{-6}T + 2.37 \times 10^{-9}T^2$ (0-1000°C)			
V-40 w/o Ti	5.36 ± 0.03	0-250	9.18
		0-500	9.77
		0-750	10.36
		0-1000	10.96
$\frac{\Delta L}{L_0} = 9.75 \times 10^{-6}T + 1.96 \times 10^{-9}T^2$ (0-1000°C)			
V-50 w/o Ti	5.20	0-250	10.13
		0-500	10.51
		0-750	10.89
		0-1000	11.27
$\frac{\Delta L}{L_0} = 8.80 \times 10^{-6}T + 1.96 \times 10^{-9}T^2$ (0-1000°C)			
V-15 w/o Ti-7.5 w/o Cr	5.88 ± 0.02	0-250	9.29
		0-500	9.78
		0-750	10.27
		0-1000	10.76
$\frac{\Delta L}{L_0} = 7.90 \times 10^{-6}T + 3.98 \times 10^{-9}T^2$ (0-1000°C)			
V-5 w/o Ti-15 w/o Cr	6.16	0-250	9.82
		0-500	10.38
		0-750	10.94
		0-1000	11.50

*Reference taken above the magnetic ordering temperature of 37°C.

C. Engineering Development

1. Master-Slave Manipulator Systems

a. Electric Master-Slave Manipulator, Mark E4A. Changes are being made in the Mark E4A to improve its stability (see Progress Report for July 1966, ANL-7245, p. 41). The gear ratios are being changed to correct the slow speed of the master motors with respect to the slave. The required gears are to be delivered by September 19.

Certain electrical changes are being made to broaden the amplifier bandwidth and to correct the force-ratio changes caused by the new gearing. All the required electrical parts are now on hand, and all revisions, both mechanical and electrical, will be completed by late September.

b. Low-inertia Servo Motors for Manipulators. A newly designed, low-inertia, cup-type servo motor, intended for use with a manipulator having over 100-lb load capacity, has been assembled. Preliminary electrical testing has begun.

2. Boiling Liquid-metal Technology

a. Niobium-1% Zirconium Loop. After 800 hr of vacuum chamber operation, the booster pump seals again showed signs of excessive wear. They have been replaced with a new type. Also, an outboard bearing has been installed to reduce the torque load on the original seals.

A check of the liquid nitrogen system shows that the diffusion-pump baffle is consuming approximately 20% more nitrogen than the nominal design load, occasionally running dry over a 65-hr weekend period. Additional capacity will be installed for use during continuous high-temperature loop experiments.

During low-temperature calibration runs with sodium, the differential pressure transducers yielded much lower output voltages than indicated by the original calibration curves. The difficulty has been traced to the eddy-current field in the sodium which fills both sides of the transducer diaphragms. It has been shown that the increased input power to the linear variable differential transformer windings yields usable deflections; modifications are underway.

b. Heater Experiments

(i) Electron-bombardment Heater Experiment. Approximately 500 hr of testing with the 0.030-in.-dia, uncarburized thoriated-tungsten filament have been achieved. Heat fluxes ranging up to 350,000 Btu/hr-ft^2 have been supplied to the anode during both steady-state and transient

testing, with peak sodium temperatures to 1500°F. This includes an emission current range to 5.2 A and a cathode to anode voltage of 7700 V. This experiment is approaching limiting design conditions and will be modified to provide higher heat fluxes for short periods of time. These tests and an evaluation of the electron-bombardment heater study by Eimac Corp. will provide the basis of the final design for use in the Nb-1% Zr loop at 2100°F.

3. General Heat Transfer

a. Heat Transfer in Double-pipe Heat Exchangers

(i) Countercurrent Turbulent Liquid-metal Flow. A series of experiments with the first mercury-to-mercury concentric-tube exchanger was completed. Thirty-five separate runs were made for a range of tube-side flow rates with the annulus-side flow rate held constant. Heat exchanger efficiencies were computed from measured flow rates and inlet and outlet fluid temperatures. Fully developed overall heat transfer coefficients were inferred from detailed measurements of the outer wall temperature distribution by the technique described by Stein[21] and used previously with cocurrent flow experiments.

For each tube-side flow rate, data were obtained for three different inlet temperature differences. The purpose of these "inlet-temperature-difference experiments" is to determine if certain idealizations, such as negligible end conduction and negligible thermal convection, are valid for the test heat exchanger. The analytical investigations are based on these idealizations; if they are valid, heat exchanger efficiencies and overall heat transfer coefficients, as determined by the experiment, will be independent of the inlet temperature difference. The results revealed a significant dependence of these computed quantities on the inlet temperature difference, indicating that one or more of these idealizations are not being satisfied in the experiment. Similar difficulties were experienced with the cocurrent flow experiments, making it necessary to correct experimental results by graphical extrapolation to zero temperature difference.[22] Since the extrapolation procedure is tedious and results in inaccuracies, present efforts are being devoted to eliminating or reducing the effects of the nonidealities.

4. Electrical Connector Shell and Seal Testing

A series of tests were performed in which a connector assembly was subjected to repeated cycles of heating, sodium immersion, removal

[21] Stein, R. P., "A Method for the Determination of Local Heat Fluxes in Liquid-metal Heat Exchangers," in Proceedings of the Conference on Application of High Temperature Instrumentation to Liquid-metal Experiments, ANL-7100 (1966), p. 483.

[22] Merriam, R. L., An Investigation of Liquid-metal Heat Transfer in a Cocurrent Flow, Double-pipe, Heat Exchanger, ANL-7056 (June 1965).

from sodium, opening, and resealing the shell in the test vessel (see Progress Report for June 1965, ANL-7071, p. 9). Temperatures were raised gradually to 400°C in argon and in sodium during each cycle. The inside of the shell was evacuated during the heating periods to monitor leak tightness.

Four consecutive cycles were completed with immersion and "soaking" in the sodium of approximately 12 hr/cycle.

Slight inleakage of gas was detected during temperature cycling in argon, but no leakage occurred when immersed in sodium. The seal was hermetically tight when "soaked" at temperatures above 300°C. No sodium entered the shell at any time during the test period.

It is planned to continue the testing with longer cycles and higher temperatures.

D. Chemistry and Chemical Separations

1. Fluoride Volatility Processes

a. Recovery of Uranium and Plutonium from Low-enrichment Fuels: Laboratory Support Work

(i) Instruments for Plutonium Analysis. An experimental program is under way to develop techniques for remote plutonium analysis based on the counting of neutrons derived from (α,n)-type reactions. Current tests involve the use of He^3 proportional counters for estimating the quantity of plutonium in solid samples. Variations in specific counting rate [counts/(min)(g PuF_4)] with sample size, sample position, and counter position were determined. A large sample of PuF_6 was counted and estimated to contain 94.6 g PuF_6, which is to be compared with 100.9 g obtained by weighing.

(ii) Reactions of UO_2 and UO_3 with BrF_5. The study of the reactions of BrF_5 with various uranium compounds has been concluded with the determination of the kinetics of the reactions of BrF_5 with UO_2 and UO_3. Two types of UO_2 were used in these experiments: material prepared by the reduction of UF_6 by steam-hydrogen mixtures, and high-density sintered UO_2. Both materials were pulverized to -170+200 mesh powder. The reaction of UO_2 with BrF_5 proceeds by the formation of UO_2F_2 which, in turn, is fluorinated to UF_6. The rate of reaction of sintered UO_2 was less than that observed at identical temperatures for UO_2 derived from reduction of UF_6. At 305°C, the reaction rates were 19×10^{-3}/min and 50×10^{-3}/min, respectively. For the reactions with BrF_5, an activation energy of 14 kcal/mole was calculated for the sintered UO_2, whereas a value of

7.5 kcal/mole was calculated for the UF_6-derived oxide. The low value of the activation energy suggests that the reaction is controlled by the formation of UO_2F_2 and depletion of UO_2F_2 by fluorination. (The activation energy for the UO_2F_2-BrF_5 reaction is 8.3 kcal/mole.) In the case of sintered UO_2, the high activation energy suggests the presence of UO_2F_2 and UF_4 (activation energy of the UF_4-BrF_5 reaction is 16.9 kcal/mole) on the surface of the reacting particles. Both UF_4 and UO_2F_2 are formed by the reaction of UF_6 with UO_2. The difference in behavior in the two types of oxide probably arises from the degree of reactivity of the two oxides. The UO_2 derived from UF_6 is rapidly converted by BrF_5 to UO_2F_2 and interaction at the oxide surface with UF_6 is essentially absent, while sintered oxide is more slowly fluorinated to UO_2F_2 and therefore some oxide surface is available for contact with UF_6 to produce UF_4 and UO_2F_2. A value of 7.7 kcal/mole was calculated for the activation energy of the UO_3-BrF_5 reaction.

A series of experiments were performed with UF_6-derived UO_2 and with UO_3 to determine the effect of BrF_5 partial pressure on the rates of reaction. The following equations were derived to represent the temperature and partial pressure dependence of the two reactions:

for the UO_2-BrF_5 reaction, $\log k = 0.84 \log P - (1630/T) - 0.270$;

for the UO_3-BrF_5 reaction, $\log k = 1.05 \log P - (1680/T) - 0.767$.

During the course of this laboratory support program, the kinetics of the reactions between BrF_5 and UF_4, UO_2F_2, U_3O_8, UO_3, and UO_2 were measured. A summary of the data appears in Table XIX in the form of constants for the equations representing the temperature and BrF_5 partial pressure dependence of the rates of reaction.

TABLE XIX. Equations for Estimating the Rates of Reaction of BrF_5 with Uranium Compounds

Rate Equation: $\log k = n \log P - (A/T) + B$;
P in Torr, k in min^{-1}

	UF_4	UO_2F_2	U_3O_8	UO_2	UO_3
n	0.38	0.71	0.90	0.84	1.05
A	3690	1810	2000	1630	1680
B	4.286	0	-0.220	-0.270	-0.767
Activation Energy, kcal/mole	16.9	8.3	9.2	7.5	7.7

b. Recovery of Uranium and Plutonium from Low-enrichment Fuels: Engineering Work

(i) Engineering-scale Alpha Facility. The primary objectives of experiments performed in the engineering-scale alpha facility are to investigate the possible difficulties in handling PuF_6 on an engineering scale and to determine the feasibility of possible fluoride volatility flowsheets. Initial experiments involve the processing of UO_2-PuO_2 fuel containing synthetic fission products; later experiments may be made with low levels of fission product activity. A series of experiments are under way to demonstrate the transfer of PuF_6 in process equipment. Two tests (runs U-8 and Pu-9) were performed in which UF_6 and PuF_6 were vapor-transferred from one vessel to another. In run U-8, 160 g of UF_6 was vacuum transferred from a small supply vessel to a large cold trap (~1 cu ft) maintained at -52°C. The UF_6 was then transferred to a small nickel receiver (800 ml) using nitrogen as the carrier gas. In this operation, the cold trap was heated to 75°C and the UF_6 was swept from the trap by the nitrogen gas stream. The receiver vessel was maintained at temperatures between -38 and -57°C. A small NaF trap was used to collect any UF_6 which passed through the receiver vessel. Approximately 123 g UF_6 was collected in the product receiver and 35.2 g in the NaF trap; collectively, these numbers represent a UF_6 material balance of about 99% in the two transfer operations which is considered to be very satisfactory.

The transfer of PuF_6 (run Pu-9) was performed in the same equipment under the same operating conditions. During the vacuum transfer step, 89.4 g of PuF_6 was transferred to the cold trap. In the second transfer, 74.0 g PuF_6 was collected in the receiver vessel and 13.4 g PuF_6 was collected in the NaF trap. The PuF_6 material balance, taking into account alpha decomposition of PuF_6 at a rate of 2% per day for 8 hr, was 98.4% for the transfer experiment. This result is considered to be highly satisfactory.

(ii) Process Development Studies for Uranium Dioxide Fuels. Pilot-scale studies to demonstrate the use of BrF_5 in the processing of UO_2 fuels are under way in a 3-in.-dia fluid-bed reactor. A run has been performed with 2.2 kg of fragmented UO_2 pellets (fragment size, -0.5+0.13 in.) to evaluate the equipment performance in the pilot-plant facility (run BRF5-1). The UO_2 fragments and 2.9 kg of -60 mesh alumina particles were charged to the 3-in.-dia reactor. The UO_2 was oxidized to U_3O_8 powder by passing a 20 v/o oxygen in nitrogen fluidizing gas stream at a velocity of 1.5 ft/sec through the bed at 450°C for 6 hr. The U_3O_8 fines were fluorinated to UF_6 by reaction with 12 v/o BrF_5 in nitrogen for 2 hr at 300°C. The fluidization gas velocity during fluorination was 0.8 ft/sec. The total quantity of BrF_5 fed to the reactor was 1.5 times the stoichiometric amount to convert the uranium to UF_6 (3.8 kg).

All equipment operated satisfactorily throughout the entire run. The alumina bed material drained freely and was free from agglomerates at the end of the run. The average UF_6 production rate for the entire fluorination period was 65 lb/(hr)(sq ft reactor cross section). Future tests will involve the fluorination of larger quantities of uranium. Of primary interest in these tests will be the establishment of fluorination conditions that avoid the occurrence of temperature excursions.

c. Disposal of Gaseous Fluoride Volatility Reagents. A factorially designed experiment to study the effects of process variables on the capacity of activated alumina for the removal of fluorine from a gas stream in a fluidized bed of activated alumina has been completed. The experiment (16 runs) was performed in a 2-in.-dia fluid-bed reactor. The capacity of the alumina was measured at the time of fluorine breakthrough, that is, the time when the concentration of fluorine in the effluent gas stream exceeds a certain value, such as 200 ppm.

Preliminary interpretation of the data from the experiment indicates: (i) increasing the bed temperature from 300 to 400°C, increasing the bed depth-to-diameter ratio from 3 to 6, and decreasing the alumina particle size from 28-48 mesh to 48-100 mesh were all effective in increasing the capacity of the activated alumina for fluorine disposal; (ii) changing the fluidizing gas velocity (1.25 to 1.65 times minimum fluidizing velocity) and changing the fluorine concentration (from 5 to 10 v/o in nitrogen) has no effect on the capacity of the bed; (iii) there appeared to be no significant interactions among the five independent variables.

d. Chemistry of Tellurium Fluorides. Studies of the reactions of volatile tellurium fluorides are under way to determine the conditions whereby tellurium is fixed on solid materials and to investigate the kinetics of the reaction. Preliminary studies on the sorption of TeF_6 on Linde Molecular Sieve Type 10X indicate that this material is less effective than Linde Molecular Sieve Type 13X (see Progress Report for July 1966, ANL-7245, p. 73) in retaining TeF_6 after sorption; significant quantities of TeF_6 desorbed from Type 10X sieve after 1 hr in vacuum. Silica gel also exhibits poor retention and sorption rate properties for TeF_6.

Tests performed to investigate the reaction of TeF_6 with copper turnings and nickel wool indicated that, at 400 and 500°C, TeF_6 readily reacts with both materials. The reaction of TeF_6 with these materials gave nonvolatile reaction products.

III. ADVANCED SYSTEMS RESEARCH AND DEVELOPMENT

A. Argonne Advanced Research Reactor (AARR)

1. Fuel and Core Development

a. Thermal Conductivity of Irradiated Fuel as a Function of Burnup and Temperature. The flash method of determining thermal diffusivity and thermal conductivity is being utilized to measure the thermal properties of AARR fuel plates. Measurements with the unirradiated material are made from ambient temperature up to 800°C with intermediate measurements at 100°C increments. Twenty samples from five fuel plates have been tested, and the data reduction is in progress.

b. Transient Analysis. Investigatory work necessary for the development of a refined mathematical model to describe the transient behavior of the AARR continued. Calculations were made to determine whether it is necessary to account for the temperature dependence of thermal properties of fuel-plate materials in order that sufficient accuracy is provided in calculations of plate temperatures during transient heating.

Examination of time-dependent temperatures within a typical AARR fuel plate and associated coolant channel was accomplished through the use of a digital computer code, ANL designation RE-322. A detailed, two-dimensional representation of an AARR half-plate and half-channel was developed, consisting of 10 zones along the plate length, each of which comprised 7 nodes through the plate half-thickness plus one in the flowing bulk water. Thus the spatial representation of the plate and water consisted of a total of 80 nodes.

The heat-generation profile along the plate length was assumed to be a chopped cosine function; heat generation was assumed uniform through the half-thickness of the fuel zone. Time dependence of the total heat-generation level was specified by auxiliary calculation of the reactor-power response to various reactivity insertions.

Results have been obtained for a severe transient caused by a step-function addition of $1.50 reactivity to the reactor when operating at a simulated power level of 100 MW. This produces a change in the heat-generation rate by a factor of 50 in approximately 20 ms and a resulting maximum change in fuel temperature of approximately 1700°F in 30 ms. The results obtained for constant and temperature-dependent values of fuel-plate materials were compared on the basis of actual temperature differences and through an estimate of the error which would result in a calculation of feedback reactivity based upon constant thermal properties. These comparisons indicate that the maximum errors incurred due to the use of

constant thermal properties are less than 6% in metal temperatures and less than 3% in coolant temperatures. The feedback reactivity is less than 10% of its total value. It is concluded, on the basis of these results, that the use of constant thermal properties for fuel-plate materials provides adequate accuracy for transient-temperature calculations.

2. Component Development

a. AARR Vessel. It is generally believed that the geometry (radius) of the small fillet at the nozzle-shell junction can have a major influence on the resulting stresses. Unfortunately, the two methods developed under Pressure Vessel Research Committee auspices by E. O. Waters and N. C. Lind and adapted by the ASME Code for the analysis of nozzle connections in spherical shells are both incapable of considering the geometry of the juncture in detail. With the aid of Seal-Shell-2 (Ref. 23) computer program, the stresses in the outlet nozzle connection caused by the internal pressure and thermal loading can now be studied in detail. Several configurations of different fillet size, fillet radius, and corner radius have been analyzed in an effort to arrive at an optimum design having the least stress concentration factor. The most favorable configuration and associated stresses are shown in Fig. 20. The calculated stresses are all below the design limits.

Currently, no computer program is available for the detailed study of the inlet nozzle connection. However, the stresses for a cylindrical shell having nozzles with zero wall thickness have been obtained theoretically by Eringen.[24] Furthermore, an interesting fact can be obtained from comparison of the results of the cylindrical and spherical shells. For example, Fig. 21 shows that the membrane stresses for a sphere as obtained from the Seal-Shell-2 program are almost identical to the membrane stresses along the longitudinal axis of a cylindrical shell having the same $d_m/D_m\sqrt{D_m/T}$ ratio (d_m = mean nozzle diameter, D_m = mean vessel diameter, T = vessel wall thickness) as obtained by Eringen,[24] providing the stresses are reduced by the applicable basic value. The basic values are 2.0 for spheres and 2.5 for cylinders. Since a cylinder with a membrane closure is a limiting case for nozzles having finite thickness, it is believed that the same relationship can apply to nozzles having finite wall thickness or perhaps even to nozzles having a small fillet. Figure 21 shows that for a $d_m/D_m\sqrt{D_m/T}$ ratio of 1.325, the increase of stress from a spherical shell to a cylindrical shell is about 14%. With this comparative information the stresses in the inlet nozzle connection can be deduced from the calculated stress values in the outlet nozzle connection.

[23] Friedrich, C. M., Seal-Shell-2, A Computer Program for the Stresses Analysis of a Thick Shell of Revolution with Axisymmetric Pressure, Temperature, and Distributed Loads, WAPD-TM-398 (Dec. 6, 1963).

[24] Eringen, A. C., Naghd, A. K., and Thiel, C. C., State of Stress in a Circular Cylindrical Shell with a Circular Hole, W. R. C. Bulletin 120 (Jan 1965).

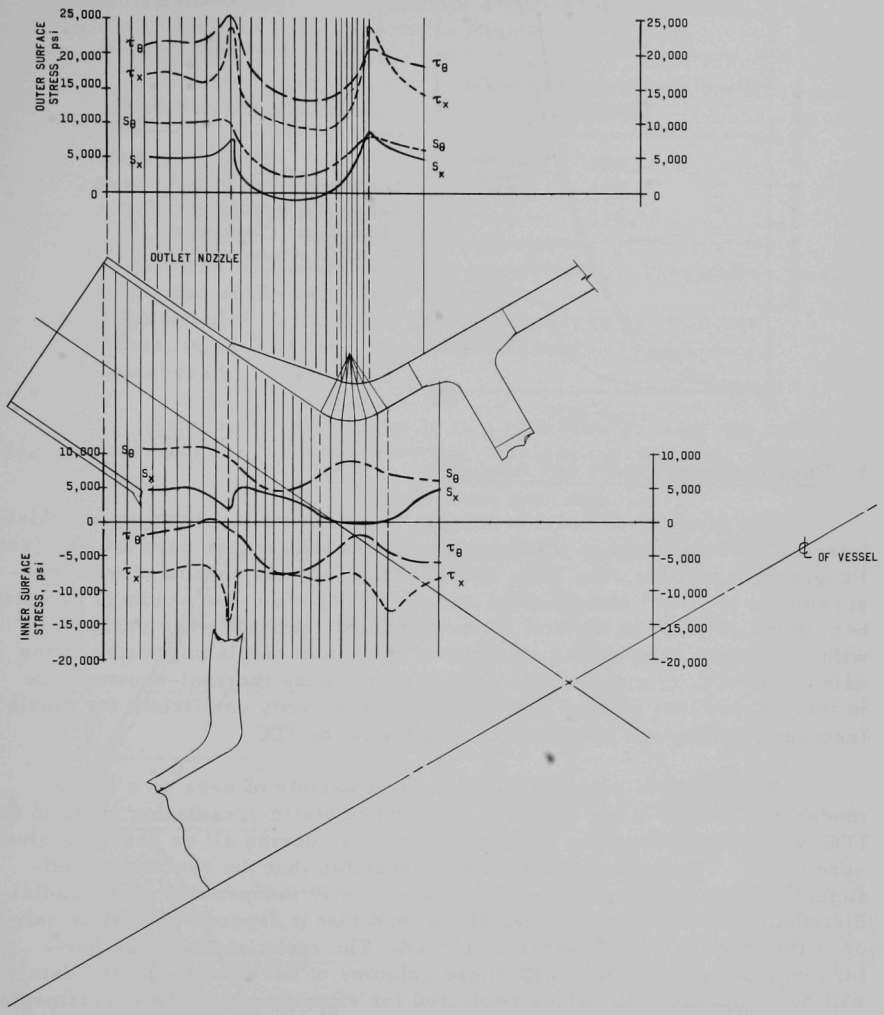

Legend

S_x	Longitudinal Stress Primary & Secondary
S_θ	Circumferential Stress Primary & Secondary
τ_x	Longitudinal Stress Primary, Secondary & Thermal
τ_θ	Circumferential Stress Primary, Secondary & Thermal

Fig. 20. Primary, Secondary, and Thermal Stresses in AARR Reactor Vessel Outlet Nozzle

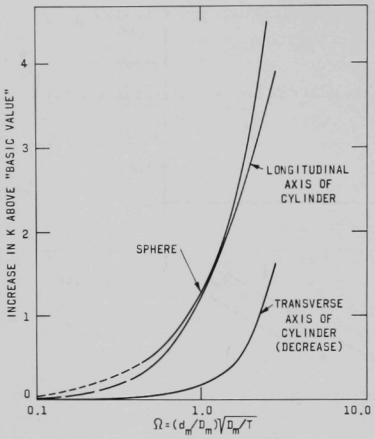

Fig. 21
Comparison of Increase in Membrane Stress in Sphere and Cylinder above "Basic Value" ("Basic value" of K = 2.5 for cylinder and 2.0 for sphere)

3. Physics Experiments and Analyses

The program of reactor physics experiments involving an oversized Internal Thermal Column (ITC) and an 1173/1347 reactor core loading (see Progress Report for July 1966, ANL-7245, p. 48) has continued with measurements of "flux" distributions and reactivity effects of voidings in water, both in the ITC and in the fuel zone. Also, experiments were performed with full-length rectangular columns of beryllium displacing water at the axis of the ITC, to measure the effects on the peak thermal-neutron flux in the ITC per unit reactor power, and the reactivity coefficient for small fractional voidings of the water remaining in the ITC.

Beryllium is being considered for a variety of uses as a solid moderator in part of the ITC, e.g., inserts in static-irradiation tubes in the ITC, when these tubes are not intended for use during all or part of a given core cycle. Theoretical analysis has predicted that the reactivity coefficient of voiding water in the ITC is essentially independent of the radial distribution of the pieces of beryllium, and that it depends primarily only upon the fraction of ITC water displaced. The experiments were performed most conveniently with these columns of beryllium, and the data will be compared with values computed for simulations of the experimental configurations. Later, measurements will be made with beryllium rings at the outer edge of the ITC.

Radial distributions of U^{235} fission were measured with (a) a 1-in.-square column and (b) a 2-in.-square column, of beryllium. These measurements were taken on a plane 3.2 cm below the core midplane, with reactivity control by adjustment of water level in the reactor tank. Table XX summarizes the water levels for criticality:

TABLE XX. Water Levels Controlling Reactivity for the Criticals

Condition of the ITC[a]	Water Level at Criticality[b] (cm)
100% H_2O	120.72
1-in.-square block of Be	120.36
2-in.-square block of Be	118.70

[a]These are full-length rectangular columns of beryllium, centered at the axis of the ITC.

[b]The top of the active fuel zone nominally is at 132.4 cm. Thus, in each of these experiments, part of the fuel was uncovered.

a. Experimental. Figure 22 is a plan view showing the radial locations of foils for radial and vertical traverses of activity. Note that

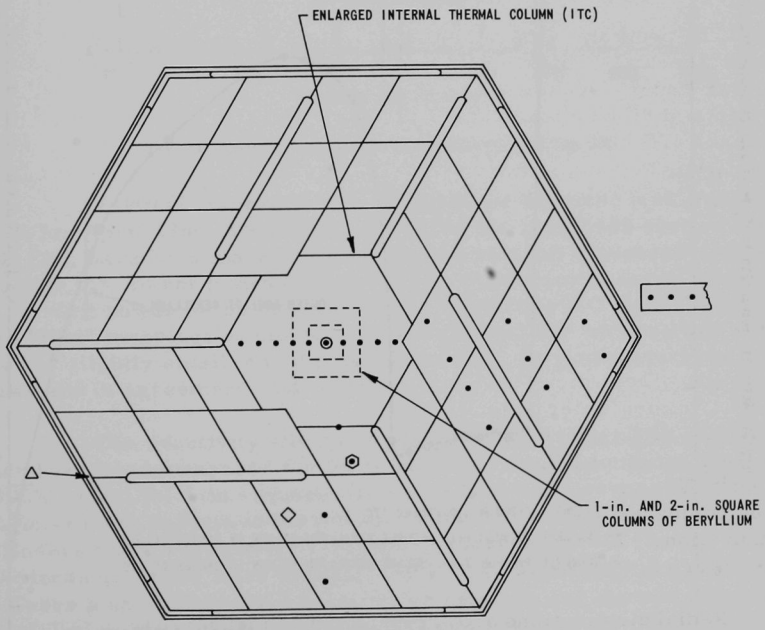

Fig. 22. Radial Locations of Bare Foils for Radial and Vertical Traverses of U^{235}-fission Activity

the boundary of the oversized ITC is somewhat irregular because three fuel assemblies could not be modified reasonably to remove portions of fuel plates.

Figure 23 presents the radial traverses of bare-foil U^{235}-fission activity for the two sizes of beryllium columns in the ITC, normalized to foil activities in the core away from boundaries. Figure 23, and the detail in Fig. 24, show that the beryllium perturbs the traverse essentially only in its immediate vicinity. In the beryllium itself, the flux (traverse) is flat and ~5% (~10%) lower than the peak flux in the 100%-H_2O ITC, when a 1-in.-square (2-in.-square) column of beryllium is present.

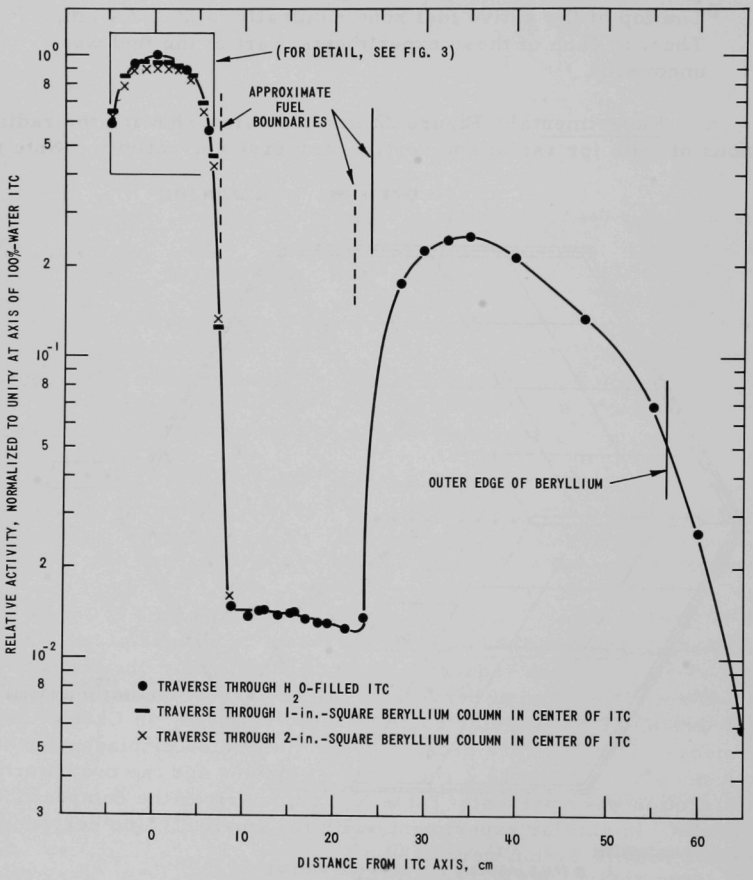

Fig. 23. Radial Traverses of U^{235}-fission Activity of Bare Foils for the 1173/1347 Uniform Loading and the Oversized ITC

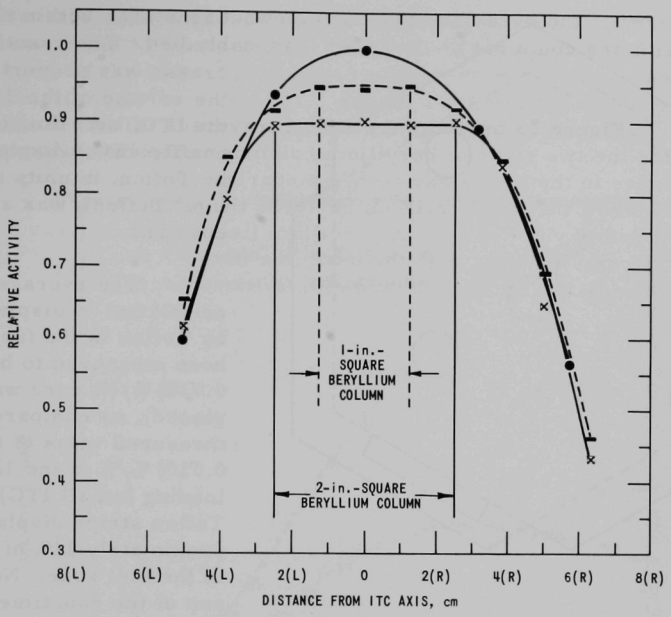

Fig. 24. Detail of Activity Near Axis of ITC (See Fig. 23)

Vertical traverses, similar to those reported (see Progress Report for April 1966, ANL-7204, p. 68) for the 1215/1620 system with the small ITC, have been made. The radial and vertical traverses with the 100%-H_2O ITC do not indicate a substantial difference in the values of peak flux per unit power in the undersized and oversized ITC's. Much more detailed "flux" mappings would be required to establish whether this ratio indeed is slightly smaller in the oversized ITC, as it appears to be. These results are in agreement with theory.

The reactivity effects of replacing part of the ITC water with Teflon have been measured for three different conditions of the ITC: (a) 100% water; (b) 1-in.-square column of beryllium at the ITC axis; and (c) 2-in.-square column of beryllium. Figure 25 shows the locations of the 5 cylinders and 2 rectangular columns of Teflon used. In Case a, above, all 7 pieces of Teflon were present, for a total water displacement of 6.8%. For Cases b and c only the 2 rectangular columns and the two outermost rods of Teflon were present. Table XXI summarizes the compositions and the results. In similar experiments with the small ITC (no beryllium), only the 5 rods of Teflon were used.

As may be seen from Table XXI, the reactivity changes due to the small volumes of Teflon are almost independent of the beryllium content

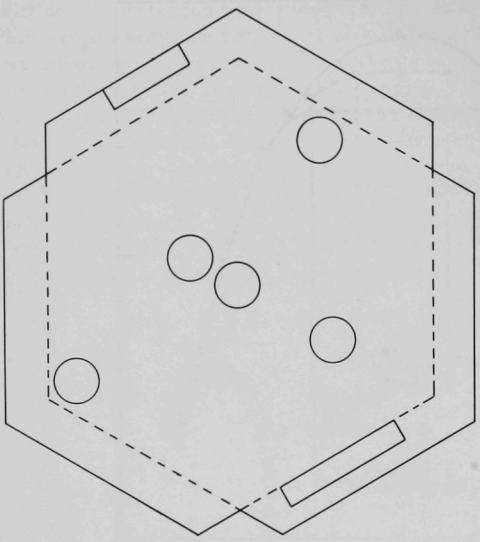

LEGEND:
REGION BORDERED BY DASHED LINE: SMALL ITC (5.9-cm-radius)
REGION BORDERED BY SOLID LINE: OVERSIZED ITC (7.2-cm-radius)

Fig. 25. Locations of Full-length Columns of Teflon in the Two ITC's

of the ITC, within the ranges studied. The reactivity increase was proportional to the volume of the Teflon in the ITC, i.e., the reactivity coefficient of displacing water by Teflon, in units of %/(cm^3 Teflon), was almost constant.

The average reactivity coefficient of displacing water by Teflon in the fuel zone has been measured to be (-0.136 ± 0.010) %/(% core water displaced), as compared with a measured value of (-0.116 ± 0.010) %/% in the 1215/1620 loading (small ITC). The Teflon strips displaced approximately $1\frac{1}{2}$% of the water in the fuel zone. Note that one of the constituents of Teflon, carbon, is a neutron moderator. Thus Teflon is almost, but not quite, equivalent to a gas void. In the ITC, the correction factor is not so large as it is in the core. It has been calculated that, taking the carbon content into account, the reactivity coefficient of air void in the water in the reactor core is approximately 1.1 times the reactivity coefficient of displacement of core water by Teflon.

TABLE XXI. Reactivity Coefficient of Teflon in the Oversized ITC[a]

Plan Areas (cm^2)				
Beryllium	Water plus Teflon	Teflon	Reactivity Change (%)	Reactivity Coefficient of Teflon [%/(% H_2O displaced)]
-	152.3	10.4	0.36	0.053 ± 0.005[b]
6.4	145.9	6.6	0.24	0.054 ± 0.005
25.8	126.5	6.6	0.24	0.047 ± 0.005

[a]Numerical values for areas are rounded off.
[b]This compares with an average coefficient of (0.040 ± 0.005) %/%, in the small ITC.

Measurements were made of the reactivity gains due to partial air voidings of the 100%-water ITC, with void fractions ranging up to 69.4% of the volume of the ITC. These experiments are similar in type to those reported earlier for the small ITC. Figure 26 compares these results with data for the small ITC. The maximum reactivity gain in partial voidings of the ITC is approximately 3%.

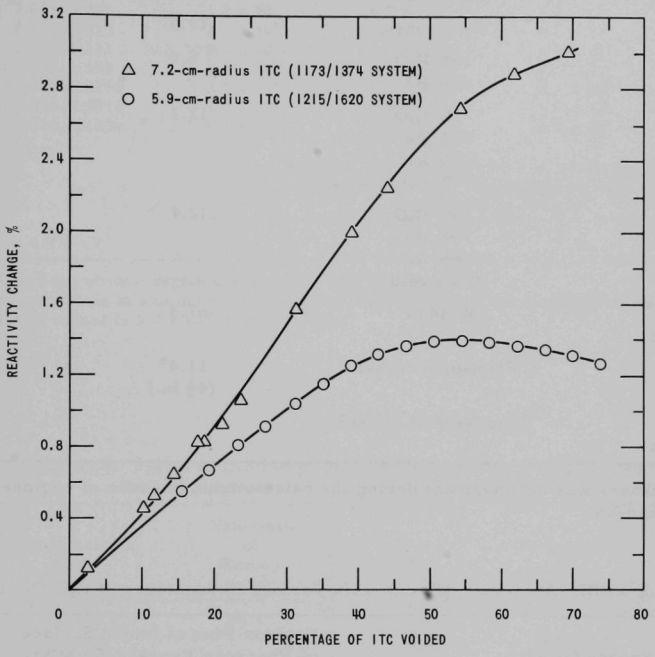

Fig. 26. Reactivity Effects of Partial Voidings of ITC

b. Theoretical Studies. The Progress Report for June 1966, ANL-7230, pp. 50-51, included remarks on a neutron-window configuration, for the reference AARR, which appeared to: (i) reduce the radiation damage rate, to the reactor pressure vessel, to acceptable levels, and (ii) still permit placement of neutron detectors for power-operation instrumentation outside the pressure vessel. A summary of calculations leading to this choice of neutron window is presented in Tables XXII-XXVI. Figure 28, based on Window No. 2 (see Table XXVI), gives radial distributions of the thermal-neutron flux in a 6-in.-thick instrument-tube zone as a function of the material composition of that zone. Clearly, compositions with minimum water volume are most favorable for use because small thicknesses of water are effective in attenuating the source neutrons in the instrument-tube zone.

TABLE XXII. Region Configuration for Neutron-window Calculations

Region Number	Composition of Region	Thickness of Region (cm)	Outer Radius of Region (cm)
1	Fuel zone	10.1	10.1
2	Fuel zone	17.0	27.1
3	10% H_2O 90% Be	5.6	32.7
4	7% H_2O 81% Be 5% Al 7% void	12.2	44.9
5	5% H_2O 79% Be 5.6% Al 10.4% void	12.7	57.6
6: 6a, 6b, etc.	Window	67.3	124.9
7	Pressure vessel	11.4[a] ($4\frac{1}{2}$ in.)	136.3
8: 8a, 8b, etc.	Zone beyond vessel		

[a]This thickness was not invariant during the calculations, because of engineering-design changes.

TABLE XXIII. Aluminum Window with Various Percentages of H_2O (No steel)

Neutron Energy Group		Neutron Flux at Inside Surface of Pressure Vessel (100 MWt) (n-cm/cm^3-sec)			
No.	Energy Range (MeV)	No H_2O	4% H_2O	6% H_2O	8% H_2O
1	6.065-10	2.2×10^7	2.0×10^7	1.9×10^7	1.8×10^7
2	3.679-6.065	1.4×10^7	1.2×10^7	1.2×10^7	1.1×10^7
3	2.231-3.679	2.6×10^7	2.1×10^7	2.0×10^7	1.8×10^7
4	1.353-2.231	7.7×10^7	5.0×10^7	4.2×10^7	3.5×10^7
5	0.8208-1.353	1.7×10^8	8.7×10^7	6.7×10^7	5.4×10^7
6	0.3876-0.8208	1.1×10^9	3.5×10^8	2.2×10^8	1.5×10^8
7	0.1830-0.3876	1.9×10^9	4.1×10^8	2.3×10^8	1.5×10^8
8	0.06733-0.1830	3.6×10^9	5.4×10^8	2.9×10^8	1.7×10^8
		Relative Thermal-neutron Flux at Outside Surface of Pressure Vessel, Normalized to Unity for Case of Full Aluminum Window[a]			
31	0-0.076 eV	1	0.79	0.27	0.11

[a]For case of full aluminum window (no H_2O), computed absolute value of thermal-neutron flux at outside surface of vessel is 6.3×10^{10} n-cm/cm^3-sec.

TABLE XXIV. Aluminum Window Containing Zones of Steel (Iron)[a]

Neutron Energy Group		Neutron Flux at Inside Surface of Pressure Vessel (100 MWt) (n-cm/cm^3-sec)			
No.	Energy Range (MeV)	No Steel	2 in. Steel	4 in. Steel	8 in. Steel
1	6.065-10	2.0×10^7	1.2×10^7	7.1×10^6	2.5×10^6
2	3.679-6.065	1.2×10^7	6.9×10^6	4.0×10^6	1.3×10^6
3	2.231-3.679	2.1×10^7	1.2×10^7	6.7×10^6	2.4×10^6
4	1.353-2.231	5.0×10^7	3.0×10^7	1.9×10^7	8.7×10^6
5	0.8208-1.353	8.7×10^7	5.8×10^7	4.1×10^7	2.3×10^7
6	0.3876-0.8208	3.5×10^8	2.7×10^8	2.3×10^8	1.9×10^8
7	0.1830-0.3876	4.1×10^8	3.3×10^8	2.9×10^8	2.5×10^8
8	0.06733-0.1830	5.4×10^8	4.6×10^8	4.1×10^8	3.3×10^8
		Relative Thermal-neutron Flux at Outside Surface of Pressure Vessel, Normalized to Unity for Case of No Steel in Window[b]			
31	0-0.076 eV	1	0.70	0.52	0.30

[a]Each subregion of the window region contained 4% H_2O by volume.
[b]For case of no steel zone in aluminum window, computed absolute value of thermal-neutron flux at outside surface of vessel is 5.0×10^{10} n-cm/cm^3-sec.

TABLE XXV. Region Configuration for Aluminum-window Calculations with Various Detector-zone Compositions (See Fig. 28)

Region Number	Composition of Region	Thickness of Region (cm)	Region Number	Composition of Region	Thickness of Region (cm)
6a	96% Al 4% H_{20}	20.3	8c: [52]	50% void 25% Al 25% H_2O	15.2
6b	96% Fe 4% H_2O	5.1			
6c	96% Al 4% H_2O	41.9	[53]	50% void 40% Be 10% H_2O	
7	Pressure Vessel	11.4	[54]	50% void 40% Al 10% H_2O	
8a	H_2O	0.64			
8b	Pb	6.35	[55]	90% void 10% H_2O	
8c: [48]	H_2O		8d	H_2O	45.7

TABLE XXVI. Comparisons of High-energy Neutron Fluxes at the Inside Surface of the AARR Pressure Vessel (8-ft-ID Vessel; 100 MWt)

Neutron Flux Group		Neutron Flux (n-cm/cm^3-sec)			
No.	Energy Range (MeV)	Window No. 1[a]	Window No. 2[b] (Earlier Reference)	New Reference Window[c] (No. 3)	No Window[d] (All Water)
1	6.065-10	2.0×10^7	1.2×10^7	2.5×10^6	5.0×10^6
2	3.679-6.065	1.2×10^7	6.9×10^6	1.3×10^6	3.5×10^6
3	2.231-3.679	2.1×10^7	1.2×10^7	2.4×10^6	2.9×10^6
4	1.353-2.231	5.0×10^7	3.0×10^7	8.7×10^6	2.6×10^6
5	0.821-1.353	8.7×10^7	5.8×10^7	2.3×10^7	2.5×10^6
6	0.388-0.821	3.5×10^8	2.7×10^8	1.9×10^8	4.0×10^6
7	0.183-0.388	4.1×10^8	3.3×10^8	2.5×10^8	2.7×10^6
8	0.0673-0.183	5.4×10^8	4.6×10^8	3.3×10^8	2.5×10^6

Note: These summaries of neutron flux at the inside surface of the pressure vessel are not entirely consistent. They are based upon calculations performed over a total period of roughly 9 months, during which time the reference thickness of the pressure vessel was changed and the compositions of the regions outside the pressure vessel were altered. However, these variations are higher-order effects, and the results are sufficiently close to consistency to provide valid and useful comparisons.

[a]Window No. 1 consists of a zone of aluminum with 4 v/o H_2O, filling the space between the beryllium reflector and the pressure vessel. For this case, it has been calculated that 10 yr at 100 MWt would irradiate the inside surface of the pressure vessel to 1.8×10^{17} RDU, based on the methods of Rossin.*

[b]Window No. 2 consists of: 8 in. aluminum with 4 v/o H_2O; then 2 in. SS with 4% H_2O; then 16-1/2 in. aluminum with 4% H_2O.

[c]Window No. 3 consists of: 8 in. of aluminum shroud (4% water); 8 in. of SS (4% water); 10-1/2 in. of aluminum (4% water).

[d]Actually, there will be a thin steel thermal shield inside the pressure vessel, and this will degrade the neutrons further. The neutron fluxes listed here do not include the effects of this shield.

*Rossin, A. D., ANL-6826 (March 1964).

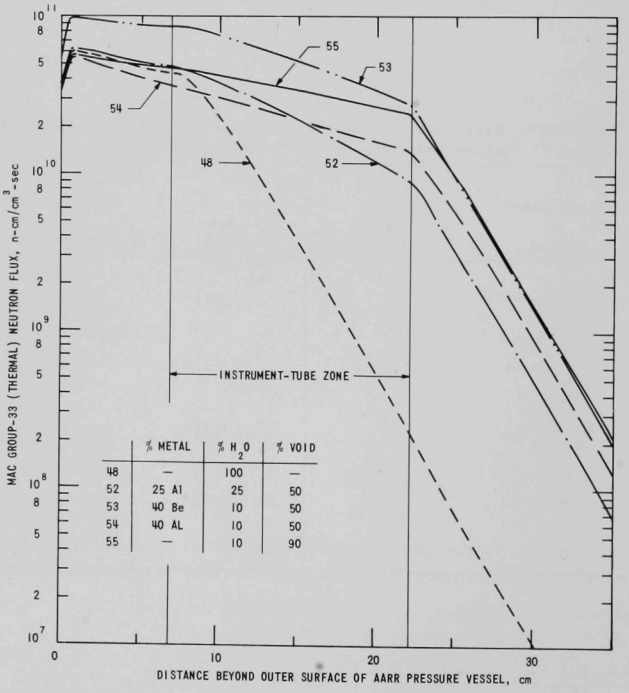

Fig. 27. Radial Distribution of Thermal-neutron Flux outside AARR Pressure Vessel as Function of Material Composition of Instrument-tube Zone (Earlier Neutron Window; 100 MWt)

IV. NUCLEAR SAFETY

A. Research and Development

1. Coolant Dynamics

a. Coolant (Water) Expulsion Studies. Work is continuing on the reduction of the height versus time data obtained from high-speed motion pictures of the expulsion process.

Possible analytical models of expulsion are being explored in terms of the water data and the anticipated behavior of sodium. It appears that a model for the highly subcooled situation is exceedingly complex; thus, initial emphasis will be on initially saturated liquid.

b. Superheat Experiments. Assembly of the initial superheat experiment is complete. The system instrumentation is still being checked out. The dump tank has been filled with sodium and the final check-out of the system is forthcoming.

c. Sodium Expulsion Experiment. Fabrication of some of the components to be used in this experiment are complete, and the building of some of the instrumentation is underway.

d. Critical Flow Studies. The construction of apparatus to study critical flow of different fluids is continuing. The boiler and blow-down vessel for the sodium loop have been installed, and the two test sections are being fabricated. The instrumentation to be used for measuring pressure and flow rate is undergoing shakedown tests.

Analytical efforts are being carried out simultaneously with the experimental program to achieve a better understanding of the critical phenomenon and to obtain better methods for evaluating critical flow rates.

The efforts associated with the high-quality region (droplet-dispersed flow) have led to an analytical solution for predicting the critical flow rate, which shows excellent agreement with existing data. The solution is briefly illustrated below.

If one-dimensional droplet flow is assumed, the equations of continuity and momentum written for a differential element at the point of choking are

$$\frac{\partial}{\partial y}[\rho_g \alpha u_g + \rho_\ell (1 - \alpha)\, u_\ell] = 0; \tag{1}$$

$$\frac{\partial}{\partial y}[\rho_g \alpha u_g^2 + \rho_\ell (1 - \alpha)\, u_\ell^2] + \frac{\partial P}{\partial y} = 0, \tag{2}$$

where

α = void fraction;

ρ_g, ρ_ℓ = density of vapor and liquid;

P = pressure;

u_g, u_ℓ = average velocity of the vapor and liquid;

y = length of differential element.

A consideration of relaxation phenomena that results from temperature and velocity lags between the phases in the approach region to critical flow leads to the following conditions:

$$\frac{\partial \alpha}{\partial P} = 0; \quad \frac{\partial x}{\partial P} = 0; \quad \frac{\partial \rho_g}{\partial P} = \frac{\rho_g}{KP},$$

where

x = quality;

K = isentropic coefficient for vapor (K = 1.32 for water vapor).

Solution of Eqs. (1) and (2), satisfying the above conditions, leads to the following solution for the critical flow rate:

$$G^2 = Kg_c P \alpha \rho_g / x^2. \tag{3}$$

It is important to note that for low pressures and high qualities, $\alpha \approx 1.0$. In this case, no information is required about the slip between the liquid and vapor phase in order to calculate the critical flow rate from Eq. (3).

Calculated values from Eq. (3) are displayed in Fig. 28 and show excellent agreement with existing data in the high quality region[24] (dispersed flow). (G_{HEM} is the flow rate predicted from the well-known homogeneous thermal equilibrium model.) Also shown in Fig. 28 is the range of predicted values from previous models published in the literature.[24-29]

---

[24]Zaloudek, F. R., HW-68934 (1961).

[25]Fauske, H. K., Proc. of Heat Transfer and Fluid Mech. Inst., Stanford University Press, 1961.

[26]Levy, S., Journal of Heat Transfer, Trans. ASME, Series C, 87, 53, 1965.

[27]Moody, F. J., Journal of Heat Transfer, Trans. ASME, Series C, 87, 134, 1965.

[28]Cruver, J. E., and Moulton, R. W., Preprint 29e, AIChE 55th National Meeting, Houston, Texas, 1965.

[29]Klingebiel, W. J., Ph.D. Thesis, University of Washington, 1964.

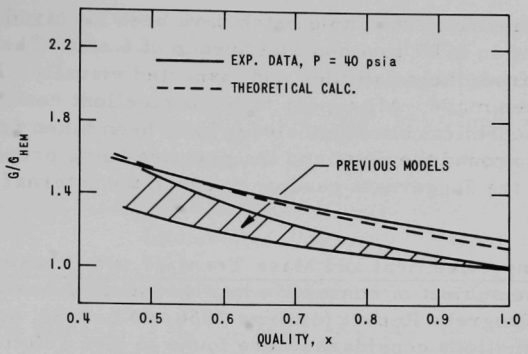

Fig. 28. Comparison between Calculated and Experimental Critical Flow Rates for Steam-Water Mixtures

In Table XXVII, calculated values from Eq. (3) are compared with the most recent data available in the literature.[29] As illustrated, the deviation between experimental and calculated values is less than ±6%. A detailed description of this analysis is under preparation.

TABLE XXVII. Comparison between Experimental and Calculated Critical Flow Rates

Experimental Data[29]			Calculated	Deviation
P_{cr}	x	G	G	(%)
52.67	0.6222	307.68	320.0	+3.9
32.11	0.5255	227.68	234.0	+2.6
41.93	0.5193	296.51	307.0	+3.4
52.43	0.5103	369.31	386.0	+4.6
33.62	0.9690	143.16	135.0	-5.6
30.73	0.6160	196.25	192.0	-2.0
50.82	0.7128	281.77	271.0	-3.9
30.17	0.7170	170.82	163.0	-4.0
49.68	0.8089	249.68	235.0	-5.8
29.95	0.8145	151.67	143.0	-5.9
48.0	0.9625	198.76	190.0	-4.5
30.9	0.723	167.03	165.0	-1.2

2. Fuel Meltdown Studies in TREAT

a. Irradiated Oxide, Fast Reactor-type, Fuel Pins. Half-length, EBR-II Mark-I size, stainless steel-clad, gas-bonded fuel pins irradiated to nominal values of 0.7 a/o and 3 a/o burnup have been studied in TREAT experiments (see Progress Report for July 1966, ANL-7245, pp. 60-61).

Six additional pins from the same batch have been received after steady-state irradiation in MTR to a nominal burnup of 6 a/o. These pins have been removed from their capsules and inspected visually. Dimension checks have been made. All appear to be in excellent condition. Specimens for radiochemical burnup analyses have been taken from the monitor wires wrapped around the pins, and the pins are being prepared for neutron radiography at the Juggernaut reactor to check the internal condition of the fuel.

b. Convective Heat and Mass Transfer with Phase Changes. Study continues on the subject of convective heat and mass transfer with change of phase (see Progress Report for June 1966, ANL-7230, p. 64). The similarity transformations considered were found to give solutions inapplicable for problems within channels, but may be of some use to describe the entrance region for "starting" the problem.

Two effects are found to be important: the Stephan-Nusselt effect or the effect of mass transfer on mass transfer via a velocity component normal to the channel wall, and an effect from the change in density, due to the phase change, which affects the rate of motion of the phase boundary. One or both of these effects have been neglected in previous related studies.

The problem has been reformulated using an integral approach often referred to as the von Karman-Poulhausen integral method. This technique leads to a set of six coupled nonlinear first-order ordinary differential equations. These equations are being checked to see if they reduce properly to cases without mass transfer or without phase change to assure that they have been correctly derived. Some approximate analytical solutions are being sought to guide the eventual computer studies.

Since the integral approach results in an approximate solution, consideration is being given to error estimates, and a comparison of results may be made to a direct numerical solution of the basic nondimensional equations.

c. TREAT Loop Experiment Run Short of Gross Sample Failure. A single EBR-II-type pin was run within a cluster of six dummy pins inside a Mark-I integral sodium loop, short of the threshold of gross failure in TREAT Test No. Tr-985. This test was run prior to the high-specific-energy pin experiment Tr-1007. In Table XXVIII exposure conditions of Tr-985 can be compared with those of Tr-1007. Both pins were run with power shaped axially to approximate a "chopped cosine" shape.

There was no external evidence of pin damage except for the usual spiral warpage. The cladding surface was smooth and micrometer readings did not reveal any diameter growth.

TABLE XXVIII. Tr-985 and Tr-1007 Conditions

Tr No.	Initial Reactor Period (sec)	Maximum Fuel Power Density (at axial midplane) (kW/cc)	Power Density in Fuel Integrated to Time of Max Reactor Power (at axial midplane) (kW-sec/cc)	Initial Sodium Flow Rate (cm/sec)
985	0.09	36.1	7.4	370
1007	0.075	76.0	13.2	400

Upon removal of the cladding, however, it could be seen that the fuel pin, which initially was 360 cm in length, was severely damaged and that considerable amounts of eutectic alloy had been formed between the fuel and inner cladding surface. The region of worst damage extended from the approximate center up to the top end of the fuel pin, and contained areas of spalling and heavy eutectic formation. There was also a severely melted area starting from about 20 cm from the bottom of this pin and extending up to the upper, or restrainer, end. The top cm of the fuel pin was separated from the rest and was hollowed out. Its upper end showed the imprint of the restrainer bottom. No fuel was found above the restrainer knob.

Some of the more interesting areas are shown in the illustrations, their relative positions (in inches) being indicated by the ruler in the photographs.

No appreciable attack of the cladding by eutectic formation was noted in this visual inspection, indicating penetration of the steel jacket by at most a few thousandths of a cm.

Calculations were made for this experiment by the methods described for Tr-1007 (see Progress Report for July 1966, ANL-7245, pp. 61-64). Although the calculated maximum fuel-cladding interface temperature was greater by about 150°C than the empirical failure threshold of ~1000°C determined for failure by cladding penetration in stagnant sodium meltdown experiment on these pins,[30] calculated internal pressures were not sufficient to cause failure. By means of the calculated curve of interface temperature versus time and penetration-rate data,[31] an upper-limit estimate was made that maximum cladding penetration was somewhat less than 0.008 cm, which shows eutectic formation to be insufficient to cause penetration of the 0.022-cm-thick cladding. Calculated maximum cladding thermal stress exceeded the maximum tensile strength of the cladding, but not by the excessive amount calculated for Tr-1007.

[30]Dickerman, C. E., et al., Nucl. Sci. and Eng. 18, 319 (1964).
[31]Walter, C., and Kelman, L., J. Nucl. Mat. 6, 281 (1962).

Thus this analysis predicts more severe results than observed, in that no cladding deformation was observed. The principal discrepancy is that the empirical failure threshold established for pins run in a stagnant sodium environment is not in agreement with the above results, suggesting that the continued forced cooling of the cladding by flowing coolant terminates penetration early, in the manner indicated by the calculations.

d. Analysis of Motions Occurring during a Loop Meltdown Experiment by Means of the Fast-neutron Hodoscope. The fast-neutron hodoscope, designed to provide a means of observing fuel motion inside TREAT test loops during a meltdown experiment, was operated for the high-specific-energy meltdown experiment performed with an EBR-II-type sodium-bonded, steel-clad pin surrounded by a ring of six dummy pins inside the Mark-I integral sodium loop. Postexperiment calculations performed on this experiment (TREAT Tr-1007) were reported last month (see ANL-7245, pp. 61-64). This experiment marked the first time that the hodoscope had been used to follow results of a loop meltdown experiment producing significant motions. The hodoscope results appear to correlate well with other data and to provide additional information on the course of the experiment.

Timing on the visicorder chart used to obtain a transient record of coolant temperature, pressure, test-section inlet flow, and reactor power, was checked against the NIXIE time clock used to record time on the film recording of hodoscope output. Times of peak reactor power agreed within 0.002 sec, which is within the uncertainty in reading the visicorder traces.

Figure 29 depicts the relative count rates from the different hodoscope positions for selected times during the experiment. At the left of the figure is a grid showing solid block rectangles at the hodoscope locations equipped with detectors. Subsequent sections of the figure show hodoscope data corrected for channel efficiency and normalized for changes in reactor power level so that arrays from different times can be compared visually, directly. By the time of frame 3.996 (i.e., the frame corresponding to 3.996 sec), however, the reactor power had become so low that no fuel pattern is discernable above the "background" of displaced fuel and surrounding materials.

The first indication of movement is seen in the frame at time 3.641 sec, where lowering of count rates suggests fuel displacement in the uppermost section of the fuel. The first indication of failure occurs in frame 3.682 (occurring 0.041 sec later), which shows a relative decrease in count rates adjacent to but not including the fuel. This could be caused by void formation in the sodium, which would decrease the "background" produced by neutrons scattered by the sodium. In conjunction with this, possible fuel movement from the main body of fuel is apparent. The vertical position of the possible sodium voiding is in the region 17 to 25 cm from the top, whereas fuel displacement is in three distinct areas: 14 to 15 cm from the top, 21.5 to 24 cm from the top, and at the bottom of the

fuel section. At 3.678 sec a severe drop in flowmeter output corresponding to change in inlet velocity from 370 cm/sec to -110 cm/sec occurred within about 0.005 sec. This abrupt flow blockage and partical expulsion of sodium is thus in good agreement with the hodoscope observation. In addition, a sharp pressure spike was recorded on the pressure transducer at the inlet to the test section at 3.68 sec.

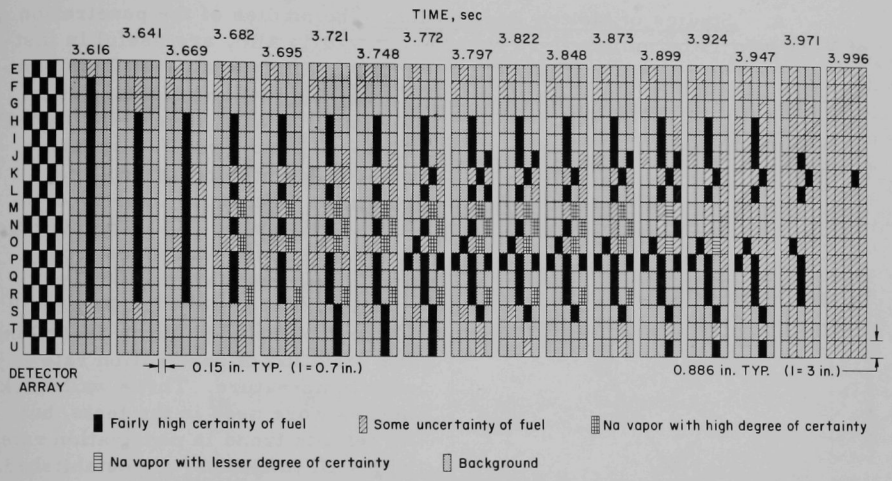

Fig. 29. A Hodoscope Record Taken of an EBR-II-type Sodium-bonded Steel-clad Fuel Pin Undergoing a High-specific-energy Meltdown Experiment (TREAT Tr-1007). The figures, taken about 25 ms apart, show the relative count rates obtained from the different detector positions. At the left of the figures is a grid of solid block rectangles showing the locations of the detectors in the hodoscope.

The next display of voiding in the fuel pin occurs at time 3.870. This is followed by additional fuel movement, notably in an upward direction as recorded in frame 3.899. The termination of sodium voiding as in frames 3.899 and 3.924, together with the spreading out of fuel, tend to imply a massive disintegration of the central part of the fuel pin, with the fuel debris concentrated around the central portion in an almost ellipsoidal distribution (see frame 3.971). After the initial flowmeter drop, erratic recovery occurred, terminating at 3.865 sec when, with flow of about 340 cm/sec the flow decreased again, reaching ~200 cm/sec at 3.910 sec. At 3.910 sec a severe flow reversal took place, with an instantaneous flow ~-1600 cm/sec occurring within a few milliseconds. (This flow anomaly was also accompanied by a simultaneous pressure spike on the pressure transducer at the test section inlet.) Together, these data indicate a collapse of sodium liquid on fuel that had been insulated from coolant, and massive disintegration of the fuel, accompanied by sharp sodium expulsion from the region of failure.

After this point, only one major feature is clearly indicated by the hodoscope record: retention of some fuel in the area of the lower part of the test pin. In spite of the violence of the dispersal, low-density fuel was found in the bottom 6-cm portion of what had been the fuel cladding.

3. Safety Related Properties of Materials

a. Studies of Molten Penetration. The studies of the penetration of V-20 w/o Ti by molten U-15 w/o Pu-6.5 w/o Ti alloy are useful in fast-reactor safety analyses. This combination of fuel and cladding is an alternate to the system of U-15 w/o Pu-10 w/o Zr and Type 304 stainless steel previously reported (see Progress Report for June 1966, ANL-7230, pp. 59-60). The average penetration rate increases from about 0.02 mm/sec at 1300°C to 0.45 mm/sec at 1450°C. Figure 30 shows the probable curve describing the variation of penetration rate with temperature. Three wall thicknesses were used in the tests, but no definite trend in penetration rate with wall thickness was established.

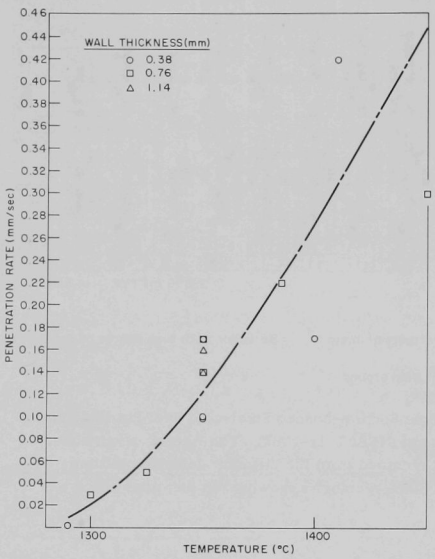

Fig. 30. Penetration Rate of V-20 w/o Ti Tubes by U-15 w/o Pu-6.5 w/o Ti Alloy

The cross section of a failed specimen was studied by electron microprobe analysis. Some of the molten metal adhered to the solid specimen, as shown in Fig. 31. Table XXIX lists the compositions of eight areas identified by numerals one through eight in Fig. 31, which is a sketch of the electron current image of the cross section. Area 1 is unaffected cladding; area 2 is cladding penetrated in the solid state for a distance of about 40 μ; area 3 is liquid fuel containing some dissolved cladding; area 4 is a nucleus of a V-20 w/o Ti grain penetrated by uranium and plutonium; area 5 is a liquid fuel similar to area 3; areas 6 and 7 are essentially nuclei of the cladding interspersed with the molten fuel area 8, but with all regions showing interdiffusion.

At 1350°C the range of solid diffusion penetration (area 2) is about an order of magnitude less in the (V-20 w/o Ti)/(U-15 w/o Pu-6.5 w/o Ti) than in (Type 304 stainless steel)/(U-15 w/o Pu-10 w/o Zr).

However, the overall rate of penetration increases much more rapidly above 1350°C in the (V-20 w/o Ti)/(U-15 w/o Pu-6.5 w/o Ti) system.

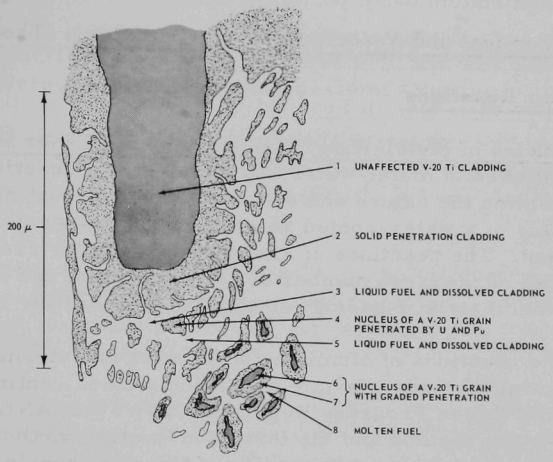

Fig. 31. Schematic of the V-20 w/o Ti Specimen Penetrated by U-15 w/o Pu-6.5 w/o Ti Alloy at 1350°C

TABLE XXIX. Compositions of Phases (w/o) Determined by Microprobe Intensity Ratios in a Couple: V-20 w/o Ti against Molten U-15 w/o Pu-6.5 w/o Ti Alloy

Electron Current Image	Very Dark	Dark	Light	Dark	Light	Dark	Grey	Light
Element								
Ti	21.6	22.0	11.5	22.4	3.9	20.5	16.3	5.3
V	79.3	46.1	6.2	39.0	3.5	39.0	21.9	3.2
U	0	21.5	69.9	28.0	73.3	25.2	54.3	74.0
Pu	0	1.7	8.8	2.2	19.1	2.9	5.5	14.5
Total Percentages	100.9	91.3	96.4	91.6	98.8	87.6	98.0	97.0

B. TREAT Operations

Two metal-water reaction, photographic series (CEN 221T and 222T) experiments were run. One stainless steel-clad and one Zircaloy-clad, UO_2 fuel pin in ambient temperature water were utilized. The film of the stainless steel-pin reaction has been processed; high-quality photographs were obtained.

The last of the SEFOR experiments, 4.1E, was finished. This experiment was designed to evaluate thermocouple designs and fuel-pellet designs. The capsule has been returned to GE-San Jose for examination.

C. Chemical and Associated Energy Problems (Thermal)

1. Metal-Water Reactions

a. Studies of Metal-Water Reactions by the Laser Heating Method. Fundamental studies of metal-water and metal-steam reactions are required to determine the nature and extent of reactions that might occur between the metals of a water-cooled reactor and the water in the event of a reactor accident. The reactions of aluminum with water are of particular interest because of the large number of reactors which use aluminum-base alloys as the fuel matrix, cladding, or structural material.

The reactions of aluminum with water and steam have been studied by several methods. In-pile excursion studies continue to be carried out in TREAT (see Progress Report for May 1966, ANL-7219, p. 83). The pressure-pulse method and the levitation-heating method have also been employed in isothermal rate studies of the aluminum-water reaction (see Progress Report for May 1964, ANL-6904, pp. 102-103). Another isothermal method utilized a high-pressure furnace[32] which allowed the aluminum-steam reaction to be studied over a wide range of steam pressures (1 to 8 atm).[33] A unique nonisothermal method was one in which aluminum particles submerged in water were rapidly heated by a laser beam. This method allowed the simulation of the condition that would exist if metal particles at high temperatures were suddenly introduced into water, as they might be in the case of a nuclear excursion.

The experimental work with the laser-beam method has been described in detail in previous reports[34-36] (see also Reactor Development Program Progress Reports for July, August, and October 1964, ANL-6923, p. 86; ANL-6936, p. 77; and ANL-6965, p. 91). A summary of the main findings of the experimental work with aluminum particles is presented herein, together with a recently devised model that satisfactorily describes the reaction process.

Most of the work was carried out with 0.1- by 0.1- by 0.002-cm pieces of aluminum foil. When melted, the foil pieces formed spheres of

[32] Chemical Engineering Division Semiannual Report, January-June 1964, ANL-6900, p. 242.
[33] Chemical Engineering Division Semiannual Report, January-June 1965, ANL-7055, p. 177.
[34] Chemical Engineering Division Semiannual Report, July-December 1963, ANL-6800, p. 327.
[35] Chemical Engineering Division Semiannual Report, July-December 1964, ANL-6925, p. 198.
[36] Chemical Engineering Division Semiannual Report, January-June 1965, ANL-7055, p. 181.

aluminum approximately 0.018 cm in radius. The principal experimental findings utilizing laser-beam heating of these aluminum particles in a water environment are as follows:

(i) In pure water at room temperature (a pressure of 0.03 atm), the extent of reaction varied between 6 and 11%, and was independent of the laser output energy in the range studied--10 to 48 joules.[35]

(ii) In room-temperature water, with one atmosphere of argon overpressure, the extent of reaction fell to about 1 and 3% at laser energies of 25 and 45 joules, respectively.[36] No threshold for complete reaction was observed.

(iii) In water at 100°C (one atmosphere pressure) and 181°C (ten atmospheres pressure), no significant reaction was found until a critical laser energy was reached; at this energy and above, complete reaction was observed.[35,36] The threshold energy was the same at both pressures.

(iv) The average time for complete reaction at both 1 and 10 atm of water pressure, as judged from the luminous time on high-speed films,[35] using all the data now available, was about 0.21 sec. Cooling times for unreacted samples were very short, being a few milliseconds.

Because of the highly protective nature of oxide films on aluminum, no extensive reaction would be expected if the film surrounding the metal remained solid and intact. For aluminum particles introduced into propane-oxygen-nitrogen flames,[37] for example, an ignition temperature has been identified with the oxide melting point of 2300°K. In the present studies, it would be expected that the aluminum could not be heated by the laser beam above its boiling point. The literature[38,39] indicates that in pure water (no inert gas present) at room temperature, the boiling point of aluminum is reached at about 2150°K (the vapor pressure of aluminum being 0.03 atm at that temperature) and the oxide melting point is not attained. (This point has been discussed.[35]) Reaction in room-temperature water thus results in sporadic cracking and rehealing of a solid, protective oxide film. The erratic results (6 to 11% reaction) and the observation of fragile, feathery, fan-shaped oxide formations on residues from reaction in room temperature water support this idea.

When the water temperature is raised to 100°C, it is then possible for the oxide melting point to be reached during the period of heating by the laser pulse. This should occur at a fairly definite energy, and extensive reaction should occur in the absence of a solid, protective oxide film.

---

[37]Friedman R., and Maček, A., Combustion and Flame 6, 9 (1962).
[38]Brewer, L., and Searcy, A. W., J. Am. Chem. Soc. 73, 5308 (1951).
[39]Kubaschewski, O., and Evans, E. Ll., Metallurgical Thermochemistry, 2nd Ed., Pergamon Press, London (1956), p. 322.

Once protectiveness has been lost, the rate of reaction seems to be controlled by the rate of diffusion of water through a hydrogen boundary layer surrounding the metal particle. (The water in the cell after reaction was found to be completely free of suspended oxide, thereby indicating that reaction between aluminum vapor and H_2O vapor was not important.)

To test the proposed reaction model, reaction rate and steady burning-temperature calculations were carried out similar to those by Baker and Just[40] for the reaction of zirconium and water. The calculations were performed by equating the rate of heat generation with the rate of heat loss and solving the resulting equation.

The rate of heat loss is the sum of losses by convection and radiation, and may be written as

$$\text{Heat loss rate} = h(4\pi r^2)(T_s - T_w) + \sigma\epsilon(4\pi r^2)(T_s^4 - T_w^4),$$

where

h = heat transfer coefficient;

r = particle radius;

T_s = particle surface temperature;

T_w = water temperature;

σ = Stefan-Boltzman constant;

ϵ = emissivity.

The heat transfer coefficient may be written in terms of the Nusselt number for heat transfer,

$$Nu = h\frac{2r}{k_f},$$

where k_f is the film thermal conductivity. The Nusselt number for spheres in free convection is given[41] by

$$Nu = 2 + 0.6\left(\frac{(2r)^3\rho^2 g\Delta T}{\mu^2 T}\right)_f^{1/4}\left(\frac{C_p\mu}{k}\right)_f^{1/3},$$

---

[40] Baker, Jr., L., and Just, L. C., Studies of Metal-Water Reactions at High Temperatures. III. Experimental and Theoretical Studies of the Zirconium-Water Reaction, ANL-6548 (May 1962).

[41] Bird, R. B., Stewart, W. E., and Lightfoot, E. N., Transport Phenomena, John Wiley and Sons (1960).

where

ρ = density;

g = gravitational constant;

$\Delta T = T_s - T_w$;

μ = viscosity;

C_p = heat capacity;

and the subscript f indicates that the physical properties are to be evaluated for the H_2-H_2O film surrounding the particle.

The rate of heat generation is simply the product of the rate of diffusion of water through the gas film surrounding the particle and the heat of reaction. This may be written as

$$\text{Heat generation rate} = h_d(4\pi r^2)\frac{\Delta P}{RT_f}Q(T_s),$$

where

h_d = mass transfer coefficient;

ΔP = water pressure difference across film;

$T_f = \frac{1}{2}(T_s - T_w)$, the mean film temperature;

$Q(T_s)$ = heat of reaction at T_s.

The coefficient h_d may be related to the Nusselt number by

$$Nu_d = h_d\frac{2r}{D},$$

where D is the diffusion coefficient and Nu_d is the Nusselt number for mass transfer.

The Nusselt numbers for heat transfer and mass transfer are identical if the diffusion coefficient D and the thermal diffusivity ($\alpha = k/\rho C_p$) are equal. By means of expressions for the physical properties of films given below, the Lewis number (α/D) is found to be about 1.04, which is sufficiently close to one to allow a single expression for Nu to be used for the evaluation of both h and h_d.

Values for μ, C_p, and k were taken from data tabulated by Svehla,[42] and averaged for equimolar mixtures of hydrogen and water by

[42]Svehla, R. A., Estimated Viscosities and Thermal Conductivities of Gases at High Temperatures, NASA-TR-132 (1961).

the procedure described by Bird, Stewart, and Lightfoot.[41] An empirical equation was found which adequately described these properties in the range of T_f from 1000 to 3000°K. The actual expressions used in the calculations are listed below:

$$k_f = 1.575 \times 10^{-4} + 7.425 \times 10^{-7} T_f;$$

$$\mu_f = 1.160 \times 10^{-4} + 2.670 \times 10^{-7} T_f;$$

$$C_p = 2.351 T_f^{0.2362}.$$

The diffusion coefficient may be expressed by

$$D = 2.493 \times 10^{-5} T_f^{1.75}/P,$$

where P is the total pressure. This expression for D was obtained by using the procedure described by Fuller, Schettler, and Giddings.[43]

From the expressions for heat generation and for D, it is seen that the rate of heat generation is proportional to $\Delta P/P$. In pure water this ratio is always 1.0 since we assume that all the water reaching the particle reacts. In the case that one atmosphere of argon overpressure was employed, however, this ratio is less than one and the reaction rate will fall. The significance of this effect will be discussed in detail later.

In choosing an expression for $Q(T_s)$, it was recognized that the reaction is not adequately described by the equation

$$2Al + 3H_2O \rightarrow Al_2O_3 + 3H_2.$$

The heat generated by this reaction would lead to impossibly high values for the burning temperature. As the temperature of reaction increases, the formation of such species as H, OH, and AlO causes a decrease in the amount of heat liberated. These species must be taken into account in calculating $Q(T_s)$. A computer program using a free-energy minimization routine, which has been used to calculate equilibrium adiabatic temperatures and pressures in sodium-air reactions (see Progress Report for June 1966, ANL-7230, p. 70), was used to calculate compositions and heats of reaction for the Al-H_2O system. The formation of hydrogen atoms was clearly the most important factor in decreasing the amount of heat generated by reaction at increasing temperature. An equation of the form

$$Q(T_s) = \alpha + \beta T + \gamma T^2 + \frac{\delta}{T}$$

was used to fit computed Q values.

---

[43]Fuller, E. N., Schettler, P. D., and Giddings, J. C., Ind. Eng. Chem. 58, 19 (1966).

Choosing a value for the emissivity of the burning particle was difficult, and calculations were carried out for pure water at one atmosphere for emissivities ranging from 0.1 to 1.0. The effect of emissivity on reaction rate proved to be quite small, as would be expected, whereas the effect of emissivity on temperature increased with increasing particle size. In the particle size range of the laser experiments, the effect on temperature was not very great, however. An emissivity value of 0.3 was used in the subsequent computations.

All the pertinent equations were combined and solved utilizing a CDC-3600 digital computer. The calculated results were then compared with the experimental value for average reaction rate for the 0.018-cm-radius particle. The earlier observation of a 0.21-sec reaction time yields an average reaction rate of 1.8×10^{-5} moles H_2O/sec. The calculated average rates at 1 and 10 atm for r = 0.018 cm are, respectively, 1.4×10^{-5} and 1.6×10^{-5} moles H_2O/sec. This is in satisfactory agreement with the experimental value.

One additional experimental observation remains to be explained, namely, the observation that, in room-temperature water with one atmosphere of argon overpressure, a reaction threshold is not reached and the extent of reaction is small. The explanation for this lies in the dependence of the reaction rate on $\Delta P/P$. In pure water this ratio is always exactly one. With an inert gas present, it is less than one, and the rate of reaction is reduced. In this case, even though the aluminum particle can be heated above the melting point of Al_2O_3 (2300°K), the steady-state temperature cannot be maintained above 2300°K, owing to a reduced reaction rate, and the particle is simply quenched. For this case, however, the value of $\Delta P/P$ for water at 25°C, namely, 0.03, cannot be used. It has been pointed out[40] that in both the zirconium-water and uranium-water reactions, a value of 0.5 should be used for 25°C water because of the dynamic equilibrium existing at the water-water vapor interface. For the case being discussed here a value for $\Delta P/P$ of about 0.15 or below will suffice to lower the steady-state temperature to a value below 2300°K. The difference between the value of 0.15 and that suggested by Baker of 0.5 probably results from the much higher temperature involved here.

The proposed model thus seems to account reasonably well for the main features of the reactions observed. It should be emphasized, however, that this model is adequate only for small particles. With massive aluminum samples, additional processes, such as flow of molten metal and widespread rupture of the protective oxide, would be expected to give extensive reaction at temperatures considerably below the 2300°K required for extensive reaction with the small particles that were employed in this work.

[40]Ibid., p. 84.

D. Plutonium Volatility Safety

The environmental contamination control for volatility processing involves treatment of gas streams containing plutonium hexafluoride and fission product fluorides (such as tellurium fluorides) as well as treatment of gas streams containing reagents such as fluorine gas. Experimental programs are under way to provide information required for the safe containment of PuF_6 within ventilated enclosures and to investigate the chemistry of tellurium fluorides and means for the disposal of gaseous reagents.

1. Cleanup of Cell Exhaust Air Contaminated with Plutonium Hexafluoride

Owing to the high volatility of plutonium hexafluoride (b.p. 62°C) and extreme toxicity of plutonium, it is necessary that highly efficient methods be used to prevent the release of plutonium to the environment. When PuF_6 is released into the atmosphere it reacts with moisture in the air to produce solid PuO_2F_2, which can be removed from ventilation air by filtration with high-efficiency filters. Under conditions of low moisture concentrations, the reaction occurs predominantly on exposed surfaces, while at high moisture concentrations the reaction occurs in the gas phase to produce a fume of PuO_2F_2. A series of experiments is being made to determine how each type of reaction affects filter penetration and to measure plutonium particulate penetration through a series of filters. The apparatus used in these experiments is shown in Fig. 32. A disc of filter media is mounted between two glass funnels to form a filter unit. Each unit is tested for DOP (dioctylphthalate) penetration prior to use. Four units are assembled in a series before the entire assembly is placed in the glovebox. Four filters are required to measure accurately low-level plutonium penetration of the second filter. The function of the third filter is to contain material penetrating the second filter; the fourth filter serves to preclude back-contamination of the third filter. A stream of PuF_6 in dry air is mixed with a moist air stream in a Plexiglas chamber. Analyses of the filters are difficult owing to the small quantity (10^{-9} mg Pu) of plutonium on the filters.

Twelve experiments have been completed and analytical work is now in progress. Results will be reported as they become available.

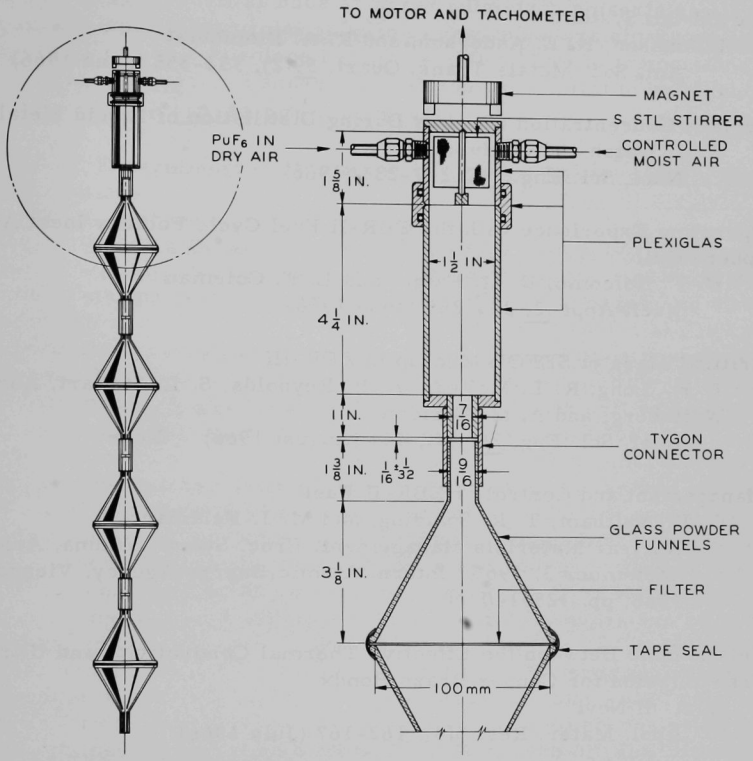

Fig. 32. Apparatus for Filtration of Plutonium Particulate Material

V. PUBLICATIONS

Papers

Partial Constitutional Diagrams for the Cd-La, Cd-Ce, Cd-Pr, Cd-Nd, and Cd-Sm Systems
I. Johnson, K. E. Anderson, and R. A. Blomquist
Am. Soc. Metals Trans. Quart. 59(2), 352-355 (June 1966) Note

Surface Concentration Changes During Distillation of Liquid Metals
W. J. Walsh and G. Burnet
Nucl. Sci. Eng., 25, 227-235 (1966)

Operating Experience with the EBR-II Fuel Cycle Facility Inert Atmosphere Cell
W. F. Holcomb, D. M. Paige, and L. F. Coleman
Nucl. Appl. 2, 254-255 (June 1966)

Critical Mass of SEFOR Mockup in ZPR-III
J. K. Long, R. L. McVean, A. B. Reynolds, S. L. Stewart, Abraham Weitzberg, and A. M. Leridon
Nucl. Sci. Eng. 25, 442-444 (August 1966) Note

Management and Control of EBR-II Fuel
G. K. Whitham, T. R. Spalding, and M. J. Feldman
Nuclear Materials Management, Proc. Symp., Vienna, August 30-September 3, 1965. Intern. Atomic Energy Agency, Vienna, 1966, pp. 123-140

Relationship Between the Effective Thermal Conductivity and Ultrasonic Transmission for Copper Braze Bonds
R. A. di Novi
Appl. Mater. Res. 5(3), 162-167 (July 1966)

Characteristics of a Thermal Neutron Television Imaging System
Harold Berger
Mater. Eval. 24, 475-481 (September 1966)

LiF Thermoluminescence for Neutron Image Storage
Jacob Kastner, Harold Berger, and I. R. Kraska
Nucl. Appl. 2, 252-253 (June 1966)

Isothermal Drop Calorimeter for Alpha Active, Pyrophoric Materials
Howard Savage
Rev. Sci. Instr. 37, 1062-1064 (August 1966)

Synthesis of an Optimal Nuclear Reactor Control System
I. E. Kliger
Neutron Dynamics and Control, Proc. Symp. on Nuclear Engineering, The University of Arizona, Tucson, April 5-7, 1965. USAEC Report CONF-650413 (1966), pp. 110-136

Temperature-Enthalpy Diagram Helps Analyze Nuclear Reactor Steam Systems
Donald Lutz
Power 110, 76-77 (August 1966)

TREAT Experiments to Provide Data for Fast Reactor Safety Kinetics Calculations
C. E. Dickerman and L. E. Robinson
Neutron Dynamics and Control, Proc. Symp. on Nuclear Engineering, The University of Arizona, Tucson, April 5-7, 1965. USAEC Report CONF-650413 (1966), pp. 371-385

Analytic Error Estimates for Integral-Equation Eigenvalue Problems in Neutron Physics
D. A. Sargis and L. M. Grossman
Nucl. Sci. Eng. 25, 395-406 (August 1966)

Nuclear Power and Oceanic-System Energy: Concepts and Applications
B. I. Spinrad and E. J. Croke
Proc. AIAA-ONR Symp. on Deep Submergence Propulsion and Marine Systems, U. S. Naval Ordnance Plant, Forest Park, Ill., February 28-March 1, 1966. Am. Inst. Aeronautics and Astronautics, Chicago, 1966, pp. 265-296

ANL Report

ANL-7228 CATALOG OF NUCLEAR REACTOR CONCEPTS. Part I. Homogeneous and Quasihomogeneous Reactors. Section VI. Solid Homogeneous (Semihomogeneous) Reactors
Charles E. Teeter, James A. Lecky, and John H. Martens

B